Studying Droplet Behavior and Capillary flow in Open Microfluidic Channels

Jing Jei Lee

A dissertation

submitted in partial fulfillment of the

requirements for the degree of

Doctor of Philosophy

University of Washington

Year (2021)

Reading Committee:

Ashleigh B. Theberge, Chair

Robert Synovec

Dan Fu

Program Authorized to Offer Degree:

Chemistry

University of Washington

Abstract

Studying Droplet Behavior and Capillary flow in Open Microfluidic Channels

Jing Jei Lee

Chair of the Supervisory Committee:
Ashleigh Theberge, Ph.D.
Department of Chemistry

This dissertation discusses advancements in open channel microfluidics, the design and fabrication of open channels and capillary pumps, and methods to manipulate open channels. An open droplet-based microfluidics platform is demonstrated with promising future applications. Additionally, an expression to measure the velocity of capillary flow in an open channel and design guidelines for an efficient capillary pump are presented.

Chapter 1 discusses the field of microfluidics and the advantages of such platforms. The fundamentals of open microfluidics is presented along with the benefits of open channel systems. Capillary flow is discussed, and the necessary considerations for fabrication of channels to ensure that the fluid in the system is driven by capillary means is provided. Droplet-based microfluidics is a large subfield of microfluidics, which is briefly reviewed, and a need for further fundamental and applied work using droplet-based systems which are completely driven

by capillary flow is discussed. Finally, capillary pumps provide a solution to the inherent decrease of velocity (and flow rate) observed in channels driven by capillary flow.

Chapter 2 introduces droplet-based microfluidics where droplets are formed in an open channel that is completely driven by capillary means. Our work represents the first time that this phenomenon was observed and studied. The interaction that exists between a droplet and the surrounding phase is described in detail.

Chapter 3 explores fundamental microfluidic features in open channels: droplet splitting, multiple droplets, and droplet merging. An example of an open platform that enables users to manipulate droplets on the same chip is presented.

Chapter 4 investigates capillary flow in an open channel, and an expression to measure velocity derived from the Lucas-Washburn-Rideal law is presented. The capillary flow in bifurcations and networks of open channels are studied.

Chapter 5 investigates the theory of open capillary pumps to alleviate the inherent decrease of velocity and flow rate during capillary flow. Design guidelines of an efficient open capillary pump are discussed.

Chapter 6 concludes the thesis with an overall perspective of the field and other experimental proposals to improve the overall design of open channels and capillary pumps and to enable applications with the platform.

TABLE OF CONTENTS

LIST OF FIGURES

LIST OF TABLES

ACKNOWLEDGEMENTS

I had a wonderful five years learning microfluidics in Seattle. I really appreciated the opportunity to attend the University of Washington and join the Theberge lab. I sincerely appreciated the support of the Theberge lab members, chemistry department staff, colleagues, and fellow TAs whom I have been teaching with throughout my Ph.D. studies. I'd also like to thank John, Tammi, Ulri, and Kathleen for all of the discussions on designs and milling, Dr. Sam Berry, for all of the help on revising manuscripts and exams writings, Dostie, for all of the feedback on the writings and figures designs, Dr. Jian-Wei Khor, for showing me how to utilize code to enhance the efficiency and accuracy of experimental measurements, and Xiaojing, for the lab trainings and other lab help.

I would like to thank my advisor Dr. Ashleigh Theberge for her guidance during these years. Her enthusiasm in microfluidics is what drives our lab to produce creativity in developing microfluidic devices. I would also like to thank Dr. Erwin Berthier for his advice on the projects. Lastly, I'd like to thank Dr. Jean Berthier on the collaboration these years on working to develop the theory and physics behind microfluidics. Without my advisors, I would not have overcome the challenges in order to continue my scientific career in the future.

I would also like to thank my past and current exam committee members Dr. Robert Synovec, Dr. Sarah Keller, Dr. Dan Fu, Dr. Joshua Vaughan, and Dr. Jonathan Posner. I appreciated the feedback and comments that you gave me throughout the exams.

To the Alemán lab, thank you for giving me a space to do my undergraduate research. Thank you Dr. Alemán for the encouragement to apply for a Ph.D. program and the opportunities to present at conferences. Thank you to the rest of chemistry professors at Stanislaus State for your

guidance and teaching during undergraduate. You truly inspired me to become a scientist just like you are.

Outside of lab, I appreciate the support from my friends in California, Curaçao, and Seattle for their understanding these years.

Last but not least, I sincerely would like to thank my husband, parents, siblings, grandparents, cousins, and the rest of my family for their help, support, and understanding these years. Thanks for always listening to my science talks outside of school. You always believe in me, and never gave up in me during my lowest time. I would have not finished this chapter without you. ‘Masha danki’, as we say Thank You in Curaçao.

DEDICATION

I would like to dedicate this dissertation to my family who always set up me up for challenges. Without your support, I would have not become the first one in our family to be honored with a doctoral degree. Thank you for always listening to my science talks.

I would also like to thank my husband for all of the support, the late-night writing reviews, waiting in the lab to finish up experiments, and encouraging me through this process.

Chapter 1. INTRODUCTION

Parts of this chapter are excerpted and paraphrased from my published work in Chapters 2 – 5.

1.1 MICROFLUIDICS SYSTEMS

Microfluidics is the study of fluid flow confined in channels or networks where at least one of the dimensions is on the micron scale[1,2]. Microfluidics has advanced the fields of biochemistry, chemistry, engineering, physics, and technology since the 1980s. Applications of microfluidics can be found in engineering, biology, diagnostics, and point of care testing[1]. Microfluidic systems allow (1) rapid analysis; (2) use of small samples, thereby lowering cost and consumption of reagents and generating less waste; and (3) increased sensitivity in separations and detections of samples at high resolution[2,3]. Microfluidics also enables applications such as multiplexing, automation, and high throughput screening experiments, all of which can be performed on a single chip.

Most microfluidic systems are closed-channel platforms, where the majority require external pumps or syringes for fluid actuation and multi-step fabrication which can lead to bubbles being trapped in the channel. Fabricating these channels may require complex designs, and the equipment can be costly. These microfluidic systems are thus not applicable in laboratory spaces that lack such equipment, and are not easy to translate to other laboratories that lack such supplies or other low-resource settings[4–7].

1.1.1 *Open microfluidics systems*

Recently, capillary-driven open microfluidic systems have gained popularity as they alleviate some of the challenges of closed microfluidic systems. Open fluidic channels (e.g., channels devoid of a ceiling, devoid of a ceiling and floor, or devoid of lateral walls) have emerged as alternatives to closed channel, pump-driven microfluidic platforms due to their relative ease of design, fabrication, and use[1,8]. In capillary-driven flow, channels can be filled using a simple pipette, a tool that is available in most laboratory settings. Open microfluidic systems offer many advantages for conducting life science experimentation including pipette accessibility and independence from pumps and external flow generators, as the mechanism for flow is built into the device[8]. Open channels do not require bonding and can be fabricated in a single step using micromilling[9–11] or high-volume fabrication techniques such as injection molding[12,13]. Open channels also offer ease of accessibility and intervention to the flowing liquid in the system at any time[1] so fluids, cells, or tissue can be added at any point along the channel by simply pipetting from the top. Finally, open microfluidic systems are reliable as air-bubbles and bonding-defects are alleviated.

1.2 DROPLET-BASED MICROFLUIDICS SYSTEMS

Droplet-based microfluidics advances the capabilities of traditional single-phase microfluidic platforms by compartmentalizing chemical and biological experiments in microfluidic channels. In such systems, immiscible fluids are introduced, allowing reagents to be confined to droplets. Users can precisely form, manipulate, and transport small volumes (picoliter to microliter droplets) for use in cell-based assays, chemical synthesis, and biochemical analyses[14].

Droplet-based platforms enable applications such as high throughput cell screening, DNA sequencing, directed evolution, and chemical reactions[15].

In addition to throughput, key advantages of droplet-based microfluidics include (1) the ability to manipulate discrete volumes of fluid within microfluidic channels without dispersion, (2) the ability to compartmentalize reagents into individual droplets with low or no chemical crosstalk, and (3) the ability to miniaturize chemical and biological processes to reduce reagent consumption and handle low volume samples.

Droplet-based systems for an extensive range of functions have been described[15], and droplet manipulation methods such as incubation[16,17] , reagent addition[18], and splitting[19,20] have been developed. However, most current droplet-based microfluids systems still rely on complex designs, a multistep fabrication method (e.g., photolithography, bonding) to create a closed system, and the use of external pumps to manipulate the flow making it more challenging to use in labs that lack such equipment.

1.2.1 *Droplet-based open microfluidics systems*

Alternatively, capillary-driven open microfluidics address many of the problems of closed microfluidic systems as discussed earlier. In an open microfluidic platform, droplets can be created by simply pipetting reagents in a channel. The behavior of droplets in a closed channel is well studied, but droplet generation in an open channel remains largely unexplored. Li et al. started to explore the creation of biphasic flows in syringe-pump driven, paper-based systems[21]. However, the physics of two-phase capillary flows as well as the behavior of immiscible droplets or plugs in an open capillary flow remained unstudied, an important gap in the literature that this dissertation fills.

The application of open capillary-driven systems for droplet microfluidics promises to enable features including simplicity of manufacturing and access to droplets in real time. However, multiple challenges such as droplet generation and droplet manipulation must be overcome to create functional droplets in open microfluidics. Open microfluidics, biphasic microfluidics, and fluid flow without external pressure offer many advantages as described earlier, and a system that can combine these aspects could be beneficial to the field of microfluidics and myriad downstream applications.

1.3 CAPILLARY-DRIVEN FLOW IN MICRO CHANNELS

The considerable development in understanding surface tension driven flows in open channels and the development of applications of open microfluidic flows has driven a gain in popularity in the field of open microfluidics. The use of passive capillary forces, also known as spontaneous capillary flow (SCF), to drive fluids eliminates the need for external pumping equipment, which is critical for applications in low resource settings[22–24] and for easy translation to laboratories[25,26]. Capillary flow is governed by the balance between capillary forces and wall friction. This analysis was first done by Lucas, Washburn, and Rideal (LWR) for cylindrical tubes in the 1920s[27–29]. Shortly after, Bosanquet[30] established the general equation of the motion of fluids in capillary channels. They all show that velocity of capillary flow decreases as the inverse of the square root of time or as the inverse of the travel distance.

While capillarity in closed, cylindrical tubes is well-known, the fundamentals of capillarity in channels of arbitrary cross sections of closed[27–30] and open channels are more recent. Rye, Yost, and Romero demonstrated that the open capillary flow of solder in V-grooves followed the predictions of the LWR law where the square root of time is dependent on the travel

distance[31–33]. Sharp V-grooves have been shown to accommodate fast capillary flows[34]. The behavior of capillary flow in rectangular open channels and in open channels of non-uniform cross-sections has been investigated[35–37]. Finally, suspended capillary flows, (i.e., open capillary flows in channels devoid of bottom and ceiling) have been documented[8,38].

The aforementioned studies have confirmed that the square root of time dependency of the travel distance is valid except at the short initial phase where inertia plays a role[39,40]. Capillary flow in bifurcations, bypasses and networks are still largely unexplored, except for the numerical work of Mehrabian et al. for closed channels[41]. Therefore, it is necessary to develop an expression to measure the velocity of capillary flow in open channels with bifurcations and bypasses.

1.3.1 *Spontaneous capillary flow (SCF)*

The conditions at which SCF occurs in different geometries have been well studied. Casavant et al[8]. developed a condition to predict SCF flow in different geometries. For capillary flow to occur in a channel, the dimensions of the channel has to satisfy the condition for open flow:

$$\frac{p_f}{p_w} < \cos\theta$$

where p_w is the wetted perimeter (i.e., the sum of the solid-liquid interfaces from a cross-sectional view); p_f is the free perimeter (i.e., the sum of the air-liquid interfaces from a cross-sectional view); and θ is the contact angle of liquid on the channel surface given that the channel

surface is homogenous. In the case of non-homogenous channel surfaces the generalized Cassie angle can be used in place of the contact angle.[1]

1.4 CAPILLARY PUMPING IN OPEN MICRO CHANNELS

To extend the applications of capillary-driven microfluidics, it is necessary to overcome a fundamental limitation of capillary flow: the inherent decrease in flow rate as the flow advances through a microfluidic channel. Capillary pumps have been designed to maintain a high enough flow rate and to extend the duration of the flow. The design of capillary pumps mimic the structure of paper or threads or the arborescence of a tree[42–44]. These materials provide a large volume available for wicking the liquids and maintain a significant flow rate in the root channel. Many different designs of capillary pumps have been experimentally developed for closed systems, but not for open systems. An efficient capillary pump can enhance open channel usability in both biological and chemical applications.

1.5 SUMMARY

This dissertation advances each of the areas described in this Introduction. Please refer to the Abstract for a complete summary; briefly: Chapter 2 introduces the concept of open channel droplet-based microfluidics for the first time and investigates the fundamentals of capillary flow in the presence of an immiscible fluid plug (droplet). Chapter 3 advances the "tool box" for open channel droplet-based microfluidics including modules for droplet splitting, manipulating multiple droplets, and droplet merging. Chapter 4 investigates capillary flow in an open channel with bifurcations and networks, and an expression to measure velocity derived from the Lucas-Washburn-Rideal law is presented. Chapter 5 presents theory and design guidelines for the use of

open capillary pumps to alleviate the inherent decrease of velocity and flow rate during capillary flow.

1.6 REFERENCES

1. Berthier, J.; Brakke, K. A.; Berthier, E. Open Microfluidics; Wiley, 2016.
2. Whitesides, G. M. The Origins and the Future of Microfluidics. Nature 2006, 442 (7101),
3. Schneider, T.; Kreutz, J.; Chiu, D. T. The Potential Impact of Droplet Microfluidics in Biology. Anal. Chem. 2013, 85 (7), 3476–3482.
4. Juncker, D.; Schmid, H.; Ute, D.; Heiko, W.; Marc, W.; Bruno, M.; Nico, de R.; Emmanuel, D. Autonomous Microfluidic Capillary System. Anal. Chem. 2002, 74, 6139–6144.
5. Yager, P.; Edwards, T.; Fu, E.; Helton, K.; Nelson, K.; Tam, M. R.; Weigl, B. H. Microfluidic Diagnostic Technologies for Global Public Health. Nature 2006, 442, 412–418.
6. Gervais, L.; Hitzbleck, M.; Delamarche, E. Capillary-Driven Multiparametric Microfluidic Chips for One-Step Immunoassays. Biosens. Bioelectron. 2011, 27 (1), 64–70.
7. Safavieh, R.; Juncker, D. Capillarics: Pre-Programmed, Self-Powered Microfluidic Circuits Built from Capillary Elements. Lab Chip 2013, 13, 4180–4189.
8. Casavant, B. P.; Berthier, E.; Theberge, A. B.; Berthier, J.; Montanez-Sauri, S. I.; Bischel, L. L.; Brakke, K.; Hedman, C. J.; Bushman, W.; Keller, N. P.; Beebe, D. J. Suspended Microfluidics. Proc. Natl. Acad. Sci. U. S. A. 2013, 110, 10111–10116.
9. Guckenberger, D. J.; de Groot, T.; Wan, A. M.-D.; Beebe, D.; Young, E. Micromilling: A Method for Ultra-Rapid Prototyping of Plastic Microfluidic Devices. Lab Chip 2015, 15 (11), 2364–2378.
10. de Groot, T. E.; Veserat, K. S.; Berthier, E.; Beebe, D. J.; Theberge, A. B. Surface-Tension Driven Open Microfluidic Platform for Hanging Droplet Culture. Lab Chip 2016, 16 (2), 334–344.
11. Barkal, L. J.; Theberge, A. B.; Guo, C.-J.; Spraker, J.; Rappert, L.; Berthier, J.; Brakke, K. A.; Wang, C. C. C.; Beebe, D. J.; Keller, N. P.; Berthier, E. Microbial Metabolomics in Open Microscale Platforms. Nat. Commun. 2016, 7, 10610.
12. Lee, U. N.; Su, X.; Guckenberger, D. J.; Dostie, A. M.; Zhang, T.; Berthier, E.; Theberge, A. B. Fundamentals of Rapid Injection Molding for Microfluidic Cell-Based Assays. Lab Chip 2018, 18 (3), 496–504.
13. Lee, Y.; Choi, J. W.; Yu, J.; Park, D.; Ha, J.; Son, K.; Lee, S.; Chung, M.; Kim, H. Y.; Jeon, N. L. Microfluidics within a Well: An Injection-Molded Plastic Array 3D Culture Platform. Lab Chip 2018, 18 (16), 2433–2440.
14. Teh, S. Y.; Lin, R.; Hung, L. H.; Lee, A. P. Droplet Microfluidics. Lab on a Chip. Royal Society of Chemistry January 29, 2008, pp 198–220.
15. Shang, L.; Cheng, Y.; Zhao, Y. Emerging Droplet Microfluidics. Chem. Rev. 2017, 117, 7964–8040.

16. Frenz, L.; Blank, K.; Brouzes, E.; Griffiths, A. D. Reliable Microfluidic On-Chip Incubation of Droplets in Delay-Lines. Lab Chip 2009, 9 (10), 1344–1348.
17. Boukellal, H.; Selimović, E.; Jia, Y.; Cristobal, G.; Fraden, S. Simple, Robust Storage of Drops and Fluids in a Microfluidic Device. Lab Chip 2009, 9 (2), 331–338.
18. Abate, A. R.; Hung, T.; Mary, P.; Agresti, J. J.; Weitz, D. A. High-Throughput Injection with Microfluidics Using Picoinjectors. Proc. Natl. Acad. Sci. U. S. A. 2010, 107, 19163–19166.
19. Link, D. R.; Anna, S. L.; Weitz, D. A.; Stone, H. A. Geometrically Mediated Breakup of Drops in Microfluidic Devices. Phys. Rev. Lett. 2004, 92 (5), 4.
20. Song, H.; Chen, D. L.; Ismagilov, R. F. Reactions in Droplets in Microfluidic Channels. Angew. Chemie Int. Ed. 2006, 45 (44), 7336–7356.
21. Li, C.; Boban, M.; Tuteja, A. Open-Channel, Water-in-Oil Emulsification in Paper-Based Microfluidic Devices. Lab Chip 2017, 17, 1436–1441.
22. Hadimioglu, B.; Stearns, R.; Ellson, R. Moving Liquids with Sound: The Physics of Acoustic Droplet Ejection for Robust Laboratory Automation in Life Sciences. J. Lab. Autom. 2016, 21 (1), 4–18.
23. Demirci, U. Acoustic Picoliter Droplets for Emerging Applications in Semiconductor Industry and Biotechnology. J. Microelectromechanical Syst. 2006, 15 (4), 957–966.
24. Choi, K.; Ng, A. H. C.; Fobel, R.; Wheeler, A. R. Digital Microfluidics. Annu. Rev. Anal. Chem. 2012, 5 (1), 413–440.
25. Gervais, L.; de Rooij, N.; Delamarche, E. Microfluidic Chips for Point-of-Care Immunodiagnostics. Adv. Mater. 2011, 23, H151–H176.
26. Nilghaz, A.; Ballerini, D. R.; Guan, L.; Li, L.; Shen, W. Red Blood Cell Transport Mechanisms in Polyester Thread-Based Blood Typing Devices. Anal. Bioanal. Chem. 2016, 408, 1365–1371.
27. Lucas, R. Ueber Das Zeitgesetz Des Kapillaren Aufstiegs von Flüssigkeiten. Kolloid-Zeitschrift 1918, 23, 15–22. https://doi.org/10.1007/BF01461107.
28. Washburn, E. W. The Dynamics of Capillary Flow. Phys. Rev. 1921, 17, 273–283.
29. Rideal, E. K. On the Flow of Liquids under Capillary Pressure. Philos. Mag. Ser. 6 1922, 44, 1152–1159.
30. Bosanquet, C. H. On the Flow of Liquids into Capillary Tubes. Philos. Mag. Ser. 6 1923, 45, 525–531.
31. Rye, R. R.; Yost, F. G.; Mann, J. A. Wetting Kinetics in Surface Capillary Grooves. Langmuir 1996, 12, 4625–4627.
32. Yost, F. G.; Rye, R. R.; Mann, J. A. Solder Wetting Kinetics in Narrow V-Grooves. Acta Mater. 1997, 45, 5337–5345.
33. Romero, L. A.; Yost, F. G. Flow in an Open Channel Capillary. J. Fluid Mech. 1996, 322, 109–129.
34. Berthier, J.; Brakke, K. A.; Furlani, E. P.; Karampelas, I. H.; Poher, V.; Gosselin, D.; Cubizolles, M.; Pouteau, P. Whole Blood Spontaneous Capillary Flow in Narrow V-Groove Microchannels. Sensors Actuators, B Chem. 2015, 206, 258–267..
35. Yang, D.; Krasowska, M.; Priest, C.; Popescu, M. N.; Ralston, J. Dynamics of Capillary-Driven Flow in Open Microchannels. J. Phys. Chem. C 2011, 115, 18761–18769.
36. Berthier, J.; Brakke, K. A.; Berthier, E. A General Condition for Spontaneous Capillary Flow in Uniform Cross-Section Microchannels. Microfluid. Nanofluidics 2014, 16, 779–785.

37. Ouali, F. F.; McHale, G.; Javed, H.; Trabi, C.; Shirtcliffe, N. J.; Newton, M. I. Wetting Considerations in Capillary Rise and Imbibition in Closed Square Tubes and Open Rectangular Cross-Section Channels. Microfluid. Nanofluidics 2013, 15 (3), 309–326.
38. Berthier, J.; Brakke, K. A.; Gosselin, D.; Bourdat, A.-G.; Nonglaton, G.; Villard, N.; Laffite, G.; Boizot, F.; Costa, G.; Delapierre, G. Suspended Microflows between Vertical Parallel Walls. Microfluid. Nanofluidics 2015, 18, 919–929.
39. Quéré, D. Inertial Capillarity. Europhys. Lett. 1997, 39, 533–538.
40. Trejo-Soto, C.; Costa-Miracle, E.; Rodriguez-Villarreal, I.; Cid, J.; Alarcón, T.; Hernández-Machado, A. Capillary Filling at the Microscale: Control of Fluid Front Using Geometry. PLoS One 2016, 11 (4), e0153559.
41. Mehrabian, H.; Gao, P.; Feng, J. J. Wicking Flow through Microchannels. Phys. Fluids 2011, 23 (12), 122108.
42. Elizalde, E.; Urteaga, R.; Berli, C. L. A. Rational Design of Capillary-Driven Flows for Paper-Based Microfluidics. Lab Chip 2015, 15 (10), 2173–2180.
43. Tsai, Y. F.; Shieh, C. J.; Yang, H. Capillary Force Pumping Fluid for Glucose Oxidase Enzymatic Fuel Cells. Microsyst. Technol. 2017, 23 (9), 3927–3935.
44. Liu, H.; Zhang, X.; Hong, Z.; Pu, Z.; Yao, Q.; Shi, J.; Yang, G.; Mi, B.; Yang, B.; Liu, X.; Jiang, H.; Hu, X. A Bioinspired Capillary-Driven Pump for Solar Vapor Generation. Nano Energy 2017, 42, 115–121.

Chapter 2. DROPLET BEHAVIOR IN OPEN BIPHASIC MICROFLUIDICS

Reproduced in part from Lee, J.J.; Berthier, J*.; Brakke, K.A.; Dostie, A.M.; Berthier, E.; Theberge, A.B. Droplet Behavior in Open Biphasic Microfluidics. Langmuir 2018, 34, 5358−5366.*

**denotes co-authorship. J.J.L contributed to the overall fabrication designs and experimental designs. J.B. developed the analytical model and numerical simulation of this work.*

2.1 ABSTRACT

Capillary open microsystems are attractive and increasingly used in biotechnology, biology, and diagnostics as they allow simple and reliable control of fluid flows. In contrast to closed microfluidic systems, however, two-phase capillary flows in open microfluidics have remained largely unexplored. In this work, we present the theoretical basis and experimental demonstration of spontaneous capillary flow of two-phase systems in open microchannels. Analytical results show that an immiscible plug placed in an open channel can never stop the spontaneous capillary flow of a fluid in a uniform cross section microchannel. Numerical investigations of the morphologies of immiscible plugs in a capillary flow reveal three different possible behaviors. Finally, the predicted behaviors of the plugs are demonstrated experimentally, revealing an effect of inertial forces on the plug behavior. A model for predicting plug behavior in spontaneous capillary flows is proposed, enabling the design of open microfluidic droplet-based systems that are simple to fabricate and use. The open channel approach to droplet-based microfluidics has the potential to enable applications in which each drop can be accessed at any time and any location with simple pipettes or other fluid dispensing systems.

2.2 INTRODUCTION

In this work, we establish the first model of the behavior of immiscible fluid plugs in capillary-driven open microfluidic flows. We demonstrate, using numerical simulations and experimental validation, that immiscible plugs display different behavior modes when placed in a flow of carrier solvent driven by spontaneous capillary flow (SCF). The behavior of the plug is controlled by interfacial tension forces at low velocities of the carrier fluid and is altered as the velocities increase. The plug behavior modes enable different approaches to manipulating aqueous plugs in open microfluidic channels, including using the solvent to move the aqueous plug along the channel or flowing the solvent over a stationary aqueous plug. Methods for manipulating immiscible plugs in open channels demonstrated here show promise for controlling confined aqueous droplets without extraneous pumping equipment, bringing together some of the benefits of droplet-based microfluidics and capillary-driven open microfluidics.

Droplet-based microfluidics is a powerful tool for compartmentalizing chemical and biological experiments in microfluidic channels. In such platforms, picoliter to microliter droplets are generated and manipulated in an immiscible phase, enabling applications such as high throughput cell screening, DNA sequencing, directed evolution, and chemical reactions.[1] In addition to throughput, key advantages of droplet-based microfluidics include (1) the ability to manipulate discrete volumes of fluid within microfluidic channels without dispersion, (2) the ability to compartmentalize reagents into individual droplets with low or no chemical cross-talk, and (3) the ability to miniaturize chemical and biological processes to reduce reagent consumption and handle low volume samples. However, droplet-based microfluidics has relied on closed microfluidic systems, pumps, and actuators that make the development, fabrication, and use of these systems more challenging.

Capillary-driven open microfluidic systems have gained popularity as they alleviate some of the challenges of closed microfluidic systems. The considerable development in understanding surface tension driven flows in open channels as well as filament flows,[2–14] flows in fibrous systems,[15–17] and the development of applications[18–21] of open microfluidic flows has driven a gain in popularity of the field of open microfluidics. The use of passive capillary forces to drive fluids eliminates the need for external pumping equipment, which is critical for applications in low resource settings[22–25] and for easy translation to biology laboratories.[26,27] While capillary flows in closed cylindrical tubes have been known since the first studies of Lucas, Washburn, Rideal and Bosanquet,[28–31] the fundamentals of capillarity in closed channels of arbitrary shape is more recent.[32–34] Moreover, the ability to use capillary flows in open channels, i.e., open microfluidics, has uniquely enabled new applications.[19–21] Open channels, which lack a ceiling or both a floor and a ceiling,[20,33] are fully accessible so fluids, cells, or tissue can be added at any point along the channel by simply pipetting from the top. Further, open microfluidic devices can be fabricated in a single step with methods such as micromilling and injection molding since they do not require bonding of multiple layers. Finally, open microfluidic systems are reliable as air-bubbles and bonding-defects are alleviated.

The physics of two-phase capillary flows as well as the behavior of immiscible droplets or plugs in an open capillary flow, however, remains largely unexplored. Recent publications have started to explore the creation of biphasic flows in syringe-pump driven, paper-based systems.[34] The application of open capillary-driven systems for droplet microfluidics promises to yield enabling features including simplicity of manufacturing and access to droplets in real time.

However, multiple challenges must be overcome to create functional droplets in open microfluidics specifically regarding droplet generation and droplet manipulation. As the open

systems are driven by surface tension forces, the question arises: how does a plug of aqueous liquid behave in the presence of a solvent flowing via SCF in an open channel? We present an analytical model for two-phase capillary flows based on the resulting capillary force deduced from Young's law. We further investigate the modes of fluid movement around a plug using numerical simulations and experiments. We find conditions that enable the translation of an aqueous plug along an open channel by an organic solvent carrier phase, analogous to prior work in closed channel droplet-based microfluidics. Finally, we show droplet formation and reagent addition based on simple pipetting steps, underscoring the accessibility of capillary driven droplet-based microfluidics in open channels.

2.3 Results and Discussion

References to Supporting information (SI) can be found in Appendix A

2.3.1 *Analytical model of an immiscible plug in a spontaneous capillary flow.*

Open microfluidics describes the flow of fluid in channels that have one or more open faces and have demonstrated enabling properties in terms of increased reliability, accessibility, and ease of fabrication.[20] Previous work has determined design conditions to obtain passive surface tension driven flow in open channels and named that type of capillary flow "spontaneous capillary flow" (SCF). The nomenclature "spontaneous capillary flow" has been used to specify channels in which typical capillary flow conditions (i.e., for closed channels) do not apply and with an inlet pressure of zero. Specifically, the conditions for SCF to occur are based on the ratio of the cross-sectional perimeter that is open to the air vs. perimeter comprised of solid material (channel walls), as well as the contact angle of the fluid on the channel surface.[20,35]

A generalized condition for SCF has been developed when the material properties of the channel walls are not the same along the whole cross section (e.g., when the fluid contacts at least two surfaces with different contact angles), called the generalized Cassie angle.[36] Further, dynamic analyses of fluids in open microfluidic channels have been developed to understand the velocity of the fluid front in SCF flows, similar to the Lucas-Washburn-Rideal laws for velocities of capillary flow in closed microfluidics.[37]

While the conditions for SCF in single phase open microfluidic systems have been well characterized,[14,20] the effect of a plug of immiscible fluid placed in the path of the carrier fluid in an open microchannel has not been studied to date. We developed an analytical model considering a plug contacted by a spontaneous capillary flow (SCF) of an immiscible carrier liquid (detailed in Section 1 of the SI). We performed an analysis of the resultant of the capillary forces on the floor of the channel as the carrier fluid meets the plug, or when a plug is embedded in the carrier fluid (based on the Young contact angles). We find that any two-phase configuration can be simplified into an equivalent configuration containing a single phase (see SI section 1). Thus, in the case of a channel of constant cross section, the presence of the plug does not affect the occurrence of SCF of the carrier fluid. Note that the analysis is based on a static or quasi-static situation, which is valid for determination of a possible SCF. The dynamics of the flow, however, may be affected by the presence of a plug.

2.3.2 *Numerical simulations.*

Numerical simulations reveal three characteristic behaviors of open biphasic flows. We used 3D surface energy minimization software (*Surface Evolver*)[38] to determine how the flow of a carrier fluid would interact with an existing immiscible plug placed in an open microfluidic channel. Note that Evolver does not account for the dynamics of the flow, but its use is valid to

determine a possible SCF.[14,36] Using *Surface Evolver* we modeled a rectangular open microchannel containing a plug and added a carrier fluid flowing by SCF along the channel. The simulations confirm that the plug does not prevent the flow from occurring and reveal three different behaviors of the plug: (1) a 'shift' mode where the plug is horizontally displaced and translates in front of the carrier fluid flow, (2) a 'bridge' mode where the plug stays in place on the floor of the channel and the capillary flow of the carrier fluid flows above the plug, and (3) a 'lift' mode where the plug is lifted but maintains contact with both sides of the channel and the carrier fluid flows underneath. These simulations and corresponding schematics are detailed in Figure 2.1. The parameter space to explore is large and based on five main variables, namely the contact angle of the carrier fluid, θ_1, the contact angle of the plug fluid, θ_2, the surface tension between the carrier fluid and air, γ_{L1A}, the surface tension between the plug fluid and air, γ_{L2A}, and the interfacial tension between the two fluids, γ_{L1L2}. Note that the two-phase-wall contact angle θ_{12} is deduced from these five parameters (see SI section 1). We attempt to identify here the general conditions using these parameters that lead to the different modes.

Bridge mode is characterized by the plug maintaining contact on the bottom of the channel while the carrier fluid flows above it. In the case of an aqueous plug, this mode occurs when the plug surface tension γ_{L2A} is high compared to the oil surface tension and oil-water interfacial tension, as shown in Table S2.1. Such configuration is usually accompanied by a high value of θ_{12}. Lift mode is characterized by the plug maintaining contact on both sides of the channel but lifting to the top of the groove allowing the carrier fluid to flow underneath. This behavior occurs in the simulations at relatively large contact angles of the plug with the channel material θ_2, as shown in Table S2.1. Shift mode is characterized by the plug remaining at the front of the advancing carrier fluid and maintaining contact with the channel on all sides. Other behaviors of the plug might exist

as we have not performed an exhaustive search through the large parameter space. For example, a condition in which the plug entirely detaches from walls of the channel, forming a raft mode, is hypothesized to be possible via interfacial tension forces alone.

2.3.3 *Experimental observations.*

In order to characterize the behavior of a plug of aqueous fluid placed in an open microfluidic channel while an immiscible solvent flows past it via capillary-driven flow, we designed two channels to view the plug geometry from the top and the side (Figure 2.2Ai and 2.2Aii). Several design considerations were respected: (1) To minimize the potential for pressure-driven artifacts (for example during additions of fluid by pipetting or due to Laplace pressure created at the inlet[39,40]), the inlet was designed with a large radius, allowing the entire channel to fill with a single pipetting step and minimizing Laplace pressure, which occurs when the surface of the liquid in the reservoir is flat. (2) To make the flow of solvent more controllable and predictable, the potential for Concus-Finn filament formation was removed by designing a channel without angles in the cross section (in this case we used a rounded U-shaped cross section).[2,3] Concus-Finn filaments typically occur in the wedges of channels with a rectangular cross section and their properties (velocity, length) can be challenging to predict.[5,6] (3) In order to ensure that the behavior of the plug in the immiscible solvent is dominated by interfacial tension forces instead of gravitational forces, we selected channel dimensions (and in particular the width, w) such that the Bond number would be lower than 1 for the fluids used in this work. The Bond number is a dimensionless number that estimates the relative magnitude of the interfacial tension forces acting on the surface of a droplet compared to the gravitational forces acting on the volume of the droplet (the Bond number calculations can be found in section 5.1 of the SI). (4) In order to view the behavior of the plug, the channels were optimized for the imaging angle. The top view channel

(Figure 2.2Ai) was optimized to image a long section of the open channel, while the side view channel (Figure 2.2Aii) was designed to have a thin transparent 2 mm wall allowing side-view imaging.

We characterized the flow of the solvents in our open channels without the presence of an immiscible plug and measured the rate of advancement of the fluid front in the channel (Figure 2.2C and 2.22D). The velocity of the solvent front decreases along the channel as would be expected from a capillary-driven flow. Further, the velocity is decreased as a function of the increasing viscosity of the carrier fluid. In order to reduce dynamic and inertial effects of the solvent on a plug placed in the open microfluidic channel, we placed the aqueous plugs at a sufficient distance from the inlet of the channel where the velocities of the solvent are decreased. Shift mode was observed in cases where the interfacial tension between the carrier fluid and the plug is relatively low (Table 2.1), such as the case of 1-nonanol and water (interfacial tension: 8.5 mN/m) shown in Figure 2.3. As shown in Figure 2.3, shift mode occurred as predicted by numerical simulation with the plug being translated down the channel by the advancing solvent front. In a subset of cases, we observed that shift mode displayed a non-continuous behavior, in which the plug alternatively advances and stops (for example, when 1-pentanol is used as a carrier phase (SI Figure S3.1). Bridge mode was observed experimentally in cases where the interfacial tension between the carrier fluid and plug is relatively high (e.g., 52.8 mN/m for n-dodecane and water, see other examples in Table 2.1). As shown in Figure 2.4, during bridge mode the plug remained stationary within the channel, and the solvent flowed over the plug. Importantly, we observed bridge mode irrespective of the density of the carrier phase relative to the plug (which is to be expected given the low Bond number design of the open microfluidic channel); bridge mode was observed with both n-dodecane (density = 0.75 g/mL) and FC-40 fluorinated oil (density =

1.85 g/mL) carrier fluids with an aqueous plug (density = 1.0 g/mL). Lift mode was not observed for the solvents tested; as noted, numerical simulations predict the need for a high contact angle of both the plug and carrier fluid which presents significant experimental challenges to implement.

Transition between interfacial tension dominated conditions to inertial conditions. The numerical simulations provided an accurate representation of the behavior of the plug in low velocity conditions where interfacial tension forces dominate. As velocities increase, different behaviors are observed. We demonstrate the transition from low velocity (interfacial tension dominant) to higher velocity behaviors (with significant contribution from inertial forces) by placing a plug at different locations in the open microfluidic channel. Closer to the inlet, the plug will experience higher velocities of the carrier fluid (Figure 2.2D).[37] Further in the channel, the plug will experience lower velocities of the carrier fluid due to the fluidic resistance of the channel from the location of the plug to the inlet. The experiments performed in the previous section (Figures 2.3 and 2.4; Table 2.1) occurred at low velocity regimes, close to the end of the channel.

We placed a plug of water at different locations in the channel and demonstrated new behaviors of the plug in a flow of toluene (Figure 2.5). At low velocities, the plug typically displays a static bridge behavior. When the aqueous plug is placed further upstream, the plug can be induced to move downstream as the toluene solvent flows over it. This behavior is not observed every time and can depend on the exact positioning of the plug in the channel as well as the precise volume and spread of the droplet. We named this behavior "bridge-translate," as the main characteristics of bridge mode are maintained as the plug is displaced downstream. At even higher velocities, when the plug is placed close to the inlet, the plug is detached from all surfaces of the channel and forms a raft that moves rapidly with the carrier fluid. A similar phenomenon was observed with 1-pentanol as the carrier fluid, which typically displays a shift behavior at low velocities and

transforms into raft behavior at higher velocities (Figure S4.1). Several forces on the plug may explain these differences in behaviors, in particular (1) the inertia of the carrier fluid pushing the plug as the flow lines deform to move around the plug and modifies the θ_{12} contact angle, and (2) the shear of the carrier fluid applying force on the plug as the two fluids flow simultaneously.

We extrapolate the observations made at different velocities to hypothesize a general rule detailing the behavior of immiscible fluids in open microfluidic channels under SCF (Figure 2.6). In interfacial tension dominated conditions, such as those occurring in low velocity regions of the channel, four plug-behaviors are hypothesized / demonstrated: (1) shift (numerically and experimentally demonstrated, Figures 2.1 and 2.3), (2) bridge (numerically and experimentally demonstrated, Figures 2.1 and 2.4), (3) lift (determined numerically (Figure 2.1), not found experimentally), and (4) raft (hypothesized in the case of interfacial tension dominant conditions). As velocities and inertial forces of the carrier fluid on the plug increase, bridge and lift mode display a translation movement downstream while maintaining their bridge or lift behavior (observed experimentally for bridge mode (Figure 2.5B), hypothesized for lift mode). At even higher velocities, all behaviors are replaced by a raft mode in which the plug detaches from the walls of the channel and flow downstream with the carrier fluid (observed experimentally for shift mode (Figure S4.1B) and bridge mode (Figure 2.5C).

In order to establish a semi-quantitative guideline to determine conditions in which the inertial dominant modes occur, and to facilitate open microchannel design, we adapted the Weber number characterizing the ratio between inertial and interfacial tension forces for open microfluidic biphasic flows (see SI section 5.3). Specifically, we wrote an expression of the modified Weber number as a function of geometrical parameters (channel width, w, average friction length, λ, and position of the plug in the channel, z), properties of the carrier fluid (density,

ρ, interfacial tension, γ, and viscosity, μ), and the generalized Cassie angle for the fluid in the open microfluidic channel (θ*).[36] We displayed the calculation of the modified Weber number for a range of solvents used in this work (e.g., 1-pentanol, toluene, chloroform, FC-40) and found that the inertial modes (translate and raft modes) observed had a good correlation with modified Weber numbers greater than 1. Specifically, at locations in the channel of around 100 times the average friction length (i.e., 15 mm from the inlet) the modified Weber number for chloroform and toluene is approximately 3.28 and 1.77, respectively. Experimentally, both of these solvents placed towards the inlet of the channel display raft mode (with chloroform displaying a transition to raft mode more rapidly than toluene). Further down the channel at locations of around 1000 times the average friction length (i.e., 150 mm from the inlet), the modified Weber numbers calculated are lower, and we observe different degrees of influence of inertial forces (with toluene displaying a bridge-translate mode, and chloroform displaying both a bridge-translate and raft behavior). In general, the modified Weber number appears to be a good predictor of the behavior of immiscible plugs in an SCF flow. Using this tool, it is possible to design SCF flows that maintain interfacial tension dominated behaviors such as bridge or lift, or force modes in which the plugs are detached from the wall.

Applying behaviors for compartmentalized flow applications. A key feature of droplet-based microfluidics is the ability to create multiple droplets or plugs in sequence, compartmentalized by an immiscible carrier phase. Here, we demonstrate for the first time that capillary-driven flow in open microfluidic channels enables the creation and manipulation of multiple plugs in sequence in an open microfluidic channel. First, an immiscible carrier phase, in this case 1-pentanol, is pipetted into the device inlet. The 1-pentanol flows down the open channel based on SCF. Plug formation is achieved by simply pipetting aqueous phase directly into a

capillary-driven flow of 1-pentanol (Figure 2.7B and C). In Figure 2.7, a repeat pipette is used to create aqueous plugs. Since the system is fully open and accessible from the top, in the future it could be coupled with any type of liquid handling system.

An important consequence of using open channels is that the plugs can be accessed directly from the top at any location in the channel. In Figure 2.7E and F we demonstrate that reagents can be selectively added to targeted plugs simply by pipetting into the plugs while they flow past. For visualization, we formed yellow plugs and added red dye into every other plug, forming an alternating train of yellow and orange plugs. In closed channel droplet-based microfluidics numerous solutions have been developed to add reagents into droplets after formation, including electrofusion[45] and picoinjection,[46] however these require specific channel designs or the addition of electronic components. With open microfluidics, it is not necessary to engineer new approaches to add reagents; the accessibility of the open channel enables reagents to be added on demand using existing pipettes or other liquid handlers. Interestingly, the open aspect of the channels not only enables the addition or removal of fluids from the droplets, but also the addition of particles, magnetic beads, or cells, opening a vast range of novel applications for compartmentalized biphasic microfluidics.

2.4 Materials and Methods

2.4.1 *Numerical simulation.*

Surface Evolver was utilized to perform simulations of surface energy minimization in the presence of two immiscible fluids: a plug of aqueous fluid and an incoming solvent. A geometry was generated displaying a section of an open microfluidic channel with a rectangular cross section. The channel displayed in the simulation is 2.5 cm long, 0.8 mm wide, and 1.3 mm deep.

The cross section is a rectangular cross section for simplicity. The parameters of the fluids were varied to observe different behaviors of the plug and defined as γ_{L1A}, the surface tension between the carrier fluid and air; γ_{L2A}, the surface tension between the plug fluid and air; γ_{L1L2}, the interfacial tension between the two fluids; θ_1, the contact angle of the carrier fluid on the channel surface; θ_2, the contact angle of the plug on the channel surface (SI Table S2.1).

2.4.2 *Channel fabrication.*

In all experiments, the devices were fabricated using a Tormach PCNC 770 Mill (Tormach, Waunakee, WI) on poly(methyl methacrylate) (PMMA) sheets with a thickness of 3.175 mm (McMaster-Carr, Santa Fe Springs, CA). The design of the devices, as shown in Figure 2.2Ai-ii, was created using the computer aided design (CAD) software Solidworks 2016 (Solidworks, Waltham, MA). The CAD design files were converted to machine code, G-code, using the computer aided manufacturing (CAM) software SprutCAM (SprutCAM, Naberezhnye Chelny, Russia). Schematics of the designs are included in section 6 of the SI. The devices were rinsed with deionized (DI) water and sonicated in 70% ethanol for 10 minutes, followed by a second rinse with DI water. The channels were dried with compressed air and used immediately.

2.4.3 *Channel dimensions.*

Channels in all experiments were 1.5 mm deep and 0.8 mm wide, with a U-shaped cross section (shown in Figure 2.2Bii) to avoid Concus-Finn capillary filaments. The channel for top view imaging (Figure 2.2Ai, 2.3A, 2.4A, 2.7Ai, and 2.7Di) was 366 mm long; the circular inlet reservoir had a diameter of 30 mm and depth of 1.0 mm. The channel for side view imaging (Figure 2.2Aii, 2.3B, and 2.4B) was 60 mm long; the circular inlet reservoir had a diameter of 10 mm and depth of 1.0 mm. For the top view imaging experiment using toluene in Figure 2.5, the channel

was lengthened to 454 mm long. For side view imaging experiments in Figure 2.7Aii and Figure 2.7Dii, the channel was 205 mm long; the circular inlet reservoir had a diameter of 18 mm and depth of 1.0 mm.

2.4.4 *Materials.*

DI water (Water Deionized Distilled Type II (Harleco), chloroform, and toluene were purchased from Fisher Scientific. FC-40, n-dodecane, and 1-nonanol were purchased from Sigma-Aldrich. 1-Pentanol was purchased from Across Organics. DI water was colored with yellow dye from Spice Supreme at a volume/volume percentage of 10%. For Figure 2.7D, DI water was colored with red dye from Spice Supreme at a volume/volume percentage of 1%. The organic solvents were colored with Oil Blue N from Sigma-Aldrich at concentrations of 1.43 mg/mL (n-dodecane, 1-nonanol, and 1-pentanol) and 0.24 mg/mL (chloroform and toluene). FC-40 was not colored and was used as purchased from the manufacturer.

2.4.5 *Imaging.*

Top view images were recorded using an Amscope MU1403B High Speed Microscope Camera mounted on an Amscope SM-3TZ-80S stereoscope (Amscope, Irvine, CA). Side view images were recorded using a Nikon-D5300 Ultra-High-Resolution SLR camera.

2.4.6 *Contact angle measurements.*

The contact angles of solvents on PMMA (Table 2.1) were measured using a Krüss DSA-25 goniometer (Krüss GmbH, Hamburg, Germany). The average measurement of 2.0 μL droplets (n = 5) were made with Krüss ADVANCE Software using an ellipse shape fitting method and an automatic baseline generated by the software. The organic solvents were colored with Oil Blue N

from Sigma-Aldrich at concentrations of 1.43 mg/mL (n-dodecane, 1-nonanol, and 1-pentanol) and 0.24 mg/mL (chloroform and toluene). FC-40 was not colored and was used as purchased from the manufacturer.

2.4.7 *Characterization.*

For all experiments (excluding Figure 2.7) a 3.0 μL plug of DI water was placed in the channel. The inlet reservoir was filled with 950 μL of organic solvent for the top view imaging device (Figure 2.1Ai) and 150 μL for the side view imaging device (Figure 2.1Aii). In the toluene experiment (Figure 2.5) the inlet reservoir was filled with 1000 μL of toluene.

Sequential plug formation experiment. The inlet reservoirs were filled with 950 μL and 300 μL of 1-pentanol for the top and side view imaging devices, respectively (Figure 2.7A), followed by addition of droplets of 3.0 μL DI water (with yellow dye) on top of the solvent as 1-pentanol flowed along the channel. A repeat pipette was used to create additional drops at the desired intervals. To add additional fluid to existing droplets, a second repeat pipette containing DI water with red dye was used to pipette 3.0 μL of red dye into a yellow droplet as it was flowing down the channel in the carrier fluid, 1-pentanol.

2.5 CONCLUSION

We demonstrate that open microfluidic channels allow the formation of capillary-driven biphasic flows. We characterize the behavior of aqueous plugs in the presence of a capillary-driven flow of immiscible solvent and demonstrate two plug behaviors: shift and bridge modes. We further show that these interfacial tension dominated modes are affected by inertial forces of the carrier fluid resulting in the emergence of new modes, such as raft mode, at higher velocities. We show that these modes can be leveraged to create open droplet microfluidic systems in which

segregated plugs of aqueous fluid flow along an immiscible carrier solvent. We envision that traditional closed-channel droplet-based microfluidics still offers significant advantages for high-throughput applications due to the high droplet frequencies and small droplet volumes achievable. However, advanced fluid handling systems such as acoustic droplet ejection may offer volume controls for open biphasic applications on par with closed systems. Further, key features of open droplet-based microfluidics such as a reduced set of equipment and fabrication requirements and accessibility to the droplets at any point in the channel will be enabling in chemistry, biology, and engineering applications.

2.6 FIGURES

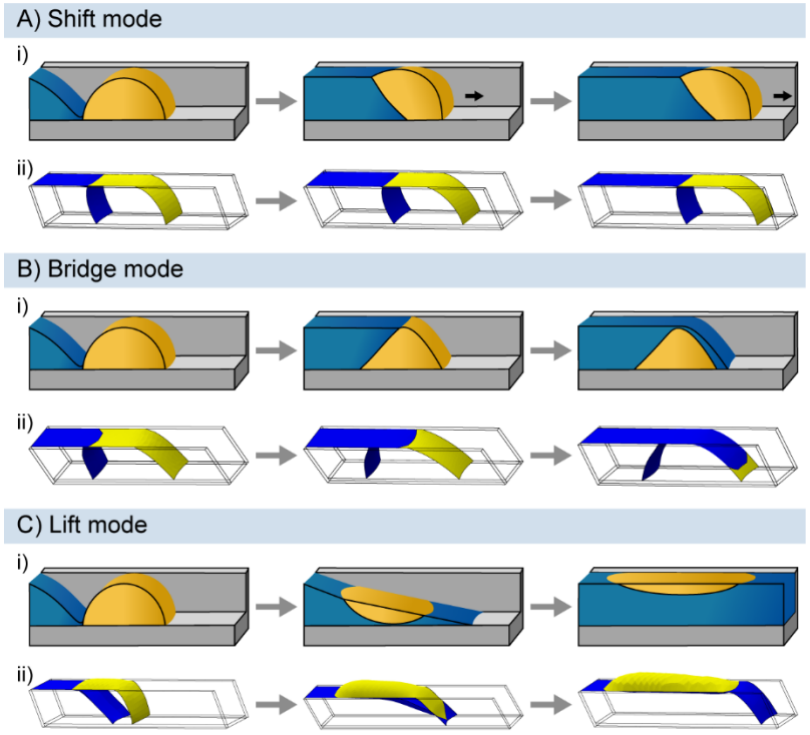

Figure 2.1 Theoretical interactions of a carrier fluid (blue) and an immiscible plug (yellow) in an open microfluidic channel, characterized into three modes. Schematic representations (i) and numerical simulations using the Surface Evolver software (ii) of shift, bridge, and lift modes demonstrating interactions of the solvent and plug at initial contact, at early interaction of the phases, and after extended contact between the two phases. The parameters used for the Surface Evolver simulations are given in Table S2.1.

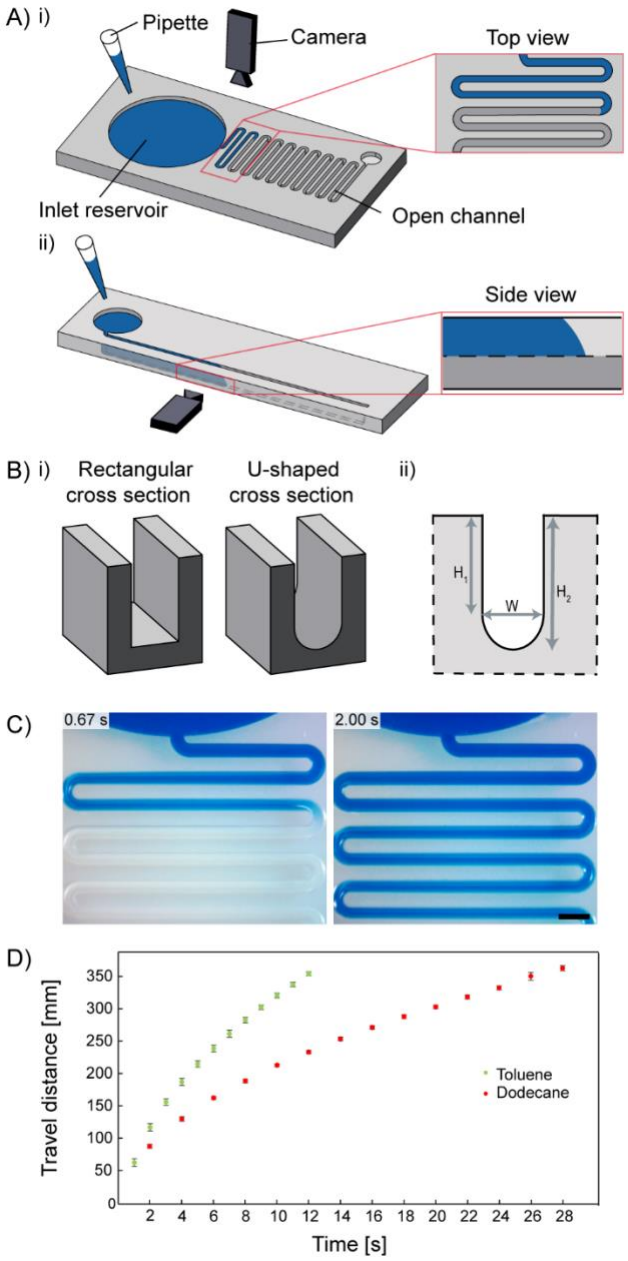

Figure 2.2. (A) Experimental setup with the different devices for top view (i) and side view (ii) imaging. (B) The bottom of the devices has a U-shaped cross section rather than a rectangular cross section to avoid Concus-Finn flow2,3 of the solvent in the channel (i). Cross section of the devices where H1 is 1.1 mm, H2 is 1.5 mm, and W is 0.80 mm (ii). (C) Top view images of spontaneous capillary flow of toluene in an open microfluidic channel with a U-shaped cross section at two different time points. The scale bar is 2 mm. (D) Measured values of the location of toluene and dodecane solvent fronts in an open microfluidic channel as a function of time. The plotted points are the average of three independent experiments, with error bars representing the standard deviations.

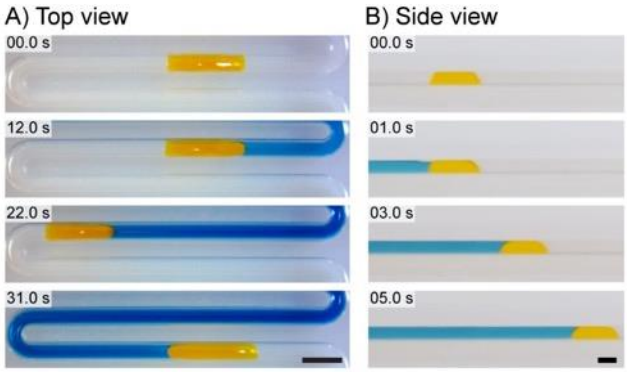

Figure 2.3. Experimental visualization of shift mode using an aqueous plug (yellow) and 1-nonanol as the carrier phase (blue) from the top view (A) and side view (B). Images are representative of three replicate experiments. The scale bar is 2 mm.

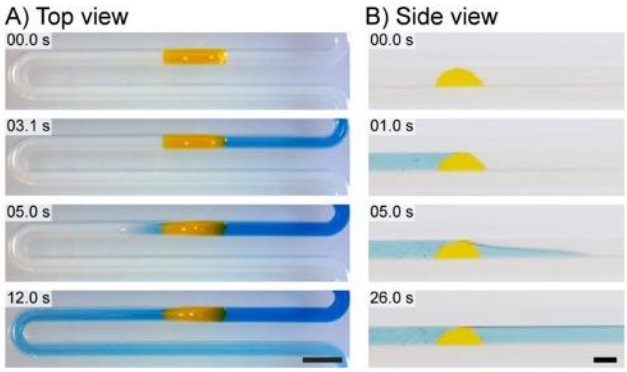

Figure 2.4. Experimental visualization of bridge mode using an aqueous plug (yellow) and n-dodecane as the carrier phase (blue) from the top view (A) and side view (B). Images are representative of three replicate experiments. The scale bar is 2 mm.

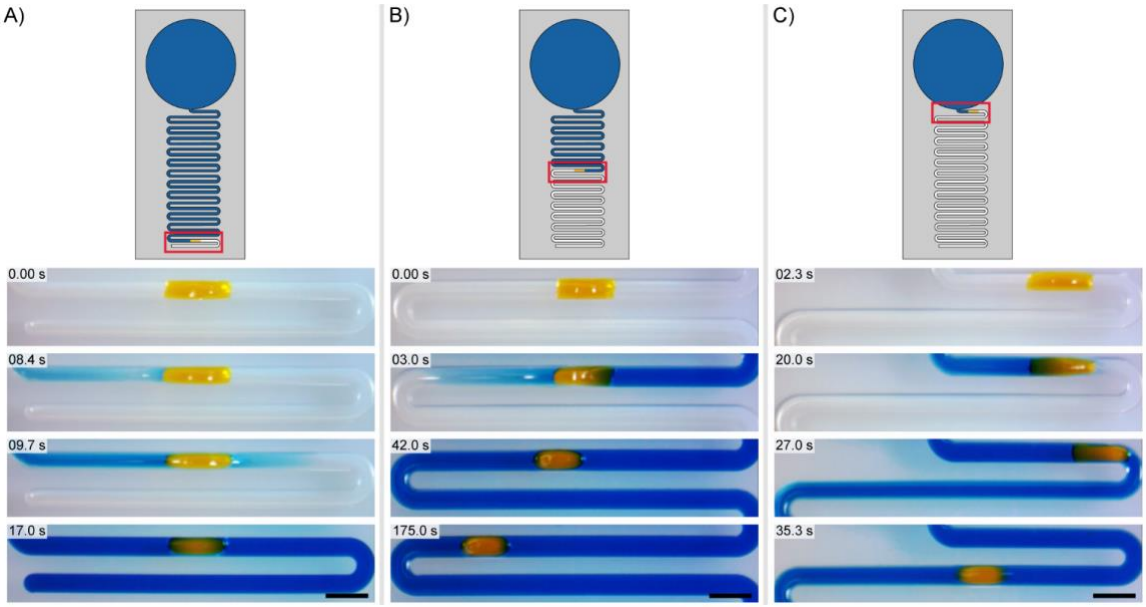

Figure 2.5. Experiment with toluene as the carrier fluid (blue) and an aqueous plug (yellow) at three different locations in the channel. (A) Plug in a low velocity region showing bridge mode. (B) Plug in a mid-velocity region showing bridge-translate mode. (C) Plug in a high velocity region showing raft mode. Images are representative of three replicate experiments, and scale bar is 2 mm.

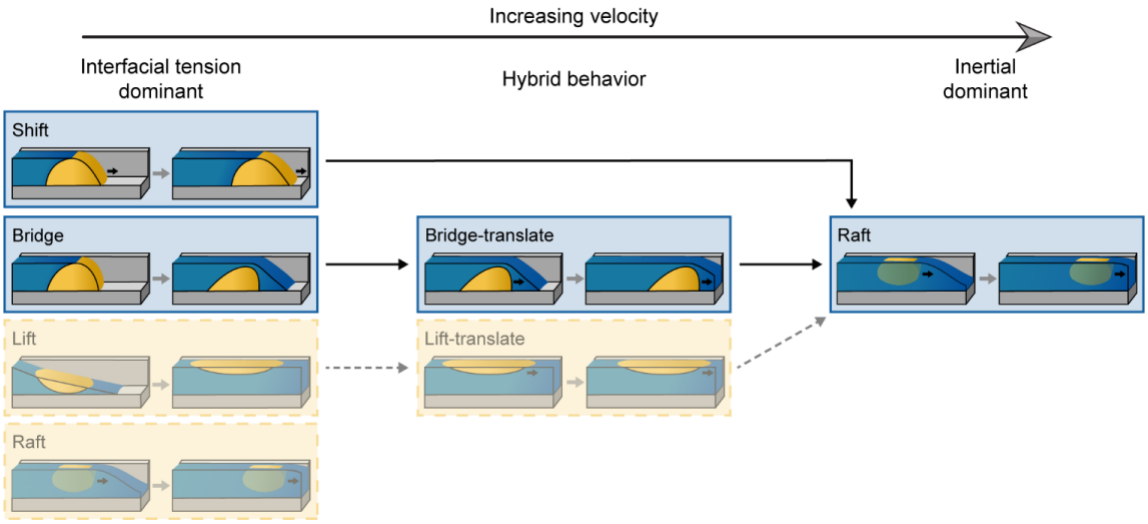

Figure 2.6. A model demonstrating the effect of velocity on the interaction between a carrier fluid and an immiscible plug in an open microfluidic channel. At lower velocity, the interactions are dominated by interfacial tension, and as velocity increases the interactions become dominated by inertia. At mid-velocity regions, transitions between certain low velocity modes and raft mode are observed. These modes are described as "translates" as they have not fully detached from the walls of the channel (which defines raft mode) but are still moving down the channel, which is uncharacteristic of the low velocity modes (excluding shift). Lift and lift-translate modes have not been observed experimentally, and thus are boxed with dashed lines and shown in yellow. Raft mode has been observed at high velocities, but has only been hypothesized to occur under interfacial tension dominated regions.

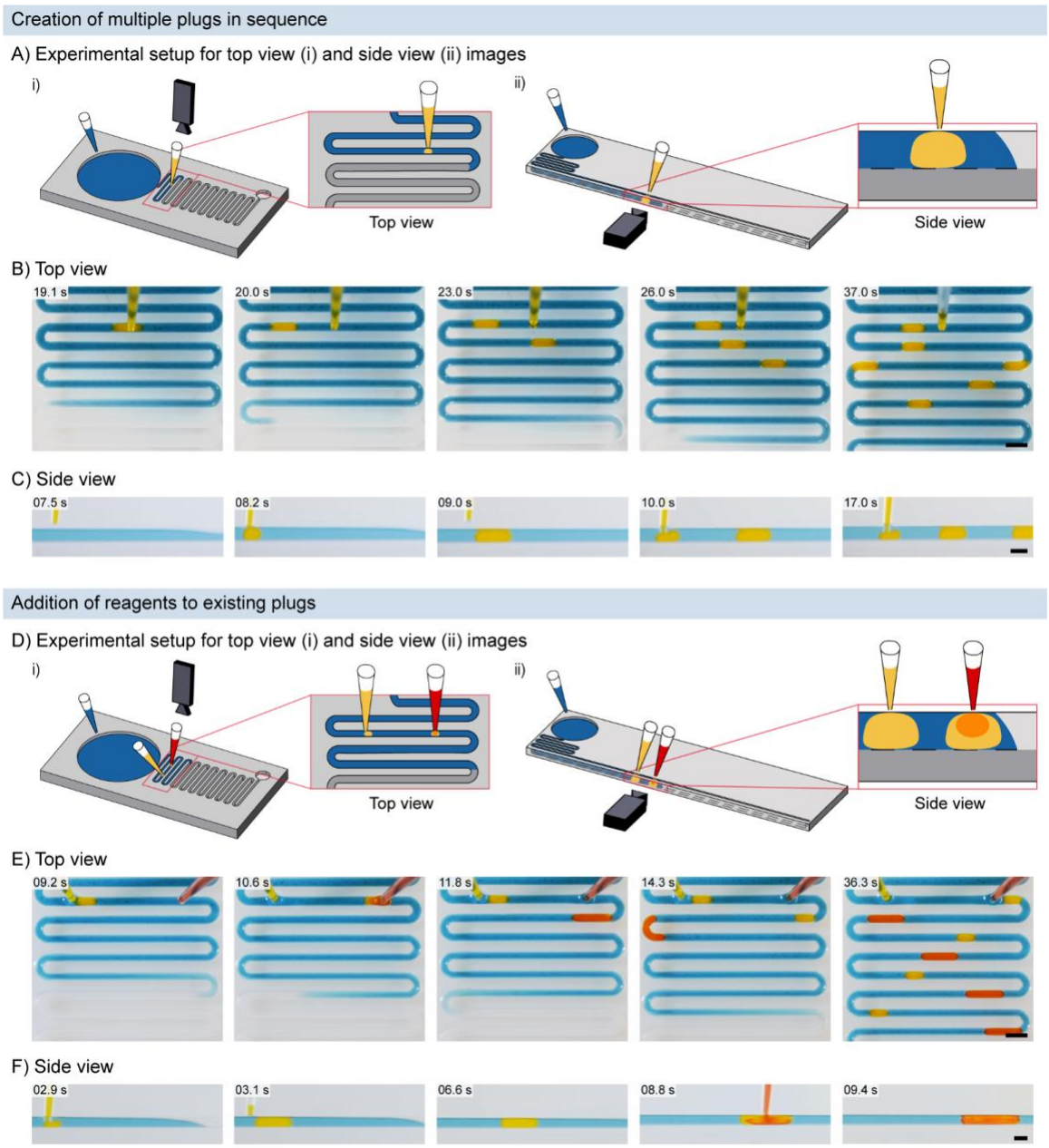

Figure 2.7. Sequential plug formation in an open microfluidic channel. The carrier solvent is 1-pentanol with blue dye; the droplets are water with yellow or red dye. Scale bars are 2 mm. (A-C) Schematic of the devices used for top and side view imaging and images of the formation of sequential plugs in these devices. (D-F) Demonstration of the ability to add fluid to a plug using a simple pipette. Every other yellow water droplet is selected, and a bolus of red-colored water is added.

2.7 TABLES

Table 2.1. Surface tension between carrier fluid and air[43–45] (γ_{L1A}), interfacial tension between carrier fluid and water[46] (γ_{L1L2}), contact angle of carrier fluid with PMMA (θ_1), and mode observed in open biphasic microfluidic experiments.

Carrier fluid	γ_{L1A}[a]	γ_{L1L2}[a]	θ_1[b]	Modes observed
1-Pentanol	25.4	4.4	12.5 ± 3.0	Shift[f]
1-Nonanol	26.4[c]	8.5	17.0 ± 1.6	Shift
Chloroform	27.5[d]	32.8[c]	17.3 ± 1.1	Bridge[f]
Toluene	28.4	36.1	7.8 ± 1.7	Bridge[f]
FC-40	16.0	52.1[e]	12.7 ± 1.3	Bridge
n-Dodecane	25.4	52.8	26.7 ± 0.7	Bridge

[a]In units of mN/m at 25°C unless otherwise indicated. [b]In units of degrees (n=5), measured experimentally (see Experimental section for details including concentration of dye added to the organic solvents). [c,d,e]At 20°C, 27°C, and 23°C, respectively. [f]These are the modes observed at low velo cities of the carrier fluid. For these solvents different modes have been observed at higher velocities (Figure 2.5).

2.8 REFERENCES

1. Shang, L.; Cheng, Y.; Zhao, Y. Emerging Droplet Microfluidics. Chem. Rev. 2017, 117, 7964–8040.
2. Concus, P.; Finn, R. On the Behavior of a Capillary Surface in a Wedge. Proc. Natl. Acad. Sci. U. S. A. 1969, 63, 292–299.
3. Concus, P.; Finn, R. Capillary Surfaces in a Wedge-DifferingContact Angles. Microgravity Sci. Technol. 1994, 7, 152–155.
4. Weislogel, M. M.; Chen, Y.; Bolleddula, D. A Better Nondimensionalization Scheme for Slender Laminar Flows: The Laplacian Operator Scaling Method. Phys. Fluids 2008, 20, 93602.
5. Berthier, J.; A. Brakke, K.; Gosselin, D.; Huet, M.; Berthier, E. Metastable Capillary Filaments in Rectangular Cross-Section Open Microchannels. AIMS Biophys. 2014, 1, 31–48.
6. Mann, J. A.; Romero, L.; Rye, R. R.; Yost, F. G. Flow of Simple Liquids down Narrow V Grooves. Phys. Rev. E 1995, 52, 3967–3972.
7. Rye, R. R.; Yost, F. G.; Mann, J. A. Wetting Kinetics in Surface Capillary Grooves. Langmuir 1996, 12, 4625–4627.
8. Romero, L. A.; Yost, F. G. Flow in an Open Channel Capillary. J. Fluid Mech 1996, 1, 109–129.
9. Yost, F. G.; Rye, R. R.; Mann, J. A. Solder Wetting Kinetics in Narrow V-Grooves. Acta Mater. 1997, 45, 5337–5345.

10. Baret, J.-C.; Decré, M. M. J.; Herminghaus, S.; Seemann, R. Transport Dynamics in Open Microfluidic Grooves. Langmuir 2007, 23, 5200–5204.
11. Kitron-Belinkov, M.; Marmur, A.; Trabold, T.; Dadheech, G. V. Groovy Drops: Effect of Groove Curvature on Spontaneous Capillary Flow. Langmuir 2007, 23, 8406–8410.
12. Yang, D.; Krasowska, M.; Priest, C.; Popescu, M. N.; Ralston, J. Dynamics of Capillary-Driven Flow in Open Microchannels. J. Phys. Chem. C 2011, 115, 18761–18769.
13. Ouali, F. F.; McHale, G.; Javed, H.; Trabi, C.; Shirtcliffe, N. J.; Newton, M. I. Wetting Considerations in Capillary Rise and Imbibition in Closed Square Tubes and Open Rectangular Cross-Section Channels. Microfluid. Nanofluidics 2013, 15, 309–326.
14. Berthier, J.; Brakke, K. A.; Berthier, E. Open Microfluidics. 2016, 1–11.
15. Reches, M.; Mirica, K. A.; Dasgupta, R.; Dickey, M. D.; Butte, M. J.; Whitesides, G. M. Thread as a Matrix for Biomedical Assays. ACS Appl. Mater. Interfaces 2010, 2, 1722–1728.
16. Nilghaz, A.; Ballerini, D. R.; Shen, W. Exploration of Microfluidic Devices Based on Multi-Filament Threads and Textiles: A Review. Biomicrofluidics 2013, 7, 51501.
17. Berthier, J.; Brakke, K. A.; Gosselin, D.; Berthier, E.; Navarro, F. Thread-Based Microfluidics: Flow Patterns in Homogeneous and Heterogeneous Microfiber Bundles. Med. Eng. Phys. 2017, 48, 55–61.
18. Conrath, M.; Canfield, P. J.; Bronowicki, P. M.; Dreyer, M. E.; Weislogel, M. M.; Grah, A. Capillary Channel Flow Experiments Aboard the International Space Station. Phys. Rev. E 2013, 88, 63009.
19. Barkal, L. J.; Theberge, A. B.; Guo, C.-J.; Spraker, J.; Rappert, L.; Berthier, J.; Brakke, K. A.; Wang, C. C. C.; Beebe, D. J.; Keller, N. P.; et al. Microbial Metabolomics in Open Microscale Platforms. Nat. Commun. 2016, 7, 10610.
20. Casavant, B. P.; Berthier, E.; Theberge, A. B.; Berthier, J.; Montanez-Sauri, S. I.; Bischel, L. L.; Brakke, K.; Hedman, C. J.; Bushman, W.; Keller, N. P.; et al. Suspended Microfluidics. Proc. Natl. Acad. Sci. U. S. A. 2013, 110, 10111–10116.
21. Berthier, J.; Brakke, K. A.; Furlani, E. P.; Karampelas, I. H.; Poher, V.; Gosselin, D.; Cubizolles, M.; Pouteau, P. Whole Blood Spontaneous Capillary Flow in Narrow V-Groove Microchannels. Sensors Actuators, B Chem. 2015, 206, 258–267.
22. Juncker, D.; Schmid, H.; Ute, D.; Heiko, W.; Marc, W.; Bruno, M.; Nico, de R.; Emmanuel, D. Autonomous Microfluidic Capillary System. Anal. Chem. 2002, 74, 6139–6144.
23. Yager, P.; Edwards, T.; Fu, E.; Helton, K.; Nelson, K.; Tam, M. R.; Weigl, B. H. Microfluidic Diagnostic Technologies for Global Public Health. Nature 2006, 442, 412–418.
24. Gervais, L.; Delamarche, E. Toward One-Step Point-of-Care Immunodiagnostics Using Capillary-Driven Microfluidics and PDMS Substrates. Lab Chip 2009, 9, 3330–3337.
25. Safavieh, R.; Juncker, D. Capillarics: Pre-Programmed, Self-Powered Microfluidic Circuits Built from Capillary Elements. Lab Chip 2013, 13, 4180–4189.
26. Gervais, L.; de Rooij, N.; Delamarche, E. Microfluidic Chips for Point-of-Care Immunodiagnostics. Adv. Mater. 2011, 23, H151–H176.
27. Nilghaz, A.; Ballerini, D. R.; Guan, L.; Li, L.; Shen, W. Red Blood Cell Transport Mechanisms in Polyester Thread-Based Blood Typing Devices. Anal. Bioanal. Chem. 2016, 408, 1365–1371.

28. Lucas, R. Ueber Das Zeitgesetz Des Kapillaren Aufstiegs von Flüssigkeiten. Kolloid-Zeitschrift 1918, 23, 15–22.
29. Washburn, E. W. The Dynamics of Capillary Flow. Phys. Rev. 1921, 17, 273–283.
30. Rideal, E. K. On the Flow of Liquids under Capillary Pressure. Philos. Mag. Ser. 6 1922, 44, 1152–1159.
31. Bosanquet, C. H. On the Flow of Liquids into Capillary Tubes. Philos. Mag. Ser. 6 1923, 45, 525–531.
32. Quéré, D. Inertial Capillarity. Europhys. Lett. 1997, 39, 533–538.
33. Berthier, J.; Brakke, K. A.; Gosselin, D.; Bourdat, A.-G.; Nonglaton, G.; Villard, N.; Laffite, G.; Boizot, F.; Costa, G.; Delapierre, G. Suspended Microflows between Vertical Parallel Walls. Microfluid. Nanofluidics 2015, 18, 919–929.
34. Li, C.; Boban, M.; Tuteja, A. Open-Channel, Water-in-Oil Emulsification in Paper-Based Microfluidic Devices. Lab Chip 2017, 17, 1436–1441.
35. Berthier, J.; Brakke, K. A. The Physics of Microdroplets; John Wiley & Sons, Inc.: Hoboken, NJ, USA, 2012.
36. Berthier, J.; Brakke, K. A.; Berthier, E. A General Condition for Spontaneous Capillary Flow in Uniform Cross-Section Microchannels. Microfluid. Nanofluidics 2014, 16, 779–785.
37. Berthier, J.; Gosselin, D.; Berthier, E. A Generalization of the Lucas–Washburn–Rideal Law to Composite Microchannels of Arbitrary Cross Section. Microfluid. Nanofluidics 2015, 19, 497–507.
38. Brakke, K. A. The Surface Evolver. Exp. Math. 1992, 1, 141–165.
39. Berthier, E.; Beebe, D. J. Flow Rate Analysis of a Surface Tension Driven Passive Micropump. Lab Chip 2007, 7, 1475–1478.
40. Walker, G. M.; Beebe, D. J. A Passive Pumping Method for Microfluidic Devices. Lab Chip 2002, 2, 131–134.
41. Freitas, A.; Quina, F.; Carroll, F. Estimation of Water-Organic Interfacial Tensions. A Linear Free Energy Relationship Analysis of Interfacial Adhesion. J. Phys. Chem. B 1997, 5647, 7488–7493.
42. Mohammad, A. A.; Alkhaldi, K. H. A. E.; AlTuwaim, M. S.; Al-Jimaz, A. S. Effect of Temperature and Chain Length on the Viscosity and Surface Tension of Binary Systems of N,N-Dimethylformamide with 1-Octanol, 1-Nonanol and 1-Decanol. J. Chem. Thermodyn. 2014, 74, 7–15.
43. Han, Y.; Shikazono, N. Measurement of the Liquid Film Thickness in Micro Tube Slug Flow. Int. J. Heat Fluid Flow 2009, 30, 842–853.
44. Mazutis, L.; Griffiths, A. D. Selective Droplet Coalescence Using Microfluidic Systems. Lab Chip 2012, 12, 1800–1806.
45. Chabert, M.; Dorfman, K. D.; Viovy, J.-L. Droplet Fusion by Alternating Current (AC) Field Electrocoalescence in Microchannels. Electrophoresis 2005, 26, 3706–3715.
46. Abate, A. R.; Hung, T.; Mary, P.; Agresti, J. J.; Weitz, D. A. High-Throughput Injection with Microfluidics Using Picoinjectors. Proc. Natl. Acad. Sci. U. S. A. 2010, 107, 19163–19166.

Chapter 3. DROPLET INCUBATION AND SPLITTING IN OPEN MICROFLUIDIC CHANNELS

Reproduced in part from Berry, S. B.; Lee, J. J.*; Berthier, J.; Berthier, E.; Theberge, A. B. Open Channel Droplet-Based Microfluidics. Anal. Methods 2019, 11, 4528-4536.*

**denotes co-authorship.*

3.1 ABSTRACT

Droplet-based microfluidics enables compartmentalization and controlled manipulation of small volumes. Open microfluidics provides increased accessibility, adaptability, and ease of manufacturing compared to closed microfluidic platforms. Here, we begin to build a toolbox for the emerging field of open channel droplet-based microfluidics, combining the ease of use associated with open microfluidic platforms with the benefits of compartmentalization afforded by droplet-based microfluidics. We develop fundamental microfluidic features to control droplets flowing in an immiscible carrier fluid within open microfluidic systems. Our systems use capillary flow to move droplets and carrier fluid through open channels and are easily fabricated through 3D printing, micromilling, or injection molding; further, droplet generation can be accomplished by simply pipetting an aqueous droplet into an empty open channel. We demonstrate on-chip incubation of multiple droplets within an open channel and subsequent transport (using an immiscible carrier phase) for downstream experimentation. We also present a method for tunable droplet splitting in open channels driven by capillary flow. Additional future applications of our toolbox for droplet manipulation in open channels include cell culture and analysis, on-chip microscale reactions, and reagent delivery.

3.2 INTRODUCTION

Open microfluidic systems offer many advantages for conducting life science experimentation including pipette accessibility, simple fabrication techniques with biocompatible materials, independence from pumps and external flow generators, and customizability.[1] Here, we describe a biphasic system driven by capillary forces that enables the control and manipulation of multiple droplets within an open channel devoid of any electrical or pneumatic actuation systems, in a fully open, pipette-accessible platform. We demonstrate a new open channel system for prolonged static droplet incubation in channel followed by capillary-driven translation of discrete droplets for downstream analysis, as well as tunable droplet splitting in open channels.

Droplet-based microfluidics advances the capabilities of traditional single-phase microfluidic platforms through compartmentalization of reaction components into discrete micro- to picoliter volumes, enabling decreased reagent consumption and use of valuable, low-volume samples that may otherwise be expensive or difficult to obtain.[2,3] Translation of assays to droplet-based platforms allows users to precisely form, manipulate, and transport small volumes for use in cell-based assays, chemical synthesis, and biochemical analyses.[2] Droplet-based systems for an extensive range of functions have been described[3], and droplet manipulation methods such as incubation[4,5], reagent addition[6], and splitting[7,8] have been developed. However, most current droplet-based microfluidic approaches rely on complex designs and multistep fabrication methods (e.g., photolithography, bonding) to create closed-channel platforms and often use external pumps and actuators to manipulate flow, allowing them to perform specialized functions but limiting their wide-spread adoption beyond engineering and physical science laboratories.[3] Recent work by Li et al.[9] overcomes some of the fabrication challenges of traditional droplet systems by using an open paper-based device, but the flow still requires external syringe pumps.

Systems utilizing open fluidic channels (e.g., channels devoid of a ceiling, devoid of a ceiling and floor, or devoid of lateral walls) and surface tension driven flow have emerged as alternatives to closed channel, pump-driven microfluidic platforms due to their relative ease of design, fabrication, and use.[1,10] Open channel platforms do not require bonding and can be fabricated in a single step using micromilling[11-13] or high-volume fabrication techniques such as injection molding.[14,15] Open platforms provide improved accessibility (e.g., pipette, automated reagent delivery systems) to users to manipulate experimental conditions through direct addition or removal of reagents at any point on the platform.[16] Additionally, open channel systems can be driven by capillary flow in a manner similar to that of closed capillary systems. Capillary flow removes the need for external flow drivers and improves the robustness and functionality of the platform, as the mechanism for flow is built into the device.[10] Recently, we presented an analytical model, numerical simulations, and experimental validation that described the behavioral modes of a single immiscible droplet placed in an open channel where a carrier flow occurs[17]; we found that an immiscible droplet can behave in a number of fundamentally different ways (remain static in the channel, translate at the leading edge of the carrier fluid, or detach from the walls of the channel and flow with the carrier fluid).

In our prior work[17], we also showed that multiple aqueous droplets can be created and transported by pipetting the aqueous phase into an oil carrier phase that is already flowing through the device based on capillary flow. In the present manuscript, we developed a new capability, which enables extended incubation of droplets within the channel in the absence of the carrier phase, followed by introduction of the carrier phase in the channel using spontaneous capillary flow, and subsequent movement of the droplets. In contrast to our prior work, the present manuscript enables longer residence times of the droplets within the channels since they can be

incubated for multiple hours before the carrier phase is added. Pipetting multiple aqueous droplets directly into an empty channel, incubating them, and *then* translating the train of droplets using a capillary-driven immiscible phase presents further challenges, as conditions such as surface wetting, evaporation, droplet merging, and satellite droplet formation all must be accounted for.

Here, we build a toolbox of droplet manipulation capabilities for open channel droplet-based microfluidics. We describe new open channel systems in which multiple discrete droplets can be placed into an open channel, incubated *in situ*, and then translated downstream either with droplet merging or without droplet merging, depending on the desired application. We also demonstrate an open microfluidic droplet splitting method to enable a parent droplet to be aliquoted into tailored smaller droplets (equal or unequal volumes) for multiplexed processing and readouts. Our open microfluidic systems rely on the surface interactions between the aqueous droplets, organic carrier phase, and channel surface which can be altered to fit various experimental needs; additionally, reliance on capillary-driven flow in an open channel removes the need for flow-generation devices and enables direct user access to the system at any time point. These platform functionalities (i.e., merging/splitting, incubation, user access) can help streamline large and cumbersome screening experiments that rely on manual pipetting, mixing, and splitting for sample generation, where manual processing can negatively contribute to assay time, sample loss, and costs associated with instrument usage. In future applications, these functionalities can be adapted and applied to array generation, sample preparation, and multiplexing.

3.3 Results and Discussion

References to ESI can be found in Appendix B

3.3.1 *Capillary-driven flow of droplets in an open channel*

While the dynamics and behavior of single phase capillary flow within an open system have been well characterized[18-21], the interaction and behavior of multiple phases within an open channel has been less extensively studied. Previously, in an open two-phase system driven by spontaneous capillary flow (SCF), we found that a single aqueous droplet within an open channel demonstrates different behavioral modes (e.g., translation, displacement, remaining stationary) largely governed by the interfacial tension between the droplet and the carrier phase, the contact angle of the droplet and carrier phase on the channel surface, and the velocity of the carrier phase.[17] In the present manuscript, we use two of these behavioral modes (Figure S1) to create open channel manipulation modules driven by capillary flow: "shift mode", in which an aqueous droplet wets all sides of the open channel and is translated downstream by the carrier phase (Figure S1i-ii), and "raft mode", in which an aqueous droplet completely detaches from the channel and is displaced downstream by the carrier phase (Figure S1iii-iv).[17] Shift mode occurs when an aqueous droplet in the channel precedes the advancing front of the carrier fluid, and the carrier fluid does not pass in front of the droplet; alternatively, raft mode occurs when the carrier fluid surrounds the droplet and simultaneously flows in front of and behind the droplet. Notably, in the case of both behavioral modes, the carrier fluid governs the overall dynamics of the system, as the pipetted droplets are entrained by the carrier fluid and transported downstream.

Within our open-channel platforms, we designed channel dimensions to fall within the flow regime governed by SCF[1,10] to ensure capillary-driven flow, and incorporated a rounded channel

geometry to negate flow along a wedge (i.e., Concus-Finn flow)[22](Figure 3.1). Further, we fabricated our platform with poly (methyl methacrylate) (PMMA) to provide the desired wettability between droplets, the carrier phase, and the channel surface; specifically, with contact angles of 78° between PMMA and the aqueous droplet, ≈ 12.5° between PMMA and the organic carrier phase, and 146.14° ± 0.9° between the PMMA and the aqueous droplet when submerged in the organic carrier phase (pentanol). Additionally, we did not use any surfactants in our platform. To prevent evaporation of droplets from within the channels during prolonged incubation times (i.e., hours), we enclosed our open channel platform within a humidified Omnitray™ (rectangular petri dish) surrounded by sacrificial water (1.5 mL in ≈ 50 µL droplets). Our open channel system offers advantages to closed systems as we can add droplets directly to the channel with a pipette and initiate flow of the carrier phase through simple pipetting into the inlet reservoir (Figure 3.1).

3.3.2 *Open channel droplet incubation and transport*

Inputting fluids into a typical microfluidic channel commonly requires dedicated ports and connectors. Addition of droplets into an open microfluidic channel, on the other hand, can be performed directly and at any location in the channel. Delivering small droplets (0.5-2.0 µL) with a pipette is a common approach available to most laboratories; alternatively, smaller droplets can be inputted through other approaches such as Acoustic Droplet Ejection methods.[23,24] While depositing droplets on a surface is straightforward, removal or transfer of small droplets from a surface at subsequent time points is challenging; for example, pipetting is unreliable and tedious, as part of the droplet often remains behind on the surface. Digital microfluidics, also referred to as Electrowetting on Dielectric (EWOD), provides a method to move small droplets, but requires the use of electrical components.[25-27] There is a need for simple systems in which droplets can be

pipetted onto an unmodified surface, incubated *in situ* for a desired period, and then passively manipulated or transferred.

Previously, we demonstrated addition of droplets to an organic carrier phase as the carrier fluid was flowing downstream, enabling droplet transport but limiting the incubation time of the pipetted droplets to the time required to reach the outlet.[17] Here, we present a different and adaptable platform where we pipette multiple discrete droplets into an open channel (in the absence of the organic carrier phase), incubate the droplets for a desired time, and then passively transport the droplets to a different location on chip *via* capillary-driven flow of an organic carrier phase (Figure 3.2). When multiple droplets are placed in series within an empty single open channel, translation of the droplets in shift mode leads to coalescence, as they merge with each subsequent droplet in the channel (Figure 3.2A). This functionality can be beneficial for analyses requiring pooling of multiple samples (e.g., discovery assays). For applications where droplet coalescence is not desired, we designed a separate flow path that we refer to as a 'bypass channel'. The bypass channel enables the immiscible carrier fluid to separate each discrete droplet (thereby preventing coalescence) and transport the droplets downstream via raft mode (Figure 3.2B-C). When the carrier phase reaches the bypass, which is positioned upstream of the droplet, part of the flow of the carrier fluid diverts through the bypass, while the remainder of the carrier phase continues in the main channel; the diverted flow fills the space between each droplet, while the nondiverted flow continues to drive the droplets through the main channel (Figure 3.2B-C). Initially, we observed droplet disruption (e.g., droplet breakup and/or flow through the bypass) and an increased flow rate through the bypass, which resulted in stagnation of the carrier phase flow in the bends of the main channel and prevented droplets from reaching the outlet (Figure 3.2B). To mitigate this droplet disruption, we designed the bypass channels with a step (Figure 3.2C-D) to increase the

hydrodynamic resistance (and therefore decrease the flux) through the bypass and maintain a sufficient flow rate in the main channel, ensuring that the droplets reached the outlet without breaking apart.

It is important to have a generalizable set of rules for designing bypass channels, to enable extension of our method to channels of different dimensions and geometries. We generated an analytical model that describes the ratio of fluid fluxes through the main channel relative to the bypass with respect to the fluidic resistance associated with each flow path. Deriving a model from a generalized Lucas-Washburn-Rideal law for open channels[18] (SI), we found the relationship between the fluidic resistances and flux to be:

$$\Delta P = P_1 - P_2 \approx \tilde{R}_1 Q_1 \approx \tilde{R}_2 Q_2 \quad (1)$$

where P is the pressure drop across our bypass system (P_1 and P_2 refer to the pressure drops at the nodes before and after the bypass, respectively), R_1 and R_2 are the resistances in the main channel and bypass channel, respectively, and Q_1 and Q_2 are the flux through the main channel and the bypass channel, respectively (SI). The fluidic resistance of the capillary-driven flow in our system can be described by Equation 2:

$$\mu \frac{p}{\lambda S^2} L = R \quad (2)$$

where S is the cross-sectional area, L is the channel length, μ is the liquid viscosity, p is the total perimeter, and λ is the friction length.[28] The resistance in our system inversely correlates to the cross-sectional area and the flux of fluid through the channel (SI). Solving for the ratio of the fluxes between the main channel and the bypass channel and then inserting the physical dimensions of

our system into Equation 2 (as detailed in the SI) yielded a flux ratio of $Q_2/Q_1 = 3.18$ wherein the flux through the bypass channel (Q_2) is greater than the flux through the main channel (Q_1). However, through incorporation of a step, we are able to increase the resistance through the bypass channel and ensure less diversion of flow from the main channel, altering the flux ratio to $Q_2/Q_1 = 2.68$. This relation demonstrates that the resistance through the bypass can be manipulated by altering the geometry of the step (i.e., larger step, increased resistance and decreased flux), enabling adaptation for different geometries and channel lengths. With different manufacturing techniques, even greater ratios can be designed. Further, while the flux is still greater in the bypass than the main channel, the decrease in the flux through the bypass afforded by the step enabled sufficient flow in the main channel to drive droplets towards the outlet and prevent stagnation of the carrier fluid in the channel curves (Figure 3.2C). The derived model provides a framework for adapting the bypass system with different geometries and acts as a useful tool for quantification of flow and hydrodynamic resistance in open channels, as well as for guiding optimization of droplet flow in open channel systems.

The ability to transport small volumes with SCF lays the foundation for future open-channel platforms that integrate processes such as cell culture or biochemical reactions with small-volume readouts such as mass spectrometry and immunoassays. Overall, the bypass system is designed to incubate and manipulate droplets without extensive user interaction or difficult pipetting steps. Ease of use is demonstrated through a simple two-step process (droplet addition followed by carrier fluid addition) without the need for adjusting flow rates and flow directions for droplet manipulation. Due to the fabrication and droplet addition methods used, this technique is currently limited to low-throughput applications and droplet volumes compatible with micropipettes (≥ 0.2 μL). Additionally, droplet number is determined by the device footprint and

friction forces between the carrier phase and the channel (resulting in decreased flow rate with an increased channel length) which restrict us from significantly extending the channel length; however, the bypass platform can be expanded to include more droplets through the creation of arrays of different geometries.

To demonstrate the expansion of this platform to incorporate more droplets, we fabricated an array of 8 devices with aligned inlet reservoirs, channels, and outlet reservoirs that enables sample loading, manipulation, and removal with a multichannel pipette. We present a potential workflow for this platform by conducting a model colorimetric assay[29] that consists of the combination of potassium thiocyanate (KSCN) and ferric nitrate ($Fe(NO_3)_3$) to form the colored complex $Fe(SCN^-)_x^{(3-x)+}$ (Figure 3.3). We pipetted 64 droplets (1 μL in volume) containing KSCN, $Fe(NO_3)_3$, or H_2O (negative control) into the channel and allowed the droplets to incubate for 30 min. at room temperature. Following incubation, we added a second 1 μL droplet containing KSCN, $Fe(NO_3)_3$, or H_2O to the first droplet and then initiated flow with undyed carrier fluid, coalescing the droplets within a single device and collecting them at each outlet reservoir. Once flow ceased, the droplets were removed using a multichannel pipette and transferred to a 96 well plate, where the absorbance of each combination was measured (Figure 3.3). Due to the formation of the $Fe(SCN^-)_x^{(3-x)+}$ complex and the movement of the droplet in shift mode, some droplet residue was observed in the channel after the addition of the carrier fluid. The ability to pipette droplets into a channel, incubate them for a desired period of time, and then supplement those droplets or manipulate them with flow through an open channel highlights the benefits of this open platform for assays where access to reagents or samples at specific time points with minimal user interaction is important. Further, compatibility of this platform with multichannel pipettes enables handling of larger volumes of liquid and simple integration with established laboratory materials (i.e., well

plates) and readouts (i.e., plate reader). Oftentimes, researchers want to be able to screen multiple conditions in an assay but then pool the samples together prior to analysis[30-32]; we envision that this platform can fulfill this need in a simple and easily implemented manner.

3.3.3 *Controlled and adjustable droplet splitting in open channels*

Building upon the droplet handling capabilities described for incubation and transport of multiple droplets, we demonstrate the ability to controllably split droplets within an open channel. Droplet splitting is an important feature that can extend the use of valuable or small volume samples by generating identical replicates and creating arrays for multiplexing. Using traditional droplet splitting geometries previously developed for closed-channel droplet-based microfluidics[7,8], we designed T junctions to split incoming droplets, where a droplet entering the junction fills each branch of the junction until it is slowed down by an expansion in the geometry of the channel (Figure 3.4A)[33,34]; once the junction is filled, the droplet splits relative to the length of each branch (Figure 3.4B). By tuning the lengths of the left and right branches of the T junction, we can generate symmetric or asymmetric droplets (Figure 3.4B-C), enabling users to generate variable volume aliquots from an original sample simply by changing the device dimensions. Further, the splitting of symmetric and asymmetric droplets was reproducible between devices within an array (Figure 3.4D). Some variability was observed between multiple arrays due to manual micromilling artifacts, but inter-array variability can be alleviated through fabrication with more consistent methods such as injection molding and advanced automated milling.[11,14] Currently, the platform is capable of splitting a single droplet in shift mode; devices can also be reused following washing and drying with reproducible results (Figure S5).

To demonstrate the workflow for a potential application of the open channel droplet splitting platform, we present a model experimental system for on-chip reagent delivery and reactions. We pipetted aqueous droplets tinted with yellow dye (to model primary reagents) upstream of a T junction and aqueous droplets tinted with green dye (to model secondary reagents) downstream of the T junction. We then loaded the inlet reservoir with carrier fluid to initiate flow. The carrier fluid flow drove the yellow droplet through the T junction, wherein the droplet split and its components were delivered to multiple samples (green droplets) downstream of the junction (Figure 3.5). The ability to preload the platform with reaction reagents allows users to generate multiplexed arrays for subsequent passive reagent delivery with minimal user handling; additionally, altering the channel distance and geometry after mixing can be used to adjust the incubation time of the reaction.[8]

3.4 Materials and Methods

3.4.1 *Materials.*

Droplets were created with deionized (DI) water (Type II, Harleco; Fisher Scientific, Hampton, NH) tinted with either yellow or green dye (Spice Supreme; Gel Spice Company, Bayonne, NJ) at a concentration of 10% or 1% (v/v), respectively. The carrier fluids were: toluene (Fisher Scientific, Figure 3.1) or 1-pentanol (Acros Organics, Thermo Fisher Scientific, Waltham, MA, Figures 3.1, 3.2, 3.3, 3.4, and 3.5). All carrier fluids solvents were tinted with Solvent Green 3 (Sigma-Aldrich, St. Louis, MO) at a concentration of 0.50 mg/mL.

3.4.2 *Device fabrication*

Devices were designed with Solidworks 2017 (Solidworks, Waltham, MA) and converted to .TAP files with SprutCam 10 (SprutCam, Naberezhnye Chelny, Russia). The devices were milled on poly(methyl methacrylate) (PMMA) sheets of 3.175 mm thickness (McMaster-Carr, Santa Fe Springs, CA) using a Tormach PCNC 770 mill (Tormach, Waunakee, WI). All device channels were milled with ball endmills (Performance Micro Tool, Janesville, WI) with a cutter diameter of 1/32" (TR-2-0313-BN) or 1/64" (TR-2-0150-BN) to create round-bottom channels. After milling, the devices were rinsed with DI water, sonicated in 70% (v/v) ethanol, and rinsed again with DI water. The devices were then dried with compressed air prior to use.

3.4.3 *Device design and testing*

The main device dimensions are a channel width of 0.90 mm and a channel depth of 1.0 mm, with smaller channels included for carrier fluid bypass (0.5 mm wide, 1.0 mm length, 0.2 mm step height) (Figure 3.2D) and splitting (1.0 mm branch length, 0.45 mm channel width); the detailed dimensions of the devices and features are included in the SI (Figure S2). Computer aided design (CAD) files (.STEP) are also included in the SI. Aqueous droplets with a volume of 1.0 μL (Figures 3.1 and 3.2) or 3.0 μL (Figures 3.3 and 3.4) were generated in the channel with a pipette. Carrier fluids with a volume of 240 μL were dispensed in the inlet reservoir of the channel. Droplets were imaged and analyzed with ImageJ (National Institutes of Health, MD) for quantification (Figure 3.3 and S3). To prevent evaporation, devices were placed inside of a humidified Nunc™ Omnitray™ (Thermo Fisher, Frederick, MD) surrounded by 1.5 mL of sacrificial water droplets (≈ 50 μL/droplet), and the Omnitray was then placed inside a secondary

humidified bioassay dish (#240835, Thermo Fisher) containing 100 mL of sacrificial water for extended incubations.

For the arrayed colorimetric analysis system, 1 μL droplets containing 0.1 N potassium thiocyanate (KSCN) (Fisher Scientific), 0.067 M ferric nitrate ($Fe(NO_3)_3$) (Fisher Scientific), or DI water were added to the open channel device (Figure 3.3) and allowed to incubate at room temperature for 30 minutes. Following incubation, a second 1 μL droplet containing KSCN, $Fe(NO_3)_3$, or H_2O was added directly to the incubating droplet for a final volume of 2 μL. 150 μL of undyed 1-pentanol was then added to the inlet reservoir to initiate flow. Once the coalesced droplets reached the outlet reservoir, they were removed using a multichannel pipette (16 μL) and added to a 96 well plate; each sample was diluted with DI water up to 50 μL to ensure accurate absorbance measurements. The absorbance of the plate was then measured at 450 nm using a Multiskan Spectrum UV/visible Microplate Reader (Thermo Labsystems, Waltham, MA). The experiment was repeated three times using three independent arrays of devices; each array contained two replicate devices per condition. Plotted points represent the average of the two replicate devices. All images were analyzed using ImageJ and visualized using Prism (GraphPad Software, San Diego, CA).

3.4.4 *Imaging*

Images and videos were acquired using a MU1403B High Speed Microscope Camera mounted on an Amscope SM-3TZ-80S stereoscope (Amscope, Irvine, CA) unless otherwise noted. For Figure 3.1B, 3.4C and 3.5, images and videos were obtained with a Nikon-D5300 ultra-high resolution SLR camera (Tokyo, Japan).

3.5 CONCLUSION

In this work, we develop essential features for immiscible droplet manipulation in capillary-driven open systems. Open channels offer several advantages over closed channels including pipette accessibility, manufacturability, customizability, and ease of use. Using these features, we created a generalized open channel platform for addition, incubation, and translation of multiple droplets and an open channel platform for droplet splitting and delivery. These platforms build upon prior work describing the fundamental behavior of single droplets in open biphasic systems by providing previously unavailable user functionalities (e.g., incubation of multiple droplets within a channel, droplet splitting) and creating foundational systems that can be customized and adapted for a range of experimental needs. Traditional closed-channel droplet microfluidics provides high throughput capabilities that can accommodate $>10^7$ samples with droplet volumes reaching 10^{-15} L and can integrate with large-capacity screening instrumentation (LC/MS, high speed microscopy, etc.), greatly increasing the abilities of researchers to perform high throughput experimentation.[3] Open-channel droplet microfluidics aims to address a different scale and set of experimental applications for researchers performing smaller screening studies (tens or hundreds of samples) with higher volumes (μL-nL) that do not require the extensive infrastructure nor cost associated with high throughput droplet microfluidics; further, we anticipate that our platform offers increased user accessibility, tractability, streamlining, and ease of use that allows for easy integration with existing experimental protocols and sample generation tools (e.g., pipettes, liquid handling robot). Future work with these platforms will include increasing the capacity of the bypass system for larger droplet arrays, expanding the droplet splitting capabilities to accommodate a wider range of splitting ratios, and studying the dynamics of mixing in open channels. Further, in future investigations our platforms could be extended to smaller scales with

the use of high resolution fabrication techniques and lower-volume liquid handlers or dispensers. In the future, we envision adaptation of these foundational platforms will enable users to expand and customize their current experimental toolbox for studies relating to drug screening, microscale reactions, and the "-omics" fields (e.g., metabolomics, proteomics).

3.6 FIGURES

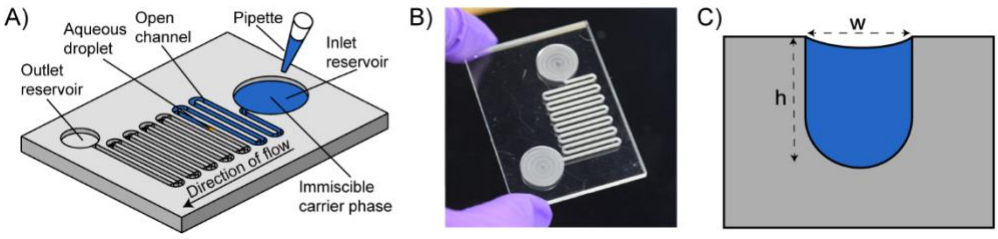

Figure 3.1. General platform design and modes of operation for translating aqueous droplets via capillary flow of an organic carrier phase. A) Schematic representation of open channel platform illustrating addition of organic carrier fluid (blue) with aqueous droplets (yellow) present in the channel; B) image of open channel platform; C) cross sectional schematic of channel (w = 0.90 mm and h = 1.0 mm).

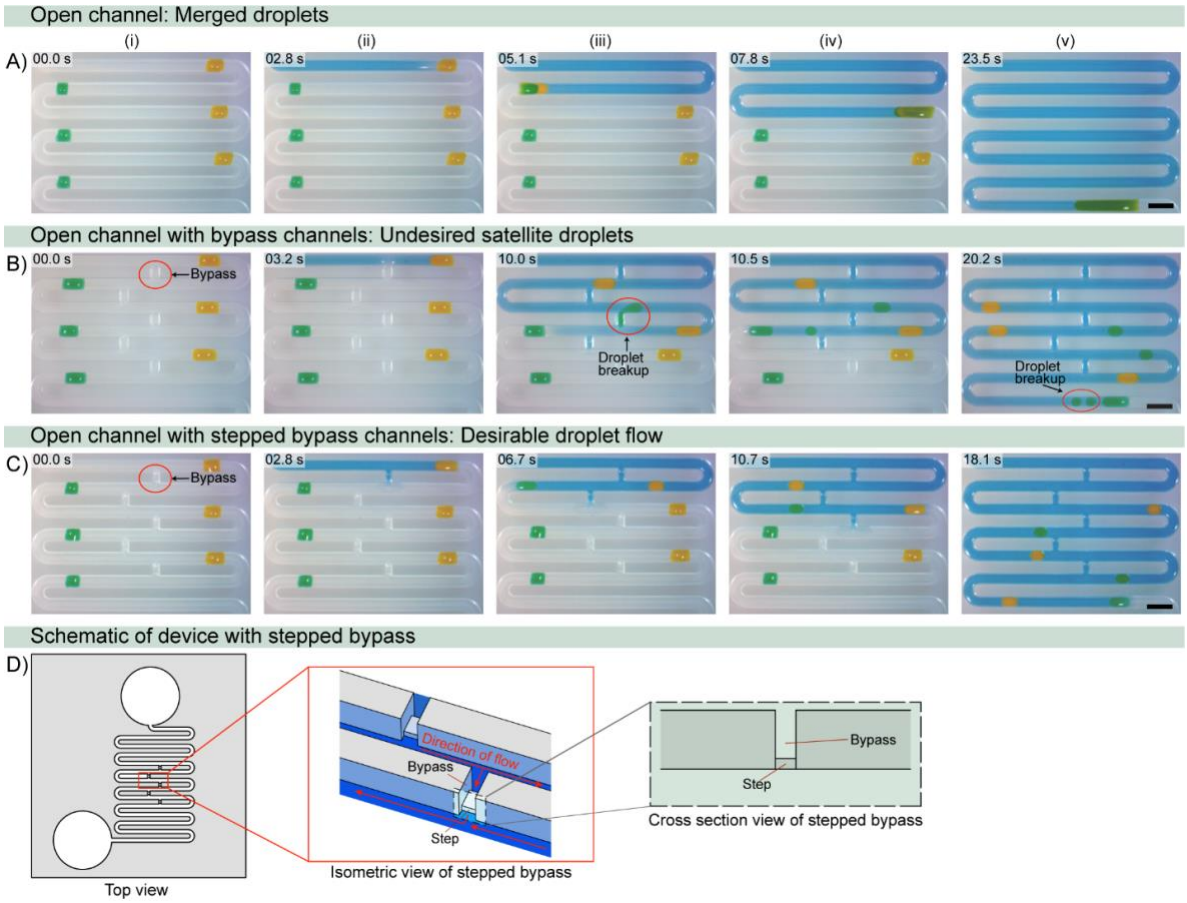

Figure 3.2. Open channel droplet incubation and transport.
Droplets (alternating yellow and green for visualization) are incubated in an open channel without (A) or with (B-C) bypass channels (red circles); i-v) carrier fluid (blue) is pipetted in the inlet and flows down the channel via capillary flow, translating the droplets down the channel to the outlet reservoir. Bypass channels (B-C) prevent coalescence of preincubated droplets by inserting immiscible carrier fluid between aqueous droplets as they flow downstream. C) Incorporation of stepped bypass improves flow in the main channel and prevents formation of satellite droplets and droplet stagnation. D) Schematic of stepped bypass showing an isometric and cross-sectional view of the step in the bypass. Scale bar: 2 mm. Timestamps correspond to the addition of the carrier fluid (0.0 s) and not total droplet incubation time.

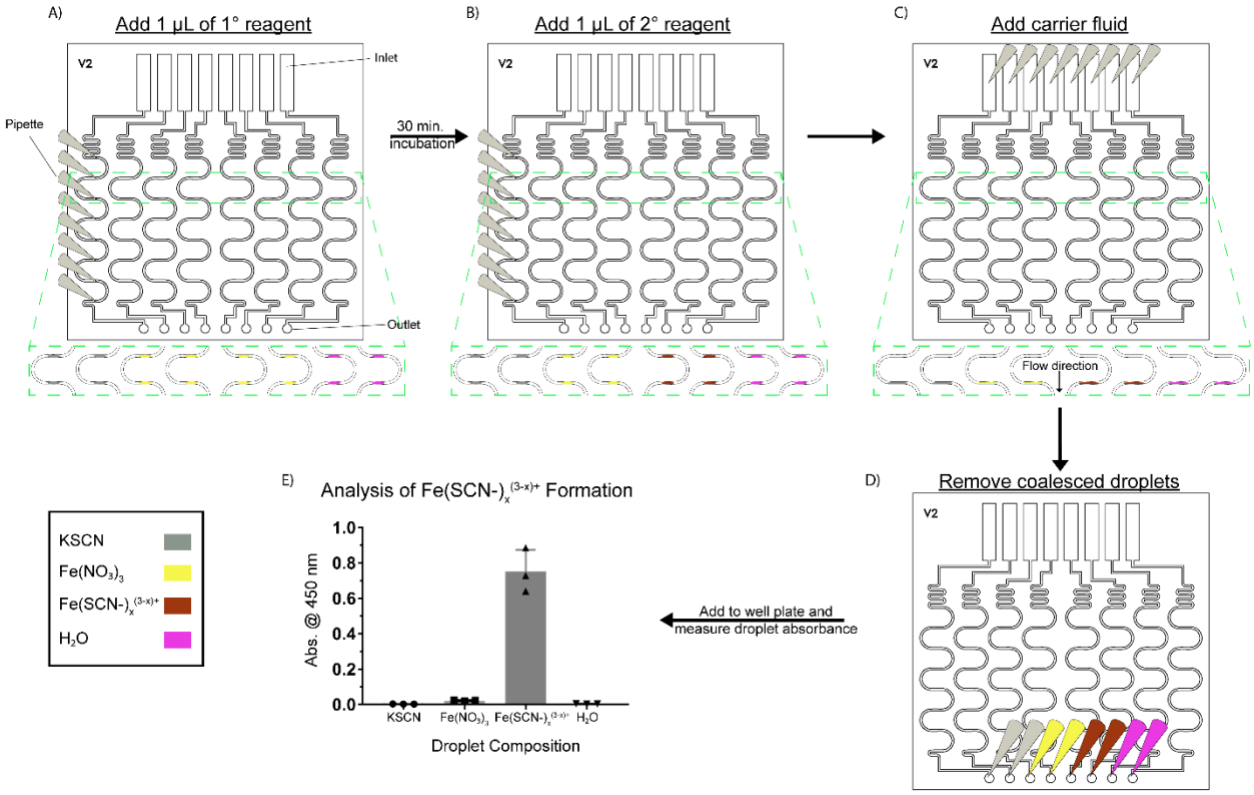

Figure 3.3. Workflow schematic and results for model colorimetric assay. A) Using a multichannel pipette, eight 1 µL droplets of KSCN (first and second channel), $Fe(NO_3)_3$ (third through sixth channel) or H_2O (seventh and eighth channel) are added to their respective open channel in each device of the array and allowed to incubate for 30 minutes at room temperature. B) After incubation, 1 µL droplets of KSCN, $Fe(NO_3)_3$, or H_2O are added to the incubating droplets with the following combinations: KSCN + KSCN, $Fe(NO_3)_3$ + $Fe(NO_3)_3$, KSCN + $Fe(NO_3)_3$, and H_2O + H_2O (negative control). C) Colorless carrier fluid was then added to the inlet to coalesce and flow all the droplets to the outlet. D) Droplets are removed from the outlet reservoir using a multichannel pipette and transferred to a 96 well plate. E) The absorbance of the droplets is measured at 450 nm and a color change is observed in the droplet containing KSCN + $Fe(NO_3)_3$, indicating the presence of the colored compound $Fe(SCN^-)_x^{(3-x)+}$.

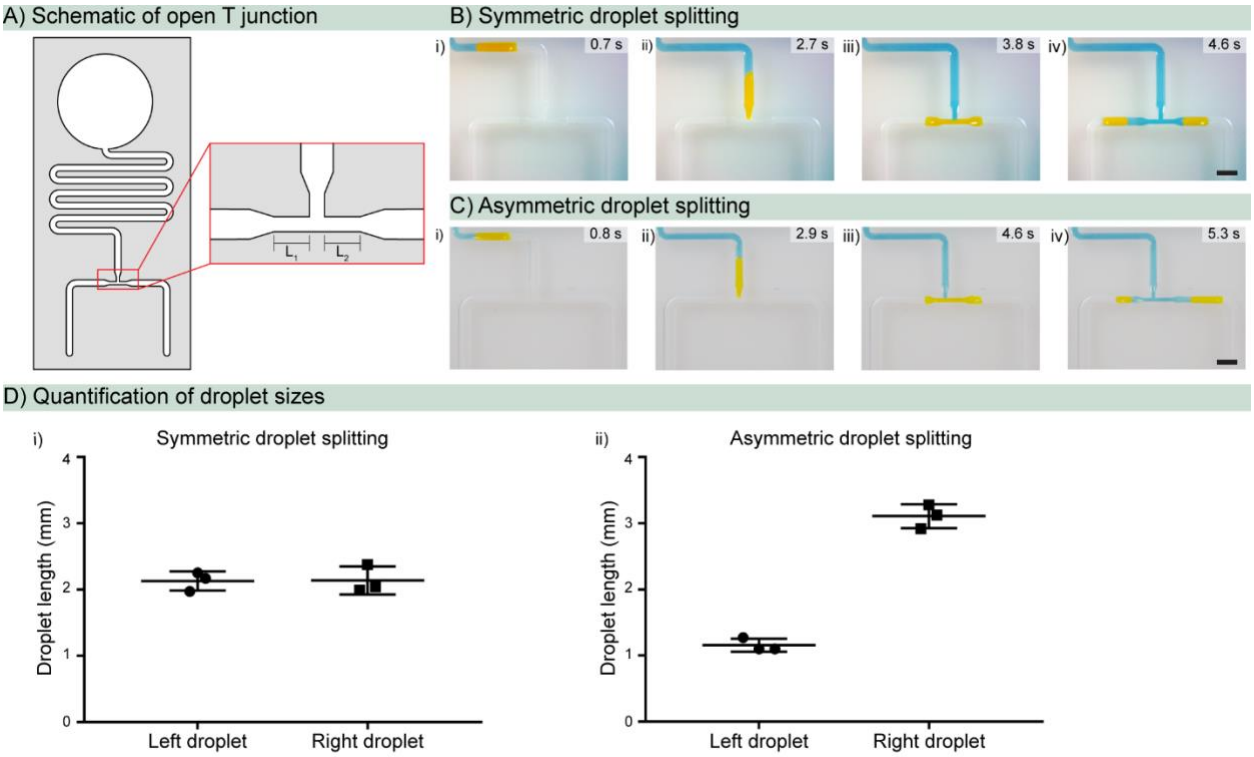

Figure 3.4. Controlled and adjustable droplet splitting in open channels with SCF. A) Schematic of T junction showing branches (L_1 and L_2) within the junction; B-C) i-ii) a droplet in the channel above a T junction with symmetric (B) or asymmetric (C) branch lengths is translated toward the junction via SCF; iii) the droplet fills both branches in the junction and slows upon reaching the channel expansion after the junction due to temporary pinning; iv) the droplet splits into two discrete droplets dependent upon the branch length; D) quantification of daughter droplet sizes after splitting in T junctions with symmetric (i) or asymmetric (ii) branch ratios (data points represent a single droplet split in three different devices within an array of devices, mean and standard deviation are indicated). Scale bar: 2 mm.

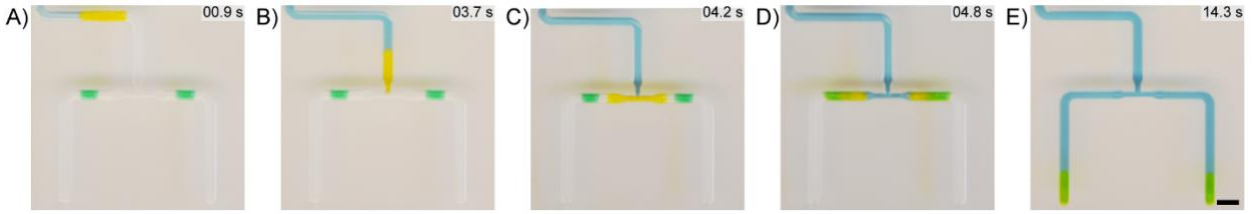

Figure 3.5. Workflow for droplet splitting and merging with downstream droplets to model reagent delivery. A yellow droplet (representing a primary reagent) was pipetted above the T junction while green droplets (representing secondary reagents) were added after the junction. A-B) Carrier fluid translates the yellow droplet via SCF into the junction; C) the droplet splits equally and is delivered (D) to the secondary reagents in the channel; E) the droplet and reagent mix as the droplet flows down the channel. Scale bar: 2 mm.

3.7 REFERENCES

1. Berthier, J.; Brakke, K.A.; Berthier, E. Open Microfluidics. Wiley, 2016.
2. Teh, S.Y.;Lin, R.; Hung, L.H.; Lee, A.P. Droplet microfluidics. Lab Chip, 2008, 8, 198-220.
3. Shang, L.; Cheng, Y.; Zhao, Y. Emerging Droplet Microfluidics. Chem. Rev., 2017, 117, 7964-8040.
4. Frenz, L.; Blank, K.; Brouzes, E.; Griffiths, A.D. Reliable microfluidic on-chip incubation of droplets in delay-lines. Lab Chip, 2009, 9, 10, 1344-1348.
5. Boukellal, H.;Selimovic, S.; Jia, Y.; Cristobal, G.; Fraden, S. Simple, robust storage of drops and fluids in a microfluidic device. Lab Chip, 2009, 9, 331-338.
6. Abate, A.R.; Hung, T.; Mary, P.; Agresti, J.J.; Weitz, D.A. High-throughput injection with microfluidics using picoinjectors. PNAS, 2010, 107, 45, 19163-19166.
7. Link, D.R.; Anna, S.L.; Weitz, D.A; Stone, H.A. Geometrically mediated breakup of drops in microfluidic device. Phys. Rev. Lett., 2004, 92, 054503.
8. Song, H.; Chen, D.L.; Ismagilov, R.F. Reactions in droplets in microfluidic channels. Angew. Chem. Int. Ed. Engl., 2006, 45, 44, 7336-7356.
9. Li, C.; Boban, M.; Tuteja, A. Open-channel, water-in-oil emulsification in paper-based microfluidic devices. Lab Chip, 2017, 1436.
10. Casavant, B.P.; Berthier, E.; Theberge, A.B.; Berthier, J.; Montanez-Sauri, S.I.; Bischel, L.L.; et al. Suspended Microfluidics. PNAS, 2016, 110, 10111–10116.
11. Guckenberger, D.J.; de Groot, T.E.; Wan, A.M.D.; Beebe, D.J.; Young, E.W.K. Micromilling: A method for ultra-rapid prototyping of plastic microfluidic devices. Lab Chip, 2015, 15, 11, 2364-2378.
12. de Groot, T.E.; Veserat, K.S.; Berthier, E.; Beebe, D.J.; Theberge, A.B. Surface-tension drive open microfluidic platform for hanging droplet culture. Lab Chip, 2016, 16, 334.
13. Barkal, L.J.; Theberge, A.B.; Guo, C.J.; Spraker, J.; Rappert, L.; Berthier, J.; et al. Microbial metabolomics in open microscale platforms. Nature Communications, 2016, 7, 10610.
14. Lee, U.N.; Su, X.; Guckenberger, D.J., Dostie, A.M.; Zhang, T.; Berthier, E.; et al. Fundamentals of rapid injection molding for microfluidic cell-based assays. Lab Chip, 2018, 18, 496-504.
15. Lee, Y.; Choi, J.W.; Yu, J.; Park, D.; Ha, J.; Son, K.; et al. Microfluidics within a well: an injection-molded plastic array 3D culture platform. Lab Chip, 2018, Advance Article.
16. Huemmer, D.; Bachler, S.; Kohler, M.; Blank, L.M.; Zenobi, R.; Dittrich, P.S.; Microfluidic platform for multimodal analysis of enzyme secretion in nanoliter droplet arrays. Anal. Chem., 2018, xxxxx
17. Lee, J.J.; Berthier, J.; Brakke, K.A.; Dostie, A.M.; Theberge, A.B.; Berthier, E. Droplet behavior in Open Biphasic Microfluidics. Langmuir, 2018, 34, 18, 5358-5366.
18. Berthier, J.; Gosselin, D.; Berthier, E. A generalization of the Lucas-Washburn-Rideal law to composite microchannels of arbitrary cross section. Microfluid. Nanofluid., 2015, 19, 3, 497-507.

19. Chen, Y.F.; Tseng, F.G.; Chein, S.Y.C.; Chen, M.H.; Yu, R.J.; Chieng, C.C. Surface tension driven flow for open microchannels with different turning angles. Microfluid Nanofluid, 2008, 5, 193-203.
20. Lade Jr., R.K.; Jochem, K.S.; Macosko, C.W.; Francis, L.F. Capillary Coatings: Flow and Drying Dynamics in Open Microchannels. Langmuir, 2018, 34, 7624-7639.
21. Yang, D.; Krasowska, M.; Priest, C.; Popescu, M.N.; Ralston, J. Dynamics of capillary-driven flow in open microchannels. J. Phys. Chem. C., 2011, 115, 18761-18769.
22. Concus, P.; Finn, R. On the behavior of a capillary surface in a wedge. PNAS, 1969, 2, 63, 292–299.
23. Hadimioglu, B.; Stearns, R.; Ellson, R. Moving Liquids with Sound: The Physics of Acoustic Droplet Ejection for Robust Laboratory Automation in Life Sciences. Journal of Laboratory Automation, 2016, 21, 1, 4-18.
24. Demirci, U. Acoustic Picoliter Droplets for Emerging Applications in Semiconductor Industry and Biotechnology. Journal of Microelectromechanical Systems, 2006, 15, 4, 957-966.
25. Choi, K.; Ng, A.H.C.; Fobel, R.; Wheeler, A.R. Digital Microfluidics. Annu. Rev. Anal. Chem., 2012, 5, 413-440.
26. Ng, A.H.C.; Li, B.B.; Chamberlain, M.D.; Wheeler, A.R. Digital Microfluidic Cell Culture. Annu. Rev. Biomed. Eng., 2015, 17, 91-112.
27. Jones, T.B. On the relationship of dielectrophoresis and electrowetting. Langmuir, 2002, 18, 11, 4437-4443.
28. Lee, J.J.; Karampelas, I.H.; Brakke, K.A.; Theberge, A.B.; Berthier, E.; Berthier, J. Capillary flow of solvents and aqueous liquids in rounded open microgrooves. Langmuir.Accepted..
29. Fidalgo, L.M.; Abell, C.; Huck, W.T.S. Surface-induced droplet fusión in microfluidic devices. Lab Chip, 2007, 7, 984-986.
30. Yang, Y.H.; Song, E.; Lee, B.R.; Kim, E.J.; Park, S.H.; Kim, Y.G.; et al. Rapid functional screening of Streptomyces coelicolor regulators by use of a pH indicator and application to the MarR-like regulator AbsC. Appl. Environ. Microbiol., 2010, 76, 11, 3645-3656.
31. Onaka, H.; Mori, Y.; Igarashi, Y.; Furumai, T. Mycolic acid-containing bacteria induce natural-product biosynthesis in Streptomyces species. Appl. Environ. Microbiol., 2011, 77, 2 400-406.
32. Adnani, N.; Vazquez-Rivera, E.; Adibhatla, S.N.; Ellis, G.A.; Braun, D.R.; Bugni, T.S. Investigation of interspecies interactions with marine micromonosporaceae using an improved co-culture approach. Mar. Drugs, 2015, 13, 6082-6098.
33. Mehrabian, H.; Gao, P.; J.J. Feng, J.J. Wicking flow through microchannels. Physics of Fluids, 2011, 23, 122108.
34. Berthier, J; Brakke, K.A.; Gosselin, D.; Navarro, F.; Belgacem, N.; Chaussy, D.; Berthier, E. On the halt of spontaneous capillary flows in diverging open channels. Med. Eng. Phys. 2017, 75-80.

Chapter 4. CAPILLARY FLOW IN OPEN MICROGROOVES: BIFURCATIONS AND NETWORKS

Reproduced in part from Lee, J. J.; Berthier, J.*; Theberge, A. B.; Berthier, E. Capillary Flow in Open Microgrooves: Bifurcations and Networks. Langmuir 2019, 35 (32), 10667–10675.*

**denotes co-authorship. J.J.L contributed to the overall fabrication designs and experimental designs. J.B. developed the analytical model and numerical simulation of this work.*

4.1 ABSTRACT

Open capillary flows are increasingly used in biotechnology, biology, thermics, and space science. So far, the dynamics of capillary flows has been studied mostly for confined channels. However, the theory of open microfluidics has considerably progressed during the last years, and an expression for the travel distance has been derived, generalizing the well-known theory of Lucas, Washburn, and Rideal. This generalization is based on the use of the average friction length and generalized Cassie angle. In this work, we successively study the spontaneous capillary flow in uniform cross-section open rounded U-grooves—for which methods to determine the friction lengths are proposed—the flow behavior at a bifurcation, and finally in a simple-loop network. We show that after a bifurcation, the Lucas-Washburn-Rideal law needs to be adapted and the relation between the travel distance and time is more complicated than the square root of time dependency.

4.2 INTRODUCTION

The science of capillary flows or "capillarics" has seen considerable development recently[1,2]. This field of science intervenes in different domains such as biology, biotechnology, materials, thermics, and space science. While capillarity in closed, cylindrical tubes is well-known from the first studies of Lucas[3], Wasburn[4], Rideal[5], and Bosanquet[6], fundamentals of capillarity in channels of arbitrary cross sections—including open channels—are more recent. In closed, homogeneous channels, spontaneous capillary flow (SCF) occurs when the liquid-wall contact angle is less than 90°. Concerning the dynamics of the flow in cylindrical channels, the Lucas-Washburn-Rideal (LWR) law governs the travel distance and velocity of the flow (except for the area close to the entry of the channel where inertial effects are not negligible)[7].

Investigation of open capillary flow is more recent. Mann, Rye, Yost, and Romero demonstrated that the open capillary flow of solder in V-grooves, followed the predictions of the LWR law where the square root of time is dependent on the travel distance[8–10]. Sharp V-grooves have been shown to accommodate fast capillary flows[11].

More recently, the behavior of capillary flow in rectangular open channels has been investigated[12–14]. Finally, suspended capillary flows—i.e., open capillary flows in channels devoid of bottom and ceiling—have been recently documented[15,16]. All these studies have confirmed that the square root time dependency of the travel distance is respected—with the exception of the short initial phase where inertia plays a role[7,17]—and the coefficient in front of the temporal term depends on the geometry and liquid properties [18,19].

Additionally, the behavior of capillary flow in open channels of non-uniform cross-sections has been recently investigated[18,20]. But bifurcations, bypasses and networks are still largely

unexplored, except for the numerical work of Mehrabian et al. for closed channels[21] and the experimental investigations by Berry et al.[22,23].

In this work, we first analyzed the behavior of an open capillary flow in an open rounded U-groove, then the flow separation at a bifurcation, and finally the flow repartition in bypasses and networks were determined. We show that the square root time dependency of the travel distance does not apply after a bifurcation, confirming the numerical approach of Mehrabian and coworkers[21]. We demonstrated that the travel distances after a bifurcation are solutions of coupled quadratic equations. The approach constitutes a first step in the understanding of open channel capillary pumping.

4.3 Results and Discussion

References to Supporting Information can be found in Appendix C

4.3.1 *Analysis of the SCF in the uniform cross-section channel.*

It has been established that the dynamics of the capillary flow in an open channel is determined by two parameters: the generalized Cassie angle and the average friction length[31]. The generalized Cassie angle, θ^* is defined by

$$cos\theta^* = \frac{-p_F + \sum_{i=1,n} p_{w,i} cos\theta_i}{p}, \qquad (1)$$

where p_F and $p_{w,i}$ are, respectively, the free perimeter (in contact with air) and wetted perimeters (in contact with the liquid) in a cross section of the open channel. In the present case of a U-shaped channel with a semi-circular section in the bottom part (see Figure 4.2), we can write, $p_F = w$ and $p_w = 2h + \pi\frac{w}{2}$. Then relation (1) yields equation 2.

$$cos\theta^* = cos\theta - \frac{2}{1+\pi/2+2h/w} \quad (2)$$

The values of the Cassie angles are listed in Table 4.2. The presence of the air boundary considerably increases the average (Cassie) contact angle. The second parameter of the equation is the average friction length $\bar{\lambda}$[18,31]. Let us recall that the average friction length is defined as the average friction $\bar{\tau}$

$$\bar{\tau} = \frac{1}{p}\int_\Gamma \tau \, dl = \frac{1}{p}\int_\Gamma \mu \frac{V}{\lambda} \, dl = \mu \frac{V}{\bar{\lambda}}, \quad (3)$$

where τ is the local friction, λ the local friction length, $\tau = \mu \frac{V}{\lambda}$, μ is the liquid viscosity, and V the average velocity. The determination of the average friction length is not straightforward. A closed form expression for the average friction length does not exist for complicated geometries. A numerical approach can be utilized to find this parameter. Here we have used the finite element software COMSOL. The geometry considered in the computation is that of the rounded groove, with a friction condition on the bottom and side walls and a symmetry condition on the top surface mimicking the free surface condition (Figure 4.3). This condition introduces an approximation since the real open surface is not flat but slightly bent inwards; the symmetry condition is however justified by the zero shear rate at the free surface, as shown by Brackbill and coworkers.[32]This no-shear condition at the free surface is also used by Kolliopoulos and coworkers[33] for the determination of the flow in open rectangular microchannels. An arbitrary average velocity is imposed in the inlet cross section while a zero-pressure condition is set up in the outlet cross section. The shear rate at the wall is deduced from the derivative of the calculated velocities in a

cross section, at the nodes of the geometrical meshes close to the solid wall. The shear rate is then averaged along the perimeter of the cross section in order to obtain the averaged shear rate $\frac{V}{\bar{\lambda}}$.

In the case of the channel depicted in Figure 4.2, the calculated value for the average wall shear rate is $\dot{\gamma} \approx 5.2\ s^{-1}$ for an average velocity of the carrier liquid of $V = 1$ mm/s. Using (3), we find $\bar{\lambda} \sim 192$ µm (see SI Section 2 for the derivation of the friction length). Note that the viscosity does not affect the value of the friction length, which is only geometrical and linked to the velocity profile in a cross section. The value $\bar{\lambda} \sim 192$ µm is consistent with the values found using approximations for simple geometries of similar dimensions. First, consider a suspended channel of width $w = 0.8$ mm. An approximation of the average friction length is $\bar{\lambda} \sim \frac{w}{6}\frac{w+6}{h} = 229$ µm. Second, a rectangular U-groove of depth $h = 1.1$ mm would have an average friction length $\bar{\lambda} \sim \frac{1}{6}\frac{2w+h}{\frac{w}{h}+\frac{2h}{w}} = 182$ µm. Finally, a rectangular U-groove of depth $h = 1.1 + 0.4 = 1.5$ mm would have an average friction length $\bar{\lambda} \sim \frac{1}{3}\frac{w+h}{\frac{w}{h}+\frac{2h}{w}} = 179$ µm.

Finally, the following analysis of the experimental results for the travel distance vs. time indicates that the value $\bar{\lambda} \sim 200$ µm is a good approximation of the average friction length. Using the definitions of the generalized Cassie angle and the average friction length, the travel distance for an open capillary flow as a function of the time is given by the general expression[18].

$$z = \sqrt{\frac{\gamma}{\mu}\, 2\, \bar{\lambda}\, cos\theta^*}\, \sqrt{t}\,, \qquad (4)$$

where z is the travel distance, t the time, μ the viscosity, and γ the surface tension. Time derivation of (4) yields the capillary velocity

$$V = \sqrt{\frac{\gamma}{\mu}\ \frac{\bar{\lambda}}{2} cos\theta^*}\ \frac{1}{\sqrt{t}} \quad (5)$$

Finally, eliminating the time between (4) and (5) yields the relation between the velocity and travel distance

$$V = \frac{\gamma}{\mu}\ \bar{\lambda}\ cos\theta^*\ \frac{1}{z}\ . \quad (6)$$

The travel distance is measured by following the location of the front end of the capillary flow which is colored by a blue dye (Figure 4.4).

In Figure 4.5, the measured travel distance vs. time is plotted for the six different liquids and compared to the theoretical results (eq. 4) using the value $\bar{\lambda}$ = 195 μm and the physical properties of the liquids at a temperature of 20°C (Table 4.1). The data follow a linear trend. The slopes were calculated using a least squares approach ($R^2 > 0.99$), and the comparison between the experimental determinations of the slopes (time coefficient) and theoretical results is shown in Table 4.3.

Theoretical versus experimental data of Table 4.3 are plotted in Figure 4.6. They align well along the diagonal (y = x), indicating close correspondence between theoretical and experimental data across all solvents.

4.3.2 *Bifurcations.*

We then investigated the behavior of the capillary flow at a bifurcation (Figure 4.7). As Mehrabian and coworkers[21] pointed out, the flows in the two daughter branches are coupled via the pressure at the fork.

Using the notations of Figure 4.7, where the index *j* stands for the "junction", the pressure at the junction is given by the pressure drop due to friction between reservoir ($P = 0$) and junction (P_j)

$$-P_j = z_0\, p_0\, \frac{\bar{\tau}_0}{S_0} \triangleq\ z_0\, p_0\, \mu \frac{V_0}{\bar{\lambda}_0} \frac{1}{S_0}, \tag{7}$$

where S_0 is the cross-sectional area, $\bar{\tau_0}$ the average wall friction, and p_0 the total channel perimeter $p_0 = p_{w0} + p_{F0}$, μ the viscosity of the liquid and $\bar{\lambda}_0$ the average friction length in the root channel. Note that, by convention, we have subtracted the atmospheric pressure to all pressures in the channels. We can write the pressure drop in each daughter channel which includes the friction and capillary forces

$$-P_j = -z_1\, p_1\, \mu \frac{V_1}{\bar{\lambda}_1} \frac{1}{S_1} + \frac{\gamma\,(p_{w1} \cos\theta - p_{F1})}{S_1} = -z_1\, p_1\, \mu \frac{V_1}{\bar{\lambda}_1} \frac{1}{S_1} + \frac{\gamma\, p_1 \cos\theta_1^*}{S_1}, \tag{8}$$

where p_1 is the total perimeter in branch 1: $p_1 = p_{W1} + p_{F1}$, and

$$-P_j = -z_2\, p_2\, \mu \frac{V_2}{\bar{\lambda}_2} \frac{1}{S_2} + \frac{\gamma\, p_2 \cos\theta_2^*}{S_2}, \tag{9}$$

for branch 2. The contact angle θ is the same everywhere, but the generalized Cassie angle θ^* is not the same if the shape of each daughter channel is different after the bifurcation. In addition, the mass conservation imposes

$$S_0\, V_0 = S_1\, V_1 + S_2\, V_2\,. \tag{10}$$

Using (10), relation (7) can be rewritten

$$-P_j = z_0\, p_0\, \mu \frac{1}{\bar{\lambda}_0 S_0{}^2}\,(S_1 V_1 + S_2 V_2). \tag{11}$$

Taking in consideration that $V_i = dz_i/dt$ for each branch the system of equations (8), (9), and (11) is a system with three unknowns $\{P_j, z_1, z_2\}$. We first eliminate P_j. Subtracting (8) from (9)

$$\frac{1}{2} p_1\, \mu \frac{1}{\bar{\lambda}_1}\frac{1}{S_1}\frac{dz_1^2}{dt} - \frac{1}{2} z_2\, p_2\, \mu \frac{1}{\bar{\lambda}_2}\frac{1}{S_2}\frac{dz_2^2}{dt} = \frac{\gamma\, p_1 \cos\theta_1^*}{S_1} - \frac{\gamma\, p_2 \cos\theta_2^*}{S_2}. \tag{12}$$

On the other hand, adding (8) and (9) produces $2P_j$ which can be injected in (11)

$$\frac{1}{2} p_1\, \mu \frac{1}{\bar{\lambda}_1}\frac{1}{S_1}\frac{dz_1^2}{dt} + \frac{1}{2} p_2\, \mu \frac{1}{\bar{\lambda}_2}\frac{1}{S_2}\frac{dz_2^2}{dt} = \frac{\gamma\, p_1 \cos\theta_1^*}{S_1} + \frac{\gamma\, p_2 \cos\theta_2^*}{S_2} - 2\, z_0\, p_0\, \mu \frac{1}{\bar{\lambda}_0}\frac{1}{S_0^2}\left(S_1 \frac{dz_1}{dt} + S_2 \frac{dz_2}{dt}\right). \tag{13}$$

For simplicity let us note $A_0 = p_0\, \mu/\bar{\lambda}_0$, $A_1 = p_1\, \mu/\bar{\lambda}_1$, $A_2 = p_2\, \mu/\bar{\lambda}_2$, and $B_1 = \gamma\, p_1 \cos\theta_1^*$, $B_2 = \gamma\, p_2 \cos\theta_2^*$. Addition and subtraction of (12) and (13) yield the two equations

$$A_1 \frac{dz_1^2}{dt} = 2B_1 - 2z_0\, A_0 \frac{S_1}{S_0^2}\left(S_1 \frac{dz_1}{dt} + S_2 \frac{dz_2}{dt}\right) \tag{14}$$

and

$$A_2 \frac{dz_2^2}{dt} = 2B_2 - 2z_0\, A_0 \frac{S_2}{S_0^2}\left(S_1 \frac{dz_1}{dt} + S_2 \frac{dz_2}{dt}\right). \tag{15}$$

Integration of (14) and (15), taking into account that $z_1 = z_2 = 0$ when $t = t_0$, yields

$$z_1^2 + 2z_0 \frac{A_0}{A_1}\frac{S_1}{S_0^2}(S_1 z_1 + S_2 z_2) = \frac{2B_1}{A_1}\tau. \quad (16)$$

and

$$z_2^2 + 2z_0 \frac{A_0}{A_2}\frac{S_2}{S_0^2}(S_1 z_1 + S_2 z_2) = \frac{2B_2}{A_2}\tau. \quad (17)$$

where $\tau = t - t_0$. In the general case, because of their coupling, the solution of the system of equations (16) and (17) requires the help of numerical methods. Symmetrical bifurcation—identical cross section of the daughter channels—is an exception for which a closed form solution exists.

4.3.3 *Symmetrical bifurcation.*

Let us analyze the simplest case where the two daughter branches have identical cross sections $S = S_1 = S_2$. Then it is easy to show that $A = A_1 = A_2$ and $B = B_1 = B_2$. Substituting these values in (16) and (17) and subtracting the two equations yield $z_1 \equiv z_2$. This agrees with the experimental results of Figure 4.8, where a flow of nonanol—stained in blue—divides symmetrically at a bifurcation.

We are left with a unique equation

$$z^2 + \left(4z_0 \frac{A_0}{A}\frac{S^2}{S_0^2}\right) z = \frac{2B}{A}\tau. \quad (18)$$

If the length of the root channel z_0 is small (and at the limit $z_0 = 0$), we retrieve the solution given by the generalized Lucas-Washburn-Rideal model ($z^2 = \frac{2B}{A}t = \frac{\gamma}{\mu}2\bar{\lambda}\cos\theta^* t$). However, if

z_0 is not small, the solution is not $z^2 \sim t$ anymore because of the first order term at the left-hand side of (18). For simplicity, we note $K_1 = 4z_0 \frac{A_0}{A}\frac{S^2}{S_0^2}$ and $K_2 = \frac{2B}{A}$, and equation (18) becomes

$$z^2 + K_1 z - K_2 \tau = 0. \qquad (19)$$

Relation (19) is quadratic in z. The solution can be written as

$$z(t) = \frac{-K_1 + \sqrt{K_1^2 + 4K_2\tau}}{2}. \qquad (20)$$

If we denote by the index "0" the characteristics of the root channel, and by the index "a" the characteristics of the channels after the symmetrical bifurcation, two constants appear $K_{2,0} = 2B_0/A_0$ and $K_{2,a} = 2B_a/A_a$. The total travel distance at time t is

$$Z(t) = z(t) = \sqrt{K_{2,0}t} \qquad \text{for } t<t_0$$

$$Z(t) = z_0 + \frac{-K_1 + \sqrt{K_1^2 + 4K_{2,a}(t-t_0)}}{2}. \quad \text{for } t>t_0 \qquad (21)$$

The capillary flow velocity is then

$$V(t) = \frac{1}{2}\sqrt{\frac{K_{2,0}}{t}} \qquad \text{for } t<t_0$$

$$V(t) = \frac{K_{2,a}}{\sqrt{K_1^2 + 4K_{2,a}(t-t_0)}}. \text{ for } t>t_0 \qquad (22)$$

Figure 4.9 shows a comparison between experimental and theoretical results for a capillary flow of nonanol in the channels depicted in Figure 4.8. All the channels (root and daughter channels) are identical and have the dimensions indicated in Figure 4.2.

Note that the velocities in the daughter channels are less than that corresponding to the undivided channel, because the local slope is smaller after the bifurcation. However, the flow rate is larger when adding the contributions of the two channels. Figure 4.10 compares the flow rates in the case of the unique channel and the case of the bifurcation. The flow rate is nearly doubled by the presence of the bifurcation.

4.3.4 *Asymmetrical bifurcation.*

The solution of the system (16) and (17) for asymmetrical bifurcations is more complicated to obtain. A numerical approach is required. Using the notations $K_1 = z_0 \frac{A_0}{A}\frac{S_1^2}{S_0^2}$, $K_2 = z_0 \frac{A_0}{A}\frac{S_2^2}{S_0^2}$, and $K_{12} = 2z_0 \frac{A_0}{A}\frac{S_1 S_2}{S_0^2}$, we set up the numerical scheme

$$z_{1,i+1} = -K_1 + \sqrt{K_1^2 + K_{12} z_{2,i} - \frac{2B_1}{A_1}\tau}$$

$$z_{2,i+1} = -K_2 + \sqrt{K_2^2 + K_{12} z_{1,i+1} - \frac{2B_2}{A_2}\tau}\,, \qquad (23)$$

where i is the iteration index (see SI section 2.2 for more details). Using an initial value $z_{1,0} = 0$, $z_{2,1}$ is obtained by solving the second quadratic equation. Inserting $z_{2,1}$ in the first quadratic equation one obtains $z_{1,1}$. The process is repeated until convergence. It was observed that convergence is fast (6 iterations approximately to reach stabilization at less than 5 μm) if the seed ($z_{1,0}$ or $z_{2,0}$) corresponds to the "slowest" channel. Divergence may occur if the seed is that of the

"fastest" channel. At the present time, we do not have a mathematical explanation for this behavior. Upon convergence of the coupled numerical equations, one finds the travel distances at time τ. An example is shown in Figure 4.11. In this example the root channel has a length of z_0 = 98 mm, and its geometry is indicated in Figure 4.2. The first daughter is geometrically identical to the root channel, while the second daughter channel cross section is homothetic with a ratio of ½. In such a case, it can be shown that the average friction length in the small channel is half that of the large channel: $\bar{\lambda}_2 = ½\ \bar{\lambda}_1$. On the other hand, the Cassie angle does not change $\theta_2^* = \theta_1^*$. Hence the characteristic expression of eq (4) is $\bar{\lambda}_2 cos\theta_2^* = 1/2\,\bar{\lambda}_1 cos\theta_1^*$. A comparison of the travel distances is shown in Figure 4.12.

The tip of the flow in the smaller channel (w = 0.4 mm) is first ahead of that in the larger channel (w = 0.8 mm), but the situation reverses after t = 80 s. In fact, the travel distance in the channel with the largest value of $\bar{\lambda} cos\theta^*$ is always ahead after a certain time. This observation rejoins that of Mehrabian et al.[21]. The progression in the smaller channel is faster at the beginning because of the sudden increase in the capillary pressure due to the restriction. However, as shown by Berthier et al.[31] the increase of the wall friction in the small channel overcomes the increase of the capillary pressure and results in a decrease of the velocity of the flow. The flow in the largest channel regains its primacy.

4.3.5 *Simple networks.*

In this section we analyze the capillary flow in the open network schematized in Figure 4.13. The capillary flow is decomposed in four steps: (1) flow in the root channel, which has been studied in the first section of this study (uniform cross-section channels); (2) flow at the first bifurcation, which has been studied in the section "bifurcations"; (3) flow at the channel merging

which separates in two between the exit channel and a reverse flow in the "slow" channel; (4) finally once the flows joined in the slow channel and the network is filled, flow in the exit channel. We also investigated the division of the flow at the second intersection, where the two daughter branches connect.

At first sight, it can be treated as a second bifurcation, with the introduction of the travel distance in the exit channel (denoted z_3) and the backwards flow in the "slow" channel (denoted z_{-2}). However, the additional effect of the advancing flow in the "slow" channel must be considered (denoted z_2). The pressure P_b (first fork) can be expressed as a pressure drop from the entrance, and as a balance between friction and capillary pressure in the "slow" branch (index 2)

$$-P_b = L_0\, p_0\, \mu\, \frac{V_0}{\bar{\lambda}_0}\frac{1}{S_0} = -z_2\, p_2\, \mu\, \frac{V_2}{\bar{\lambda}_2}\frac{1}{S_2} + \frac{\gamma\, p_2\, cos\theta_2^*}{S_2}. \quad (24)$$

Similarly, the pressure P_a (second intersection) can be expressed as a combined pressure drop between the root channel and the "fast" channel

$$-P_a = L_0\, p_0\, \mu\, \frac{V_0}{\bar{\lambda}_0}\frac{1}{S_0} + L_1\, p_1\, \mu\, \frac{V_1}{\bar{\lambda}_1}\frac{1}{S_1}, \quad (25)$$

or as the balance between capillary pressure and pressure drop in either the exit channel of the "slow" channel

$$-P_a = -z_3\, p_3\, \mu\, \frac{V_3}{\bar{\lambda}_3}\frac{1}{S_3} + \frac{\gamma\, p_3\, cos\theta_3^*}{S_3} = -z_{-2}\, p_2\, \mu\, \frac{V_{-2}}{\bar{\lambda}_2}\frac{1}{S_2} + \frac{\gamma\, p_2\, cos\theta_2^*}{S_2}, \quad (26)$$

where z_{-2} and V_{-2} are respectively the reverse travel distance and velocity in the daughter (branch 2). Note that z_3 and z_{-2} are counted from point *a*, while z_2 is counted from point *b*.

Mass conservation equations —at nodes *a* and *b*—can be added to the system (24), (25) and (26) resulting in

$$S_0 V_0 = S_1 V_1 + S_2 V_2, \tag{27}$$

and

$$S_1 V_1 = S_2 V_{-2} + S_3 V_3. \tag{28}$$

The system comprises 7 equations (7 equal signs in eqs 24 to 28), and 7 unknowns P_a, P_b, V_0, V_1, V_2, V_{-2} and V_3 (because $V_i = dz_i/dt$). In order to make it tractable, we first simplify the notations, using $A_i = \mu\, p_i/\bar{\lambda}_i$ for i=1,2,3,-2, $B_i = \gamma\, p_i \cos\theta_i^*$ and $K_i = 2\ B_i/A_i$.

The derivation of a tractable system of three equations with the three unknowns z_2, z_{-2} and z_3 is lengthy, and here we present the result (see SI section 3 for additional information). If τ_a denotes the time counted after the second fork, we obtain first a relation between z_3 and z_2

$$z_3^2\ \frac{A_3}{S_3} - z_{-2}^2\ \frac{A_2}{S_2} = \left(\frac{2\,B_3}{S_3} - \frac{2\,B_2}{S_2}\right)\ \tau_a, \tag{29}$$

and then a relation between z_2 and z_{-2}

$$\left(z_2 - z_{2,a}\right)^2 - z_{-2}^2\ =\ 2\,L_1\ \frac{A_1}{A_2}\frac{S_2}{S_1^2}\left(S_2 z_{-2} + S_3 z_3\right), \tag{30}$$

where $z_{2,a}$ is the location of the flow in the "slow" channel at time τ_a. Finally, the third relation between the three unknowns is

$$z_3^2 + 2\left(L_0\frac{A_0}{S_0^2} + L_1\frac{A_1}{S_1^2}\right)\frac{S_3^2}{A_3}z_3 + 2\,L_0\frac{A_0\,S_2S_3}{A_3S_0^2}\left(z_2 - z_{2,a}\right) + 2\left(L_0\frac{A_0S_2S_3}{A_3S_0^2} + L_1\frac{A_1\,S_2S_3}{A_3S_1^2}\right)z_{-2} - K_3\tau_a = 0\,. \quad (31)$$

The solution of the system requires a numerical approach. In the following we give the example of a network where all the cross sections are identical but where the length of the two branches are different $L_1 \neq L_2$. In this case, we have $S_0 = S_1 = S_2 = S_3$, and $A_0 = A_1 = A_2 = A_3$, and $B_0 = B_1 = B_2 = B_3$ (Fig. 14). The bifurcation at node a being symmetrical, gives the relation $z_3 = z_{-2}$

The system then reduces to

$$\left(z_2 - z_{2,a}\right)^2 - (z_3^2 + 4\,L_1\,z_3) = 0$$

$$z_3^2 + 4(L_0 + L_1)z_3 + 2\,L_0\left(z_2 - z_{2,a}\right) - K\tau_a = 0 \quad (32)$$

The solution is obtained by the numerical scheme

$$z_{3,i+1} = -2(L_0 + L_1) + \sqrt{4\,(L_0 + L_1)^2 + K\tau_a - 2\,L_0\left(z_{2,i} - z_{2,a}\right)}$$

$$z_{2,i+1} - z_{2,a} = -2L_0 + \sqrt{4\,L_0^2 - 4\,L_0\,z_{3,j+1} + K\tau_a} \quad (33)$$

In the case of channels of cross section described in Figure 4.2, and using the lengths shown in Figure 4.15, the travel distances in the network are shown in Figure 4.16.

Four sequences are observed (see Figure S4.1 for sequences of images taken). First the capillary flow in the root channel. Second, the bifurcating flows in the two daughter channels (referred to by their travel distances z_1 and z_2). The flow in the two identical daughter branches

progresses at the same speed as long as the channel junction (a) is not reached ($z_1 = z_2$). Third, when the flow in the shorter daughter branch reaches the junction (a), this flow separates in a backflow (z_{-2}) and an exit flow (z_3), while the flow continues in the long daughter branch (z_2).

Note the slow velocity of the flow in the exit channel. Finally, the fourth sequence corresponds to a unique flow in the exit channel (z_3); after that, all the daughter branches are filled (the forward and backflows in the long channel have merged). Note the acceleration of the exit flow in this last sequence.

4.4 MATERIALS AND METHODS

4.4.1 *Channels.*

The devices comprise an inlet port in which the liquid is fed from a pipette, one or two long winding channels, and outlet ports at the extremity of the channels (Figure 4.1). The use of winding channels is required by the dimensions of the solid plate. Previous studies have shown that the turns do not affect the capillary flow in the absence of capillary filaments, as is the case in our study.[24] The cross section of the channel is a vertical groove with a rounded bottom (Figure 4.2). The channels were designed using computer-aided design (CAD) software (Solidworks 2017, Waltham, MA). The design files were converted to G-code using CAM (computer aided manufacturing) software (Sprutcam 10, Naberezhnye Chelny, Russia) for micromilling. Channels were milled in PMMA (Poly(methyl methacrylate) plates of 3.175 mm thickness (#8560K239; McMaster-Carr, Sante Fe Springs, CA) using a 2 flute ball endmill with cutter diameter of 1/32" (TR-2-0313-BN), or a 2 flute square endmill with cutter diameter of 1/16" (TR-0625-S) purchased from Performance Micro Tool, Janesville, WI. The devices were fabricated using a Tormarch PCNC 770 mill (Tormarch, Waunakee, WI).

4.4.2 *Materials.*

In the first part—analysis of the flow in a uniform cross-section rounded U-grooves—different organic liquids were used: pentanol, chloroform, toluene, dodecane, nonanol, and FC-40. Only nonanol was used for the study of the flow behavior at bifurcations and through bypasses. The different physical properties of the five liquids are indicated in Table 4.1.

Chloroform and toluene were purchased from Fisher Scientific. FC-40, dodecane, and nonanol were purchased from Sigma-Aldrich, St. Louis, MO. Pentanol was purchased from Acros Organics (Thermo Fisher Scientific, Waltham, MA). The organic solvents were colored with Solvent Green 3 from Sigma-Aldrich at concentrations of 1.43 mg/mL (dodecane, nonanol, and pentanol) and 0.24 mg/mL (chloroform and toluene). This very low concentration of dye added to the solvents does not seem to affect the values of the liquid properties. FC-40 was not colored and was used as purchased from the manufacturer.

4.4.3 *Imaging.*

Top-view images were recorded using a Nikon-D5300, ultra-high resolution SLR camera. A sheet of millimetric paper was placed under the devices, and the travel distance of the fluid front was measured over time.

4.5 CONCLUSION

In this work, the dynamics of capillary flow in open rounded grooves has been investigated. It is shown that the notions of average friction length and generalized Cassie angle are pertinent to predict the dynamics of the flow. We demonstrated that the product of these two quantities should replace the product of the radius by the cosine of the contact angle in the Lucas-Washburn-Rideal

law. Next, the behavior of the flow at a bifurcation has been studied. The travel distances in the two daughter channels are solutions of two quadratic coupled equations. In the case of an asymmetrical bifurcation, the travel distance of the flow in the narrow channel is first ahead, then behind that in the larger channel. Narrow and large channels are determined by the product of the average friction length by the cosine of the Cassie angle $\bar{\lambda}\, cos\theta^*$. It is shown that well dimensioned bifurcations increase the flow rate in the device.In this perspective, the present study can contribute to the understanding and design of open capillary pumps. Such pumps are usually designed by using ramifications of the main channel. The presented model could then be used to optimize the morphology of capillary pumps. Finally, the flow behavior in simple networks and through bypasses was investigated. It has been shown that the three travel distances after the passage of the flow at the second node (junction) are solutions of three quadratic coupled equations. The coupling of the flows is imposed by the pressures at the nodes (bifurcation or junction). This approach enables the dimensioning of bypasses in capillary networks, which has been found useful for two-phase capillary flows[22,23]. We envision this work will have application in the ongoing field of open microfluidics to create devices to for sample preparation, space science, and biological and chemical analysis.

4.6 FIGURES

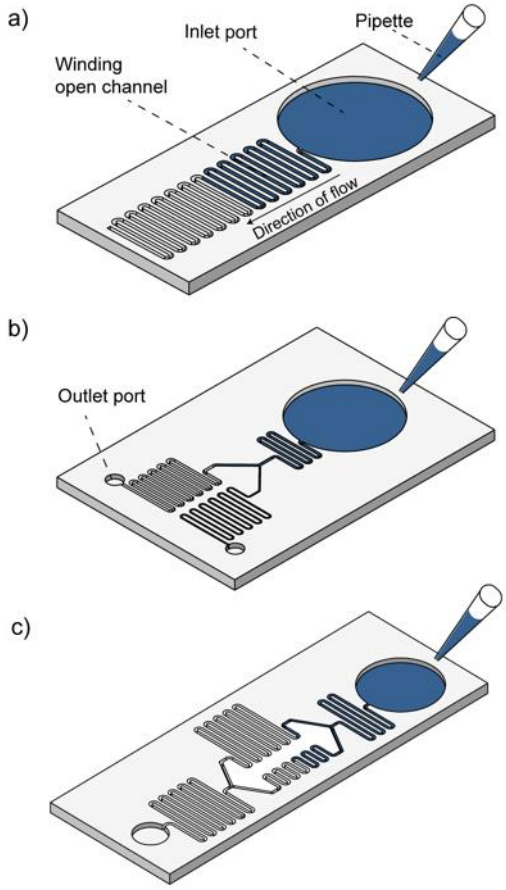

Figure 4.1. Schematic of the open devices:
(a) Simple open-channel. (b). Channel with a bifurcation. (c) Simple network. See SI section 1 for detailed schematics.

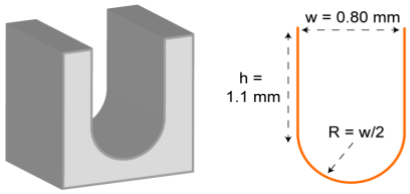

Figure 4.2. Perspective view of the rounded channel and detail of the cross-section.

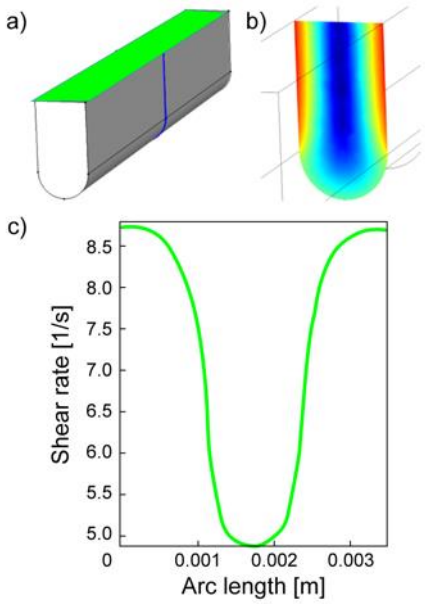

Figure 4.3. (a) View of the channel (the top boundary has a symmetry condition to account for the free surface. (b) Contour plot of the shear rate in a cross section. Blue color represents 0 s^{-1}, green is 5 s^{-1}, and red is 7 s^{-1}. (c) Shear rate profile at the walls.

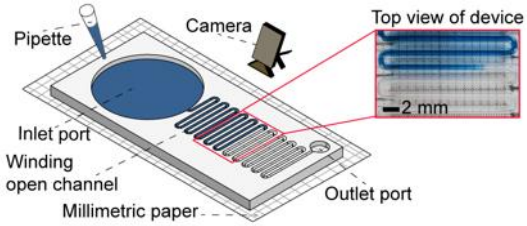

Figure 4.4. Schematic of the measurement of the travel distance of the advancing capillary flow.

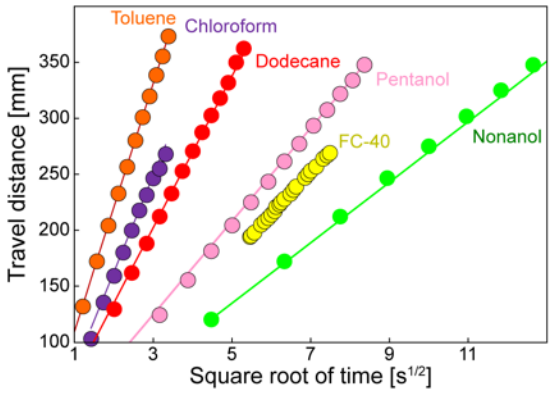

Figure 4.5. Travel distance of the different organic liquids in PMMA channels vs. square

root of time. The dots correspond to the experiments and the continuous lines to theory. Experiments have been done in triplicate, and in all cases, the standard error of the mean was smaller than the symbol plotted.

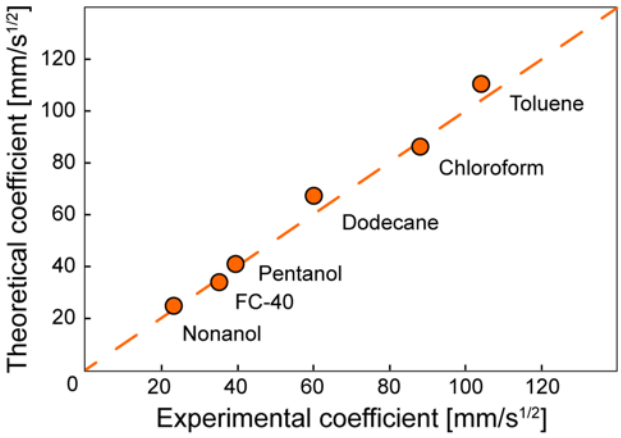

Figure 4.6. Theoretical vs. experimental time coefficient for the six liquids. The diagonal orange dotted line indicates the y = x function, and the circles correspond to the data of Table 4.3.

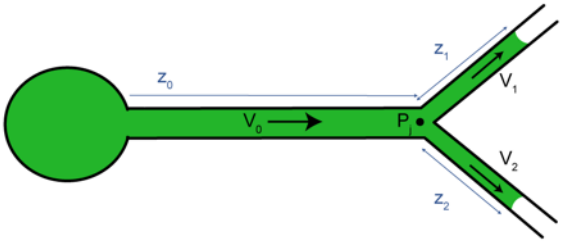

Figure 4.7. Schematic of a bifurcation. The index 0 characterizes the root channel, while indices 1 and 2 refers to the two daughter branches.

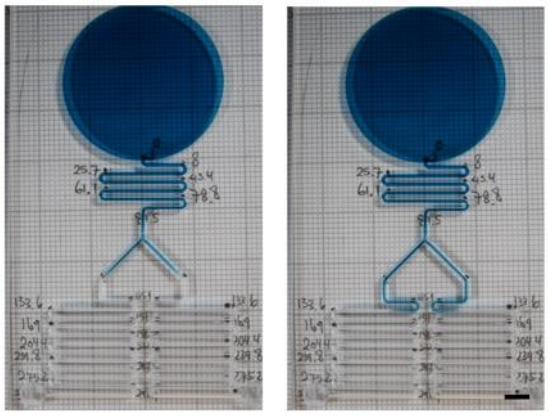

Figure 4.8. The capillary flow of nonanol has the same velocity in each daughter Branches in the case of a symmetrical bifurcation. Scale bar at 5 mm.

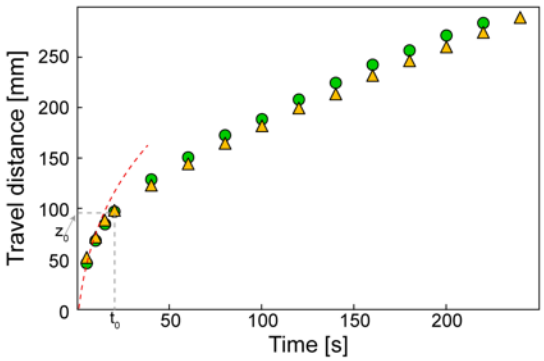

Figure 4.9. Travel distance of nonanol in the open channel with a symmetrical bifurcation: green dots correspond to experiments and yellow triangles to the theory. The red dotted line is the LWR law for the root channel. The root channel length is z_0 = 98 mm and the time at which the flow reaches the bifurcation is t_0 = 20 s. Experiments have been done in triplicate, and in all cases, the standard error of the mean was smaller than the symbol plotted.

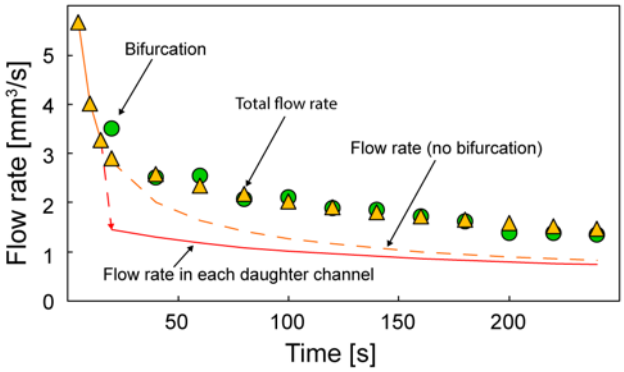

Figure 4.10. Comparison of the flow rates between a single channel and the channel With the bifurcation. The green dots are based on the experimental velocities and the yellow triangles are the model results. The continuous orange line is the flow rate before the bifurcation. The red line corresponds to the flow rate in a single channel after the bifurcation. The dotted orange line corresponds to the flow rate that would exist in the absence of bifurcation. The bifurcation contributes to increase the total flow rate.

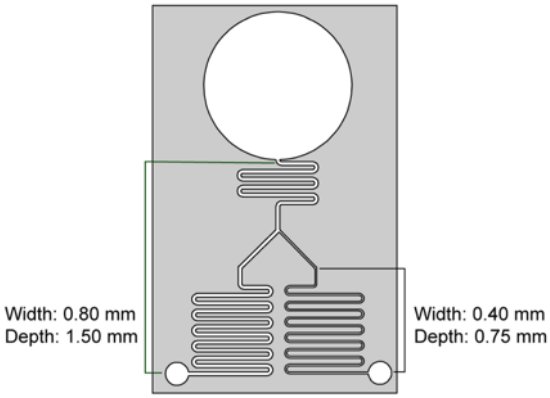

Figure 4.11. Example of asymmetrical bifurcation where the first daughter channel cross section is identical to the root channel cross section and the second daughter channel cross section is homothetical in a ratio ½ (the length of the root channel is z_0 = 90 mm).

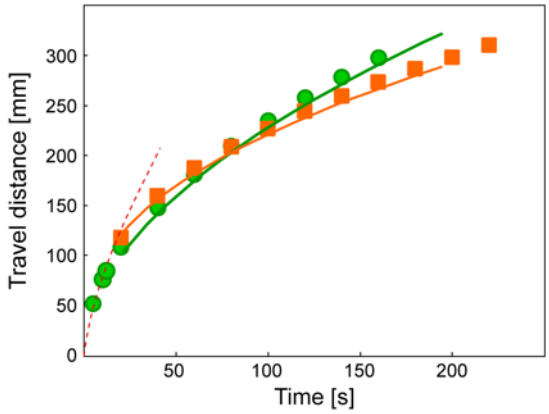

Figure 4.12. Comparison of travel distances in the two daughter channels: the green circles and orange squares correspond respectively to the larger (w = 0.8 mm) and smaller (w = 0.4 mm) channels. The green and orange lines are the results of the numerical approach (eq. 23). The red dotted line represents the LWR law. Experiments have been done in triplicate, and in all cases, the standard error of the mean was smaller than the symbol plotted.

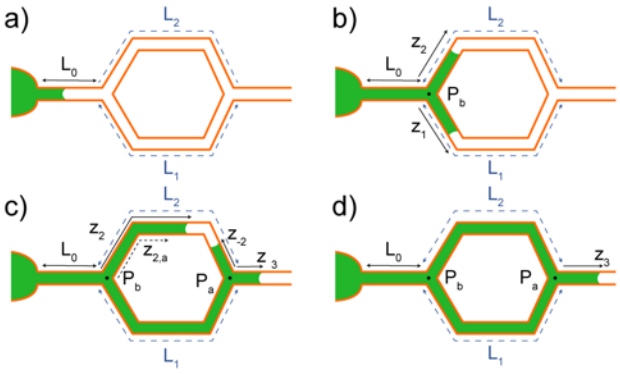

Figure 4.13. Capillary flow in a simple network:

(a) flow in the root channel; (b) the flow separates at the fork; (c) the flow in the faster channel reaches the channel merging point and divides between the exit channel and a back flow in the second branch; (d) both branches are filled and the flow continues in the exit channel.

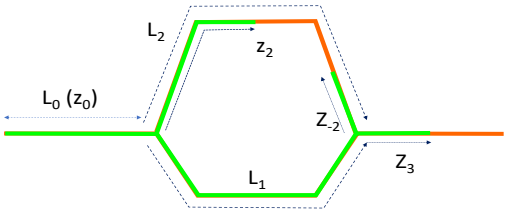

Figure 4.14. Sketch of the network with identical cross sections.

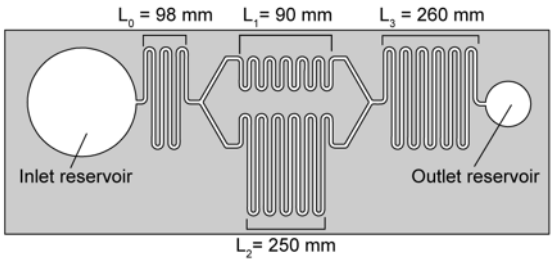

Figure 4.15. View of the network with identical cross sections, and $L_1 \neq L_2$.

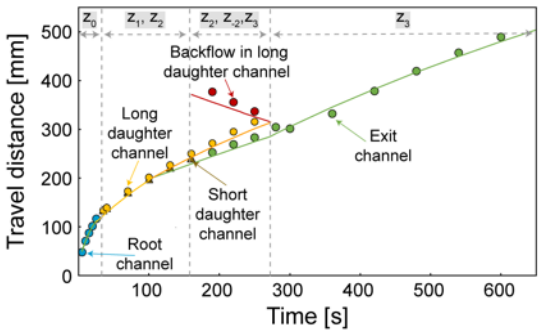

Figure 4.16. The different sequences of the filling of the network: comparison between experiments (dots) and model (continuous lines). Experiments have been done in triplicate, and in all cases, the standard error of the mean was smaller than the symbol plotted.

4.7 TABLES

Table 4.1. Physical properties of the liquids used herein.

Liquid	ρ[a]	μ[c]	γ[d]	γ/μ[g]
Pentanol	814	3.75	25.4	6.8
Chloroform	1490	0.60	27.6[e]	45.8
Toluene	867	0.59	28.5	48.3
Dodecane	750	1.20	25.4	21.0
FC-40	1850[b]	4.5	16.0	6.0
Nonanol	827	11.5	29.5[f]	2.6

[a]Density in kg/m^3 at 20°C[25,26]. [b]At 25°C. [c]Vscosity in mPa·s[25]. Some of the viscosity values were estimated. [d]Surface tension in mN/m at 25°C. [27–29] [e]At 27°C. [f]At 20°C. [g]Units of m/s.

Table 4.2. Contact angles with PMMA walls.

Liquid	θ^a	θ^{*b}
Pentanol	12.5° ± 3.0	52.8°
Chloroform	17.3° ± 1.1	54.0°
Toluene	7.8° ± 1.7	51.9°
Dodecane	26.7° ± 0.7	57.5°
FC-40	12.7° ± 1.3	52.8°
Nonanol	17.0° ± 1.6	52.9°

[a]contact angles of liquids containing dye[30]. [b]generalized Cassie angles

Table 4.3. Experimental and theoretical time coefficients

Solvent	Experimental time coefficient [mm/s$^{1/2}$]	Theoretical time coefficient [mm/s$^{1/2}$]
Pentanol	39.5	41.1
Chloroform	88.0	86.3
Toluene	104.4	110.5
Dodecane	60.0	67.5
FC-40	35.0	34.0
Nonanol	23.0	24.7

4.8 REFERENCES

1. Gervais, L.; Hitzbleck, M.; Delamarche, E. Capillary-Driven Multiparametric Microfluidic Chips for One-Step Immunoassays. Biosens. Bioelectron. 2011, 27 (1), 64–70.
2. Safavieh, R.; Juncker, D. Capillarics: Pre-Programmed, Self-Powered Microfluidic Circuits Built from Capillary Elements. Lab Chip 2013, 13, 4180–4189.
3. Lucas, R. Ueber Das Zeitgesetz Des Kapillaren Aufstiegs von Flüssigkeiten. Kolloid-Zeitschrift 1918, 23, 15–22.
4. Washburn, E. W. The Dynamics of Capillary Flow. Phys. Rev. 1921, 17 (3), 273–283.
5. Rideal, E. K. On the Flow of Liquids under Capillary Pressure. Philos. Mag. Ser. 6 1922, 44, 1152–1159.
6. Bosanquet, C. H. On the Flow of Liquids into Capillary Tubes. Philos. Mag. Ser. 6 1923, 45, 525–531.
7. Quéré, D. Inertial Capillarity. Europhys. Lett. 1997, 39, 533–538.
8. Rye, R. R.; Yost, F. G.; Mann, J. A. Wetting Kinetics in Surface Capillary Grooves. Langmuir 1996, 12, 4625–4627.
9. Yost, F. G.; Rye, R. R.; Mann, J. A. Solder Wetting Kinetics in Narrow V-Grooves. Acta Mater. 1997, 45, 5337–5345.
10. Romero, L. A.; Yost, F. G. Flow in an Open Channel Capillary. J. Fluid Mech. 1996, 322, 109–129.
11. Berthier, J.; Brakke, K. A.; Furlani, E. P.; Karampelas, I. H.; Poher, V.; Gosselin, D.; Cubizolles, M.; Pouteau, P. Whole Blood Spontaneous Capillary Flow in Narrow V-Groove Microchannels. Sensors Actuators, B Chem. 2015, 206, 258–267.
12. Yang, D.; Krasowska, M.; Priest, C.; Popescu, M. N.; Ralston, J. Dynamics of Capillary-Driven Flow in Open Microchannels. J. Phys. Chem. C 2011, 115, 18761–18769.
13. Berthier, J.; Brakke, K. A.; Berthier, E. A General Condition for Spontaneous Capillary Flow in Uniform Cross-Section Microchannels. Microfluid. Nanofluidics 2014, 16, 779–785.
14. Ouali, F. F.; McHale, G.; Javed, H.; Trabi, C.; Shirtcliffe, N. J.; Newton, M. I. Wetting Considerations in Capillary Rise and Imbibition in Closed Square Tubes and Open Rectangular Cross-Section Channels. Microfluid. Nanofluidics 2013, 15 (3), 309–326.
15. Casavant, B. P.; Berthier, E.; Theberge, A. B.; Berthier, J.; Montanez-Sauri, S. I.; Bischel, L. L.; Brakke, K.; Hedman, C. J.; Bushman, W.; Keller, N. P.; et al. Suspended Microfluidics. Proc. Natl. Acad. Sci. U.S.A. 2013, 110, 10111–10116.
16. Berthier, J.; Brakke, K. A.; Gosselin, D.; Bourdat, A.-G.; Nonglaton, G.; Villard, N.; Laffite, G.; Boizot, F.; Costa, G.; Delapierre, G. Suspended Microflows between Vertical Parallel Walls. Microfluid. Nanofluidics 2015, 18, 919–929.
17. Trejo-Soto, C.; Costa-Miracle, E.; Rodriguez-Villarreal, I.; Cid, J.; Alarcón, T.; Hernández-Machado, A. Capillary Filling at the Microscale: Control of Fluid Front Using Geometry. PLoS One 2016, 11 (4), e0153559.
18. Berthier, J.; Gosselin, D.; Berthier, E. A Generalization of the Lucas–Washburn–Rideal Law to Composite Microchannels of Arbitrary Cross Section. Microfluid. Nanofluidics 2015, 19, 497–507.

19. Berthier, J.; Gosselin, D.; Pham, A.; Delapierre, G.; Belgacem, N.; Chaussy, D. Capillary Flow Resistors: Local and Global Resistors. Langmuir 2016, 32 (3), 915–921.
20. Elizalde, E.; Urteaga, R.; Berli, C. L. A. Rational Design of Capillary-Driven Flows for Paper-Based Microfluidics. Lab Chip 2015, 15 (10), 2173–2180.
21. Mehrabian, H.; Gao, P.; Feng, J. J. Wicking Flow through Microchannels. Phys. Fluids 2011, 23 (12), 122108.
22. Berry, S. B.; Lee, J. J.; Jean, B.; Berthier, E.; Theberge, A. B. Open Channel Droplet-Based Microfluidics. In MicroTas International Conference; MicroTas International Conference: Taiwan, 2018.
23. Berry, S. B.; Lee, J. J.; Berthier, J.; Berthier, E.; Theberge, A. B. Open Channel Droplet-Based Microfluidics. bioRxiv 2019, 436675.
24. Berthier, J.; Brakke, K. A.; Gosselin, D.; Navarro, F.; Belgacem, N.; Chaussy, D. Spontaneous Capillary Flow in Curved, Open Microchannels. Microfluid. Nanofluidics 2016, 20 (7), 1–9.
25. Kim, S.; Thiessen, P. A.; Bolton, E. E.; Chen, J.; Fu, G.; Gindulyte, A.; Han, L.; He, J.; He, S.; Shoemaker, B. A.; et al. PubChem Substance and Compound Databases. Nucleic Acids Res. 2016, 44.
26. 3M TM Fluorinert TM Electronic Liquid FC-40 Electrical Properties; 2010.
27. Freitas, A.; Quina, F.; Carroll, F. Estimation of Water-Organic Interfacial Tensions. A Linear Free Energy Relationship Analysis of Interfacial Adhesion. J. Phys. Chem. B 1997, 5647, 7488–7493.
28. Mohammad, A. A.; Alkhaldi, K. H. A. E.; AlTuwaim, M. S.; Al-Jimaz, A. S. Effect of Temperature and Chain Length on the Viscosity and Surface Tension of Binary Systems of N,N-Dimethylformamide with 1-Octanol, 1-Nonanol and 1-Decanol. J. Chem. Thermodyn. 2014, 74, 7–15.
29. Han, Y.; Shikazono, N. Measurement of the Liquid Film Thickness in Micro Tube Slug Flow. Int. J. Heat Fluid Flow 2009, 30, 842–853.
30. Lee, J. J.; Berthier, J.; Brakke, K. A.; Dostie, A. M.; Theberge, A. B.; Berthier, E. Droplet Behavior in Open Biphasic Microfluidics. Langmuir 2018, 34 (18), 5358–5366.
31. Berthier, J.; Brakke, K. A.; Berthier, E. Open Microfluidics; John Wiley & Sons, Inc.: Hoboken, NJ, USA, 2016.
32. Brackbill, J. .; Kothe, D. .; Zemach, C. A Continuum Method for Modeling Surface Tension. J. Comput. Phys. 1992, 100 (2), 335–354.
33. Kolliopoulos, P.; Jochem, K. S.; Lade, R. K.; Francis, L. F.; Kumar, S. Capillary Flow with Evaporation in Open Rectangular Microchannels. Langmuir 2019, 35 (24), 8131–814

Chapter 5. OPEN-CHANNEL CAPILLARY TREES AND CAPILLARY PUMPING

Reproduced in part from Lee, J. J.; Berthier, J.*; Kearney, K. E.; Berthier, E.; Theberge, A. B. Open-channel Capillary Trees and Capillary Pumping. Langmuir 2020, 36, 12795–12803.*

**denotes co-authorship. J.J.L contributed to the overall fabrication designs and experimental designs. J.B. developed the analytical model and numerical simulation of this work.*

5.1 ABSTRACT

Velocity of capillary flow in closed or open channels decreases as the flow proceeds down the length of the channel, varying as the inverse of the square root of time or as the inverse of travel distance. In order to increase the flow rate—and extend the duration of the flow—capillary pumps have been designed by mimicking the pumping principle of paper or cotton fibers. These designs provide a larger volume available for the wicking of the liquids.

In microsystems for biotechnology, different designs have been developed based on experimental observation. In the present manuscript, the mechanisms at the basis of capillary pumping are investigated using a theoretical model for the flow in an open-channel "capillary tree" (i.e., an ensemble of channels with bifurcations mimicking the shape of a tree). The model is checked against experiments. Rules for obtaining better designs of capillary pumps are proposed—specifically we find: (1) when using a capillary tree with identical channel cross-sectional areas throughout, it is possible to maintain nearly constant flow rates throughout the channel network, (2) flow rate can be increased at each branch point of a capillary tree by slightly decreasing the areas of the channel cross section and decreasing the channel lengths at each level of ramification

within the tree, and (3) higher order branching (trifurcations vs. bifurcations) amplify the flow rate effect. This work lays the foundation for increasing the flow rate in open microfluidic channels driven by capillary flow; we expect this to have broad impact across open microfluidics for biological and chemical applications such as cell culture, sample preparation, separations, and on-chip reactions.

5.2 INTRODUCTION

Microfluidic capillary systems use passive capillary forces, rather than traditional active pumping methods, eliminating bulky peripheral equipment and enabling autonomous device operation for field-based applications.[1–5] Open microfluidic capillary systems remove at least one 'wall' of the microfluidic channel, further extending usability and manufacturability;[6,7] these systems have burgeoned in use in diverse fields including cell signaling, organotypic models, metabolomics, sample preparation, diagnostics and bioassays, chemical reactions, and space research.[8–11] To extend the applications of capillary-driven microfluidics, it is necessary to overcome a fundamental limitation of capillary flow—the inherent decrease in flow rate as the flow advances in a microfluidic channel. In this manuscript, we build on prior capillary pumping systems,[4,12] by developing the general theory for velocity (and flow rate) enhancements achievable in capillary pumping systems that mimic the branches of a tree, providing a physical solution that can be applied to wide-ranging biological and chemical applications in both open- and closed-channel microfluidics.

After an evanescent initial inertial phase, a capillary flow is governed by the balance between capillary force and wall friction. This analysis was first done by Lucas, Washburn, and Rideal for cylindrical tubes in the 1920s.[13–15] Shortly after, Bosanquet established the general

equation of the motion of fluids in capillary channels.[16] Capillary flow in open grooves is more recent, with the investigation of the capillary flow in V-grooves for solder flow for microelectronics[17–20] and for space "plumbing".[21,22] Recently, it was shown that the Lucas-Washburn-Rideal (LWR) law should be modified to account for arbitrary shaped closed channels and open channels.[23–27] It was shown that, for an arbitrary morphology, closed or open, provided that the cross-sectional area is uniform, the velocity of capillary flow decreases as the inverse of the square root of time or as the inverse of the travel distance, using an adapted generalized Lucas-Washburn law.[6,7,28]

This dependency indicates that the capillary flow rate decreases rapidly. In order to maintain an enough flow rate—and at the same time, extend the duration of the flow—capillary pumps have been conceived. Their design mimics the structure of paper or threads or the arborescence of a tree.[29–31] These materials provide a large volume available for the wicking of the liquids and maintain a significant flow rate in the root channel.

In microsystems for biotechnology, many different designs have been experimentally developed for closed systems.[3,12] Figure 5.1 shows two designs having the shape of a tree.

Here, the mechanisms at the basis of capillary pumping in open channels are investigated based on the analysis of the flow in a "capillary tree" (i.e., an ensemble of channels with bifurcations mimicking the shape of a tree). Shou et al. have theoretically studied closed cylindrical networks, however they did not include experiments).[32] As Shou, we conclude that LWR law must be modified to account for the ramifications.

Velocity (and flow rate) decreases steadily in uniform cross section open channels. If one wants to avoid this decrease in the "root channel" i.e., the channel of interest for biological or chemical applications, a capillary pumping device should be added behind the root channel (Figure

5.2). We first show that a capillary tree with identical cross section provides a nearly constant flow rate in the root channel. It is assumed that the capillary tree is "symmetrical", i.e., all branches at the same level of ramification are identical. Then, the travel distance is the same for each path, and is obtained by writing the balance between the capillary force on the advancing meniscus and the wall friction along the path. Second, we show that an improved capillary tree (with decreasing cross-sectional areas and small lengths) may even increase the flow rate in the root channel. The approach is done considering an open system, but readily applies to closed systems. The model is checked against experiments performed with nonanol flowing in open microfluidic channels (U-grooves) milled in poly(methyl methacrylate). Our approach unveils a path for designing efficient capillary pumps with marked flow rate enhancements.

5.3 THEORY

We first examine the case of a simple capillary network, which has the shape of a tree (Figure 5.4). In order to simplify the first algebraic developments, all the channels are assumed to have the same cross section. In such a case, the flow is "symmetrical", i.e., the advancing menisci of the flow are theoretically located at the same place in all daughter channels of each level.

Starting with the root channel: The travel distance z_0 in the root channel is given by the balance between friction and capillary force[6]

$$p\, z_0 \underline{\tau} = p\, z_0 \left(\mu \frac{V_0}{\underline{\lambda}}\right) = p\, \gamma\, cos\theta^* \qquad (1)$$

where $\underline{\tau}$ is the average friction, p the channel perimeter in a cross section, V_0 the average velocity (which is a function of time and/or travel distance), $\underline{\lambda}$ the average friction length,[6] μ the viscosity,

γ the surface tension, and θ^* the generalized Cassie angle (in order to take into account the free surface of the open channel[6,9] and accommodate for the potential of non-monolithic channels comprising different materials on the floor and walls; see SI section 1 for definition of generalized Cassie angle). Then we have the relation between travel distance and time

$$\frac{d\, z_0^2}{dt} = \frac{2\, \underline{\lambda}\, \gamma\, cos\theta^*}{\mu}, \tag{2}$$

And finally

$$z_0 = \sqrt{\frac{2\, \underline{\lambda}\, \gamma\, cos\theta^*}{\mu}}\, \sqrt{t}\,. \tag{3}$$

Note that the time at which the flow reaches the bifurcation at a distance L_0 from entrance, is

$$t_0 = \frac{\mu}{2\, \underline{\lambda}\, \gamma\, cos\theta^*}\, L_0^2 = \frac{L_0^2}{C}. \tag{4}$$

where $C = \frac{2\, \underline{\lambda}\, \gamma\, cos\theta^*}{\mu}$. After the first bifurcation, we must use a formulation that uses the pressures and write the pressure equilibrium along a fluidic path.[35,38]

$$p\, L_0\, \mu \frac{V_0}{\underline{\lambda}} \frac{1}{S} + p\, z_1\, \mu \frac{V_1}{\underline{\lambda}} \frac{1}{S} = \frac{p\, \gamma\, cos\theta^*}{S}, \tag{5}$$

where z_1 here is the travel distance in the first ramification, S the cross-sectional area and V_1 the velocity in the daughter branch ($V_1 = \frac{dz_1}{dt}$). Note that because of the assumption that the daughter branches have the same cross section as the root channel, S simplifies in (5), and there is a unique

friction length $\underline{\lambda}$ and a unique Cassie angle θ^*. Integrating (5) with the condition $t=t_0$, $z_1=0$, and considering the mass conservation $S\,V_0 = 2\,S\,V_1$, yields

$$z_1^2 + 4L_0 z_1 - C\,(t - t_0) = 0\,. \tag{6}$$

And the solution is simply

$$z_1 = -2L_0 + \sqrt{4\,L_0^2 + C(t - t_0)}\,. \tag{7}$$

Note that the total travel distance is

$$Z = L_0 + z_1 = -L_0 + \sqrt{3\,L_0^2 + C\,t}\,. \tag{8}$$

The time t_1 at which the flow reaches the end of the first branches (second bifurcations) along a distance L_1, is

$$t_1 = t_0 + L_1\,\frac{(L_1+4L_0)}{C} = \frac{(L_1+L_0)^2+2L_0L_1}{C}. \tag{9}$$

Let us proceed to the next level of ramification. The capillary pressure is still the same (since the channel cross section is uniform) but the wall friction increases.

$$p\,L_0\,\mu\frac{V_0}{\underline{\lambda}}\frac{1}{S} + p\,L_1\,\mu\frac{V_1}{\underline{\lambda}}\frac{1}{S} + p\,z_2\,\mu\frac{V_2}{\underline{\lambda}}\frac{1}{S} = \frac{p\,\gamma\,cos\theta^*}{S}. \tag{10}$$

Integration of (10) with the condition

$t = t_1$, $z_2 = 0$, considering the mass conservation $S\,V_0 = 2\,S\,V_1 = 4\,S\,V_2$ yields

$$z_2^2 + 2\,(4L_0 + 2L_1)z_2 - C\,(t - t_1) = 0, \tag{11}$$

and

$$z_2 = -(4L_0 + 2L_1) + \sqrt{(4L_0 + 2L_1)^2 + C(t - t_1)}. \tag{12}$$

Note that the total travel distance is

$$Z = L_0 + L_1 + z_2 = -3L_0 - L_1 + \sqrt{(4L_0 + 2L_1)^2 + C(t - t_1)}. \tag{13}$$

The time t_2 at which the flow reaches the end of the second branches (third bifurcations) is

$$t_2 - t_1 = L_2 \frac{(L_2 + 4L_1 + 8L_0)}{C}. \tag{14}$$

An approach using recurrence leads to the general formula for the daughter branch number n

$$z_n = -(2^n L_0 + 2^{n-1}L_1 + \cdots + 2\,L_{n-1}) + \sqrt{(2^n L_0 + 2^{n-1}L_1 + \cdots + 2\,L_{n-1})^2 + C(t - t_{n-1})} \tag{15}$$

and

$$t_n - t_{n-1} = L_n \frac{\left(L_n + 2^2 L_{n-1} + \cdots + 2^{n+1} L_0\right)}{C} . \quad (16)$$

In the following sections, we use the theoretical model to determine the travel distances and flow rates for three different capillary trees and compare the model with experimental results.

5.4 Results and Discussion

References to SI can be found in Appendix B

5.4.1 *Comparison with experiments.*

Figure 5.5 shows still images taken from a video of the open-channel capillary flow progressing in the capillary tree (See SI Figure S4 for the device design). The plot of the travel distances versus time is shown in Figure 5.6a. The travel distance – theoretically identical in all subchannels due to the symmetry of the tree – is calculated from equation (15) using Excel software. Elapsed time is incremented stepwise starting at time 0 seconds where the flow enters the root channel. First, using equation (3) for the root channel, the time t_0 when the flow exits the root channel is determined. Then, using equation (15) for n = 1, the time t_1 where the flow exits the first daughter branches, is determined, and so on, until the last ramifications. Derivation of the travel distance versus time then yields the velocities in the capillary tree. Note that after the first bifurcation, the velocities are nearly constant in the device. The analytical form of the velocity in the capillary tree is given by derivation of (15)

$$V_n = \frac{1}{2} \frac{C}{\sqrt{A_n^2 + C(t - t_{n-1})}} , \quad (17)$$

where A_n is a constant depending on the daughter channels lengths and ramification level.

At each bifurcation, there is a negative jump of velocity. It is similar to what is observed with a widening of a unique channel.[39–41] On the other hand, the total flow rate is nearly constant after the second level of bifurcations, as shown in Figure 5.6b. Using (17), flow rates are given by

$$Q_n = \frac{C}{\sqrt{A_n^2 + C(t - t_{n-1})}} 2^{(n-1)}\, S. \qquad (18)$$

The velocity of the tip of the flow is the time derivative of the travel distance given by equation (15) where $V_n = dz_n/dt$. Denoting $A_n = 2^n L_0 + \cdots + 2^{n-1} L_{n-1}$, we obtain equation (17) for the velocity at the tip of the flow. The flow rate at the tip of the flow is obtained by multiplying the velocity by the cross-sectional area. Finally, the total flow rate (in the root channel) is obtained by adding the contribution of all the flow tips, resulting in equation (18). The term 2^{n-1} accounts for the summation for the bifurcating trees. For trifurcating trees, this would be 3^{n-1}.

In the following section, we investigate the effect of a progressive decrease of the cross-sectional areas of the channels.

5.4.2 *Decreasing cross-sectional areas and capillary pumping.*

Let us now consider a capillary tree where the cross sections decrease by a homothetic ratio (i.e., channel width and height decrease by the same factor) from one level to the next.

5.4.3 *Bifurcating capillary trees.*

In a first step, we investigate capillary trees where channels divisions are bifurcations (two daughter channels for one mother channel), as shown in Figure 5.7. In such a case the cross-sectional perimeters are

$$p_n = \alpha p_{n-1} = \cdots = \alpha^{n-1} p_1 = \alpha^n p_0, \tag{19}$$

and the cross-sectional areas are

$$S_n = \alpha^2 S_{n-1} = \cdots = \alpha^{2(n-1)} S_1 = \alpha^{2n} S_0. \tag{20}$$

Moreover, the friction lengths are homothetic because they are proportional to the hydraulic diameter of the channel

$$\underline{\lambda}_n = \alpha \underline{\lambda}_{n-1} = \cdots = \alpha^{n-1} \underline{\lambda}_1 = \alpha^n \underline{\lambda}_0. \tag{21}$$

Hence the ratio $\frac{p}{\underline{\lambda}}$ is constant, equal to $\frac{p_0}{\underline{\lambda}_0}$. Moreover, the Cassie angles are everywhere the same, i.e., $\theta^* = \theta_1^* = \cdots = \theta_n^*$. Generalizing (10), considering the change of the cross section at each ramification level, we obtain

$$\alpha^{2n} L_0 V_0 + \alpha^{2(n-1)} L_1 V_1 + .. + \alpha^2 L_{n-1} V_{n-1} + z_n V_n = \frac{p_n}{p_0} \frac{\gamma}{\mu} \underline{\lambda}_0 \cos\theta^* = \alpha^n \frac{\gamma}{\mu} \underline{\lambda}_0 \cos\theta^* = \alpha^n \frac{C}{2}. \tag{22}$$

The mass conservation equation yields

$$V_0 = (2\ \alpha^2)V_1 = (2\ \alpha^2)^2\ V_2 = \cdots = (2\ \alpha^2)^n\ V_n, \tag{23}$$

We then can integrate (22) under the form of a quadratic polynomial in z_n

$$z_n^{\,2} + 2\left[2^n\alpha^{4n}L_0\ +\ 2^{n-1}\ \alpha^{4(n-1)}\ L_1 + \cdots + 2\alpha^4 L_{n-1}\right]z_n = \alpha^n C\ (t - t_{n-1}), \tag{24}$$

And the solution is

$$z_n = -\left[2^n\alpha^{4n}L_0\ +\ 2^{n-1}\ \alpha^{4(n-1)}\ L_1 + \cdots + 2\alpha^4 L_{n-1}\right] + \left\{\left[2^n\alpha^{4n}L_0\ +\ 2^{n-1}\ \alpha^{4(n-1)}\ L_1 + \cdots + 2\alpha^4 L_{n-1}\right]^2 + \alpha^n C\ (t - t_{n-1})\right\}^{\frac{1}{2}}. \tag{25}$$

It is easily verified that, for α = 1, equation (25) reduces to equation (15). Figure 5.8 shows the results for the device shown in Figure 5.7 (α = 0.85).

5.4.4 *Trifurcating capillary trees.*

In this section, the flow behavior in a trifurcating capillary tree is investigated. Figure 5.9 shows the device used for performing the experiments. Here, the capillary flow first divides in the two “exterior” channels because of the immediate presence of the walls, but the flow equilibrates somewhat later (sometimes a small delay in the middle channel can be observed). In the case of trifurcating devices, the approach is like that of the preceding section. However, the mass conservation equation (23) becomes

$$V_0 = (3\alpha^2)V_1 = (3\alpha^2)^2\ V_2 = \cdots = (3\alpha^2)^n\ V_n. \tag{26}$$

Then, in a similar integration as for equation (22), we obtain the solution

$$z_n = -\left[3^n \alpha^{4n} L_0 + 3^{n-1} \alpha^{4(n-1)} L_1 + \cdots + 3\alpha^4 L_{n-1}\right] + \left\{\left[3^n \alpha^{4n} L_0 + 3^{n-1} \alpha^{4(n-1)} L_1 + \cdots + 3\alpha^4 L_{n-1}\right]^2 + \alpha^n C\,(t - t_{n-1})\right\}^{\frac{1}{2}}. \quad (27)$$

Using the geometrical data of Figure 5.9, we obtain the travel distances vs. time shown in Figure 5.10.

5.4.5 *Discussion*

In the preceding sections, we have shown that the theoretical model reproduces well experimental travel distances in capillary trees. Moreover, it has been shown that the travel distances in the different branches of the tree are not of the form $z = \sqrt{A\,t}$, but of the form $z = A + \sqrt{B + Ct}$. A similar relation was also obtained in the case of networks.[35]

Let us now consider the flow rates. A comparison between all the cases studied here is shown in Figure 5.11. As expected, the trifurcating capillary tree with decreasing cross sections produces the highest flow rates.

Let us now consider the question: what morphology of the capillary tree produces the highest flow rate? In other words, what morphology corresponds to the best pumping efficiency? In the following, we do not consider the feasibility of the fabrication, but only the theoretical optimum.

The parameters of the geometry of the capillary tree are (1) the number of divisions at each ramification, (2) the lengths of the flow channels, and (3) the homothetic ratio for the cross sections

of the flow channels between each ramification. Note that relations (25) and (27) can be generalized to a higher number of divisions at each ramification. In such case, the coefficients 2 in (25) and 3 in (27) are replaced by the number of divisions. The number of parameters is large, making it difficult to detail the influence of each parameters. In the simplified case of daughter channels of equal length, a mathematical approach can be done and is presented in SI section 2-4. The approach concludes that short channels lengths, large number of sub-channels at a division (node) and homothetic ratios of the order of 0.7 - 0.8 produce the highest flow rate. In the following, we use our model to analyze more concretely the influence of the parameters.

In order to answer these questions, let us consider a two capillary trees with 4 ramification levels and a homothetic ratio $\alpha = 0.8$ between each level. These capillary trees have flow segments of much shorter lengths than that considered before, of the order of 10 to 20 mm only. The different lengths and cross sections are listed in Table 5.3.

The calculated travel distances and flow rates are shown in Figure 5.12 and 5.13 for cases #1 and #2 respectively.

Clearly, the shorter channels lengths associated to the progressive reduction of the cross-sectional areas have the effect to bring the travel distances closer with that of the generalized/modified LWR (Lucas-Washburn-Rideal) law for the case of the single channel. Homothetically decreasing the channel cross-sectional areas increases the total flow rate, as shown in Figure 5.13. Even if the flow velocity suddenly decreases at each bifurcation, the total flow rate increases because of the contribution of the additional daughter branches. Hence, an important increase of flow rates is obtained by the reduction of the channel lengths and of the cross sections at each bifurcation, when the length of the branches is sufficiently small.

5.5 MATERIALS AND METHODS

5.5.1 *Capillary tree channels.*

The devices comprise a wide inlet port in which the liquid is fed from a pipette, and outlet ports at the extremity of the channels (see SI section 5 for the schematic of the devices). In this work, open rounded channels of different lengths, widths and depths have been used (dimensions given in Figures 5.6, 5.8, and S4 and S5).

The use of winding channels is required due to the dimensions of the solid plate. Previous studies have shown that the turns do not affect the capillary flow in the absence of capillary filaments, as is the case in our study due to the U-shaped channel cross section.[33] A typical channel cross section is shown in Figure 5.3. The cross section of the channel is a vertical groove with a rounded bottom, which avoids the formation of filaments observed in channels of rectangular cross section.

We investigate first the flow behavior in capillary trees with the same cross section as that of Figure 5.3 in the whole tree. The average friction length (we will see later the use of the friction length) was estimated to be $\underline{\lambda} \sim 200$ µm (calculated using COMSOL[34]) for the homothetic channel of 0.80 mm of width, in our preceding study.[35] The friction length was defined in an early publication[35] (and included again here in SI section 6) Using an approximate homothetic ratio, an estimate of the friction length in the root channel of 1.06 mm of width is 259 µm.

Secondly, we investigate the case of capillary trees with homothetically decreasing channel cross sections. The different characteristics of the cross sections are given in the Table 5.1.

The channels were designed using computer-aided design (CAD) software (Solidworks 2017, Waltham, MA). The design files were converted to G-code using CAM (computer aided

manufacturing) software (Fusion 350) for micromilling. Channels were milled in PMMA (poly(methyl methacrylate) plates of 3.175 mm thickness (#8560K239; McMaster-Carr, Santa Fe Springs, CA) using a 2 flute ball endmill with cutter diameter of 1/32" (TR-2-0313-BN), or a 2 flute square endmill with cutter diameter of 1/16" (TR-0625-S) purchased from Performance Micro Tool, Janesville, WI. The devices were fabricated using a Datron Neo computer numerical control (CNC) mill (Datron, Germany). Roughness of the channel bottom is of the order of a few microns, one order of magnitude less than the values that would produce velocity fluctuations as observed by Lade.[27]

5.5.2 *Materials.*

Nonanol was used for the study as it is a low-volatility solvent (boiling point 213 °C), mitigating evaporation. The physical properties of nonanol are indicated in Table 5.2.[36,37] Nonanol has been colored with Solvent Green 3 from Sigma-Aldrich at concentrations of 1.43 mg/mL. The volume of nonanol added to the inlet channel was ~ 1.2 mL. Additional nonanol was added, once fluid reached third branch in the bifurcation device. This is to maintain a flat meniscus in the inlet.

5.5.3 *Imaging.*

Top-view images were recorded using a Nikon-D5300, ultra-high resolution SLR camera.

5.6 CONCLUSION

The present analysis demonstrates the possibility of obtaining nearly constant flow rates by using a capillary tree of same cross-sectional areas. Once the flow has invaded the root channel and is divided in the daughter branches, the fluid velocity is nearly constant in the wetted channels.

This solves a significant problem in capillary-driven microfluidics: decrease in fluid flow rate along the length of the channel that is observed in simple non-bifurcating channels.

Moreover, it is shown that decreasing the channel lengths and slightly decreasing the areas of the channel cross section at each level of the tree has the effect to stepwise increase the flow rate each time that the tip of the flow passes a bifurcation. A more pronounced effect is obtained with trifurcations. Hence, this work provides insight into the physics of capillary pumping: in order to obtain efficient pumping, the capillary network should be constituted of channels of small lengths and of (slightly) decreasing cross sections. We expect this insight to be useful when designing capillary-driven microfluidic systems for applications requiring efficient flow of a volume of fluid that would be challenging to deliver with non-bifurcating channels. Potential applications include sample preparation, cell culture, assay workflows (reagent delivery, washing, etc.), and chemical reactions.

A limitation to flow rate amplification stems from geometrical and fabrication considerations. For example, the reduction of the dimensions of the cross section with a homothetic factor of 0.8 results in channel widths of 1000, 800, 640, 512, 410, 328 and 262 μm for a six-level capillary tree. One reaches quickly the limits of milling channels in a plastic plate, first because of the smaller dimensions of the endmill, and second, because of the steric arrangement of the tree in the substrate (the overall device footprint).

However, methods other than milling are commonly used in microfluidic device fabrication, and our work here provides a general framework for evaluating flow rate gain in capillary trees with channels of any dimension.

Finally, we remark that the most efficient pumping—obtained by using very short channels with many divisions—has a morphology resembling that of fibrous media. In order to have a

pumping efficiency similar to that of a fibrous media, the characteristic length of the capillary tree should be of the same order of the characteristic dimension of the fibrous media. We assume this is the reason why it is found impossible to extract by capillary means liquid from a fibrous media towards open channels provided that the open channel has a radius larger than the effective capillary radius in the pore space.

5.7 FIGURES

Figure 5.1. Tree-line capillary pump designs from Zimmermann et al.[12]

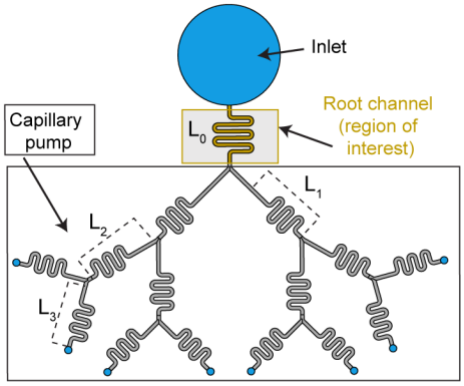

Figure 5.2. Schematic showing a capillary pump (in the form of a tree-like structure). Capillary pump can be placed downstream of any channel of interest. We included a small winding channel labelled root channel as an example channel of interest where biological or chemical applications could take place**.**

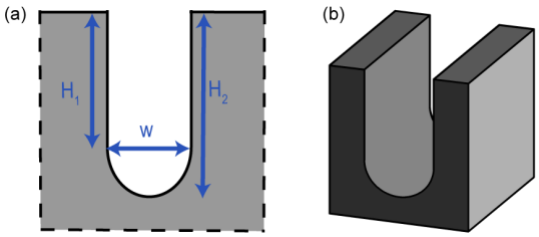

Figure 5.3. (a) Detail of the cross section.
(b) Perspective view of the rounded channel.

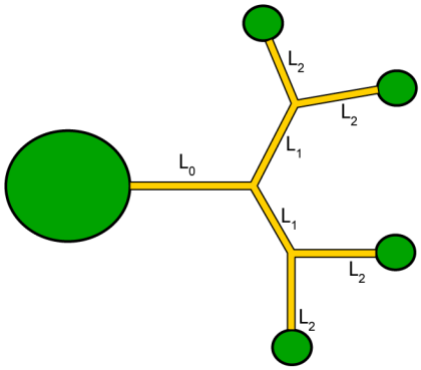

Figure 5.4. Schematic of the capillary tree with the inlet port (left) and the four outlet ports.

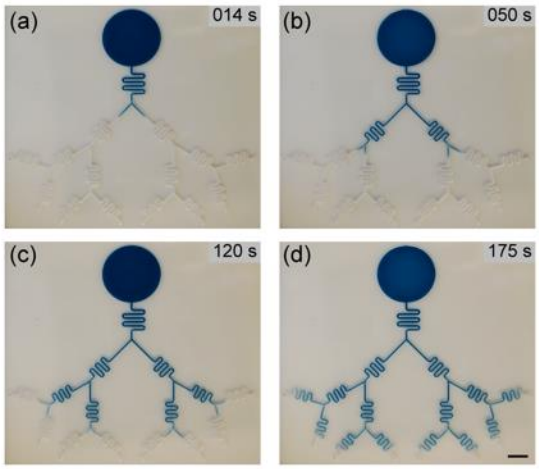

Figure 5.5. Progression of the nonanol (dyed blue for visualization) in the capillary tree at (a) the first bifurcation, (b) the second bifurcation, (c) the third bifurcation and in (d) almost reaching the end of the channel. Scale bar = 1 cm.

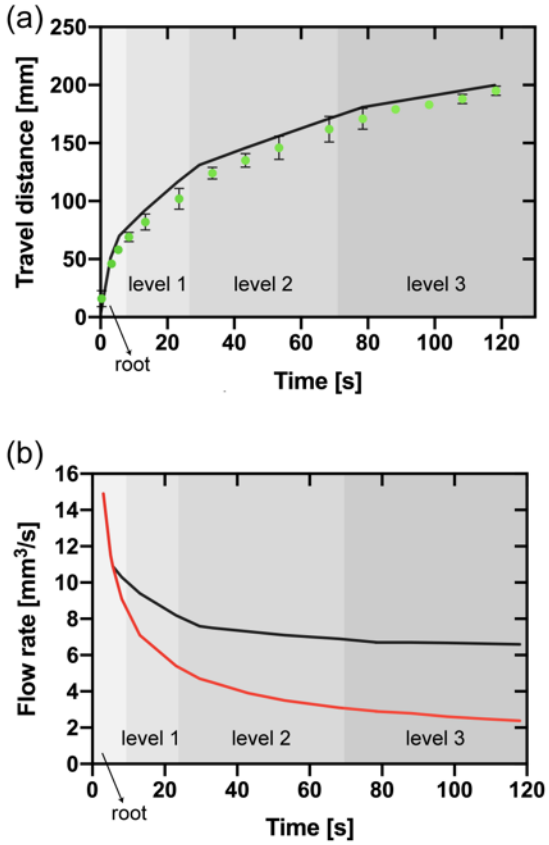

Figure 5.6. (a) Travel distances in the bifurcating capillary tree vs. time (corresponding to the design shown in Figure 5.5). The green dots correspond to the experimental travel distances (average of three replicates and error bars are standard deviation of the mean), and the black line to the theoretical model (equation 15). (b) Comparison between the flow rate in the root channel in the bifurcating capillary tree (black line) and in a single channel (red line) based on the theoretical model (equation18). The shading in the figure only applies to the black line and indicates the position of the fluid front within the capillary tree corresponding to the flow rate in the root channel (black line).

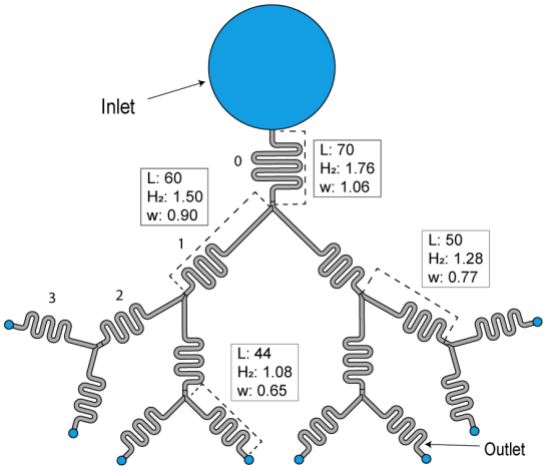

Figure 5.7. View of the capillary tree with homothetically decreasing cross sections. The homothetic ratio is $\alpha = 0.85$. Units in mm, and L is length of the respective channel part in the device.

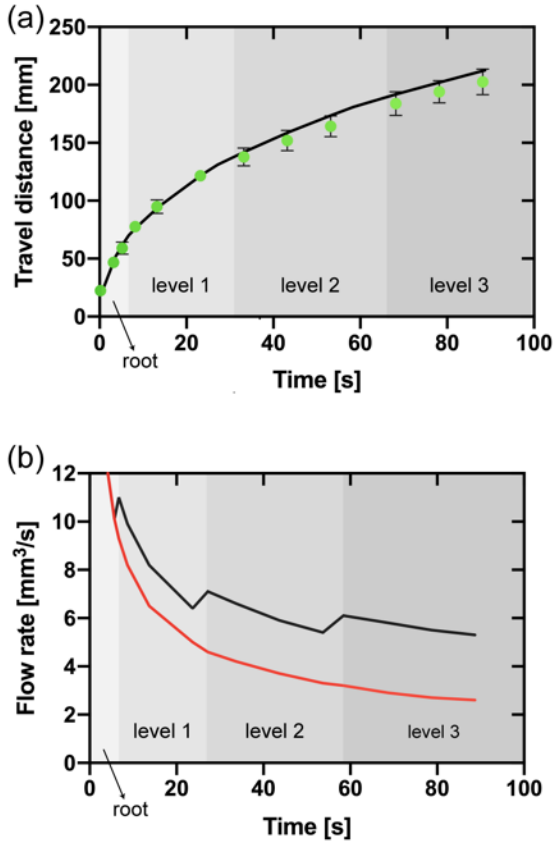

Figure 5.8. (a) Travel distances in the homothetic bifurcating capillary tree vs. time (corresponding to equation 25 and to the design shown in Figure 5.7). The green dots correspond to the experimental travel distances (average of three replicates and error bars are standard deviation of the mean), and the black line to the theoretical model (equation 25). (b) Comparison between the flow rate in the root channel in the homothetic bifurcating capillary tree (black line) and in a single channel (red line) based on the theoretical model (equation 18 modified for 25). The shading in the figure only applies to the black line and indicates the position of the fluid front within the capillary tree corresponding to the flow rate in the root channel (black line). Jumps in the flow rate are due to the crossing of the flow through bifurcations. These jumps are nearly instantaneous, but the time step of the calculation smears somewhat the jumps.

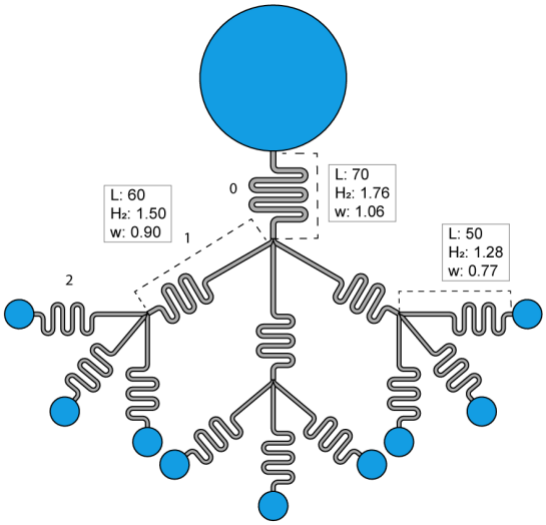

Figure 5.9. Trifurcating capillary tree with homothetically decreasing cross sections. The homothetic ratio is $\alpha = 0.85$. Units in mm, and L is length of the respective channel part in the device (see SI Figure S5 for additional dimensions).

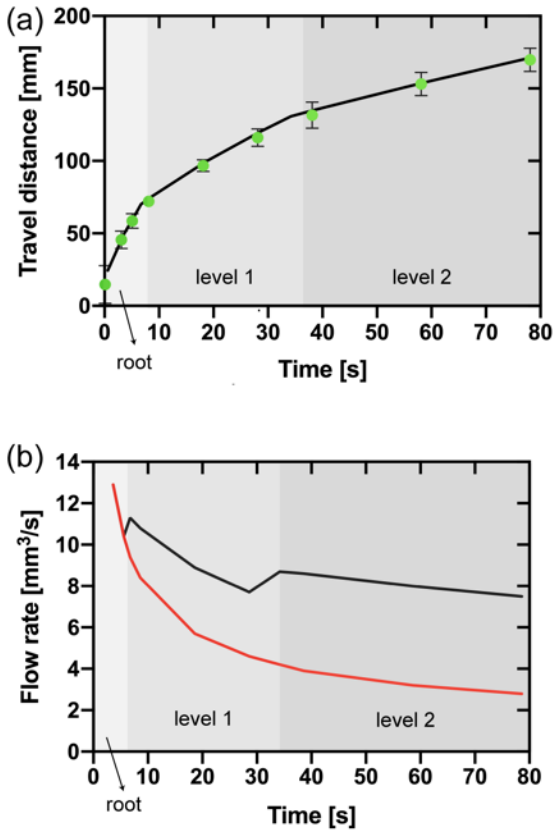

Figure 5.10. (a) Travel distances in the homothetic trifurcating capillary tree vs. time (corresponding to equation 27 and to the design shown in Figure 5.9). The green dots correspond to the experimental travel distances (average of three replicates and error bars are standard deviation of the mean), and the black line to the theoretical model (equation 27). (b) Comparison between the flow rate in the root channel in the homothetic trifurcating capillary tree (black line)

and in a single channel (red line) based on the theoretical model (equation 18 modified for 27). The shading in the figure only applies to the black line and indicates the position of the fluid front within the capillary tree corresponding to the flow rate in the root channel (black line). Jumps in the flow rate are due to the crossing of the flow through bifurcations. These jumps are nearly instantaneous, but the time step of the calculation smears somewhat the jumps.

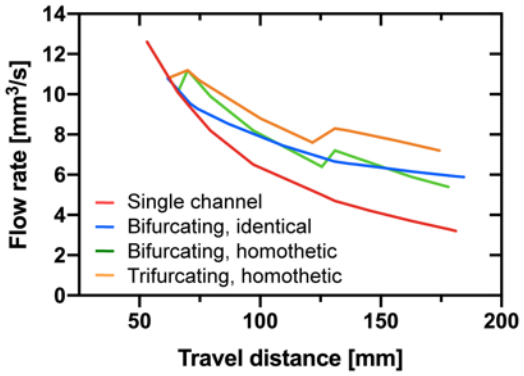

Figure 5.11. Comparison of the flow rates in the capillary trees:
Flow rates vs. travel distance. The largest flow rates are associated to the trifurcating devices with decreasing cross sections. Flow rates are calculated with LWR equation (single channel), equation 18 (bifurcating, identical), equation 25 (bifurcating, homothetic), and equation 27 (trifurcating, homothetic).

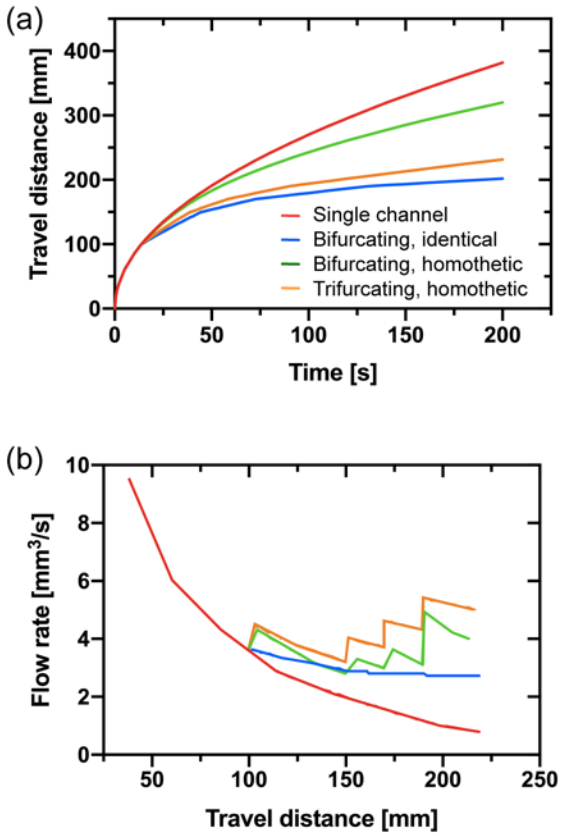

Figure 5.12. Case #1. The case of the single channel (red line) is compared to that of the bifurcating and trifurcating capillary trees. "Identical" refers to a capillary tree of uniform cross sections, while "homothetic" refers to a capillary tree with homothetically decreasing cross sections. (a) Travel distance in the successive channels (with the homothetic ratio 0.8) as a function of time calculated using equations (25) and (27). (b) Flow rate vs. travel distance.

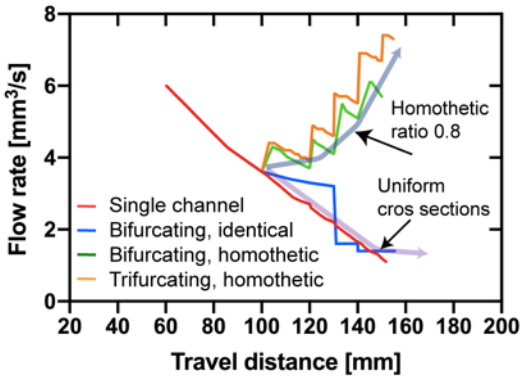

Figure 5.13. Case #2. The case of the single channel (red line) is compared to that of the bifurcating and trifurcating capillary trees. The flow rate increases when the channel cross sections are homothetically reduced (green and orange line), resulting in a pumping effect.

5.8 TABLES

Table 5.1. Characteristic dimensions of the channels

	Level 0	Level 1	Level 2	Level 3
Width [mm]	1.06	0.90	0.77	0.65
Depth [mm]	1.76	1.50	1.28	1.08
Wetted perimeter [mm]	4.13	3.51	3.00	2.53
Friction length [µm]	259	220	187	159
Cross sectional area [mm^2]	1.75	1.26	0.92	0.66

Table 5.2. Physical properties of nonanol (in the PMMA channel) at 20°C.

Physical properties	Value
Viscosity μ	11.2 Pa.s
Surface tension γ	28.5 mN/m
Young contact angle θ	13°
Cassie contact angle θ*	53°
Coefficient C (relation (4))	794 mm^2/s

Table 5.3. Geometrical characteristics of the tree

	Length Case #1 [mm]	Length Case #2 [mm]	Cross section [mm^2]	Friction length [µm]
Root	100	100	1	200
Level #1	50	20	0.8	160
Level #2	20	10	0.64	128
Level #3	20	10	0.51	102.4
Level #4	20	10	0.41	81.9

5.9 REFERENCES

1. Gervais, L.; Hitzbleck, M.; Delamarche, E. Capillary-Driven Multiparametric Microfluidic Chips for One-Step Immunoassays. *Biosens. Bioelectron.* **2011**, *27* (1), 64-70.
2. Safavieh, R.; Juncker, D. Capillarics: Pre-Programmed, Self-Powered Microfluidic Circuits Built from Capillary Elements. *Lab Chip* **2013**, *13*, 4180–4189.
3. Olanrewaju, A.; Beaugrand, M.; Yafia, M.; Juncker, D. Capillary Microfluidics in Microchannels: From Microfluidic Networks to Capillaric Circuits. *Lab on a Chip*. Royal Society of Chemistry August 7, 2018, pp 2323–2347.

4. Juncker, D.; Schmid, H.; Ute, D.; Heiko, W.; Marc, W.; Bruno, M.; Nico, de R.; Emmanuel, D. Autonomous Microfluidic Capillary System. *Anal. Chem.* **2002**, *74*, 6139–6144.
5. Temiz, Y.; Delamarche, E. Sub-Nanoliter, Real-Time Flow Monitoring in Microfluidic Chips Using a Portable Device and Smartphone. *Sci. Rep.* **2018**, *8* (1).
6. Berthier, J.; Brakke, K. A.; Berthier, E. *Open Microfluidics*; Wiley, 2016.
7. Berthier, J.; Theberge, A. B.; Berthier, E. *Open-Channel Microfluidics, IOP Collection*; Morgan & Claypool, 2019.
8. Oliveira, N. M.; Vilabril, S.; Oliveira, M. B.; Reis, R. L.; Mano, J. F. Recent Advances on Open Fluidic Systems for Biomedical Applications: A Review. *Materials Science and Engineering C*. Elsevier Ltd April 1, 2019, pp 851–863.
9. Berthier, E.; Dostie, A. M.; Lee, U. N.; Berthier, J.; Theberge, A. B. Open Microfluidic Capillary Systems. *Analytical Chemistry*. American Chemical Society July 1, 2019, pp 8739–8750.
10. Yu, J.; Berthier, E.; Craig, A.; de Groot, T. E.; Sparks, S.; Ingram, P. N.; Jarrard, D. F.; Huang, W.; Beebe, D. J.; Theberge, A. B. Reconfigurable Open Microfluidics for Studying the Spatiotemporal Dynamics of Paracrine Signalling. *Nat. Biomed. Eng.* **2019**, *3* (10), 830–841.
11. Chen, Y.; Melvin, L. S.; Rodriguez, S.; Bell, D.; Weislogel, M. M. Capillary Driven Flow in Micro Scale Surface Structures. *Microelectron. Eng.* **2009**, *86* (4–6), 1317–1320.
12. Zimmermann, M.; Schmid, H.; Hunziker, P.; Delamarche, E. Capillary Pumps for Autonomous Capillary Systems. *Lab Chip* **2007**, *7* (1), 119–125.
13. Lucas, R. Ueber Das Zeitgesetz Des Kapillaren Aufstiegs von Flüssigkeiten. *Kolloid-Zeitschrift* **1918**, *23*, 15–22. https://doi.org/10.1007/BF01461107.
14. Washburn, E. W. The Dynamics of Capillary Flow. *Phys. Rev.* **1921**, *17* (3), 273–283.
15. Rideal, E. K. On the Flow of Liquids under Capillary Pressure. *Philos. Mag. Ser. 6* **1922**, *44*, 1152–1159.
16. Bosanquet, C. H. On the Flow of Liquids into Capillary Tubes. *Philos. Mag. Ser. 6* **1923**, *45*, 525–531.
17. Rye, R. R.; Yost, F. G.; Mann, J. A. Wetting Kinetics in Surface Capillary Grooves. *Langmuir* **1996**, *12*, 4625–4627.
18. Yost, F. G.; Rye, R. R.; Mann, J. A. Solder Wetting Kinetics in Narrow V-Grooves. *Acta Mater.* **1997**, *45*, 5337–5345.
19. Romero, L. A.; Yost, F. G. Flow in an Open Channel Capillary. *J. Fluid Mech.* **1996**, *322*, 109–129.
20. Kitron-Belinkov, M.; Marmur, A.; Trabold, T.; Dadheech, G. V. Groovy Drops: Effect of Groove Curvature on Spontaneous Capillary Flow. *Langmuir* **2007**, *23*, 8406–8410.
21. Conrath, M.; Canfield, P. J.; Bronowicki, P. M.; Dreyer, M. E.; Weislogel, M. M.; Grah, A. Capillary Channel Flow Experiments Aboard the International Space Station. *Phys. Rev. E* **2013**, *88*, 063009.
22. Weislogel, M. M.; Chen, Y.; Bolleddula, D. A Better Nondimensionalization Scheme for Slender Laminar Flows: The Laplacian Operator Scaling Method. *Phys. Fluids* **2008**, *20*, 93602.
23. Yang, D.; Krasowska, M.; Priest, C.; Popescu, M. N.; Ralston, J. Dynamics of Capillary-Driven Flow in Open Microchannels. *J. Phys. Chem. C* **2011**, *115*, 18761–18769.
24. Ouali, F. F.; McHale, G.; Javed, H.; Trabi, C.; Shirtcliffe, N. J.; Newton, M. I. Wetting

Considerations in Capillary Rise and Imbibition in Closed Square Tubes and Open Rectangular Cross-Section Channels. *Microfluid. Nanofluidics* **2013**, *15* (3), 309–326.
25. Baret, J.-C.; Decré, M. M. J.; Herminghaus, S.; Seemann, R. Transport Dynamics in Open Microfluidic Grooves. *Langmuir* **2007**, *23*, 5200–5204.
26. Berthier, J.; Brakke, K. A.; Furlani, E. P.; Karampelas, I. H.; Poher, V.; Gosselin, D.; Cubizolles, M.; Pouteau, P. Whole Blood Spontaneous Capillary Flow in Narrow V-Groove Microchannels. *Sensors Actuators, B Chem.* **2015**, *206*, 258–267.
27. Lade, R. K.; Hippchen, E. J.; Macosko, C. W.; Francis, L. F. Dynamics of Capillary-Driven Flow in 3D Printed Open Microchannels. *Langmuir* **2017**, *33* (12), 2949–2964.
28. Berthier, J.; Brakke, K. A.; Berthier, E. A General Condition for Spontaneous Capillary Flow in Uniform Cross-Section Microchannels. *Microfluid. Nanofluidics* **2014**, *16*, 779–785.
29. Elizalde, E.; Urteaga, R.; Berli, C. L. A. Rational Design of Capillary-Driven Flows for Paper-Based Microfluidics. *Lab Chip* **2015**, *15* (10), 2173–2180.
30. Tsai, Y. F.; Shieh, C. J.; Yang, H. Capillary Force Pumping Fluid for Glucose Oxidase Enzymatic Fuel Cells. *Microsyst. Technol.* **2017**, *23* (9), 3927–3935.
31. Liu, H.; Zhang, X.; Hong, Z.; Pu, Z.; Yao, Q.; Shi, J.; Yang, G.; Mi, B.; Yang, B.; Liu, X.; Jiang, H.; Hu, X. A Bioinspired Capillary-Driven Pump for Solar Vapor Generation. *Nano Energy* **2017**, *42*, 115–121.
32. Shou, D.; Ye, L.; Fan, J. Treelike Networks Accelerating Capillary Flow. *Phys. Rev. E - Stat. Nonlinear, Soft Matter Phys.* **2014**, *89* (5), 053007.
33. Berthier, J.; Brakke, K. A.; Gosselin, D.; Navarro, F.; Belgacem, N.; Chaussy, D. Spontaneous Capillary Flow in Curved, Open Microchannels. *Microfluid. Nanofluidics* **2016**, *20* (7), 1–9.
34. COMSOL Multiphysics® Modeling Software https://www.comsol.com/ (accessed Aug 28, 2018).
35. Lee, J. J.; Berthier, J.; Theberge, A. B.; Berthier, E. Capillary Flow in Open Microgrooves: Bifurcations and Networks. *Langmuir* **2019**, *35* (32), 10667–10675.
36. Mohammad, A. A.; Alkhaldi, K. H. A. E.; AlTuwaim, M. S.; Al-Jimaz, A. S. Effect of Temperature and Chain Length on the Viscosity and Surface Tension of Binary Systems of N,N-Dimethylformamide with 1-Octanol, 1-Nonanol and 1-Decanol. *J. Chem. Thermodyn.* **2014**, *74*, 7–15. https://doi.org/10.1016/J.JCT.2014.03.022.
37. Kim, S.; Thiessen, P. A.; Bolton, E. E.; Chen, J.; Fu, G.; Gindulyte, A.; Han, L.; He, J.; He, S.; Shoemaker, B. A.; Wang, J.; Yu, B.; Zhang, J.; Bryant, S. H. PubChem Substance and Compound Databases. *Nucleic Acids Res.* **2016**, *44*.
38. Mehrabian, H.; Gao, P.; Feng, J. J. Wicking Flow through Microchannels. *Phys. Fluids* **2011**, *23* (12), 122108.
39. Erickson, D.; Li, D.; Park, C. B. Numerical Simulations of Capillary-Driven Flows in Nonuniform Cross-Sectional Capillaries. *J. Colloid Interface Sci.* **2002**, *250* (2), 422–430.
40. Berthier, J.; Gosselin, D.; Pham, A.; Delapierre, G.; Belgacem, N.; Chaussy, D. Capillary Flow Resistors: Local and Global Resistors. *Langmuir* **2016**, *32* (3), 915–921.
41. Berthier, J.; Gosselin, D.; Pham, A.; Boizot, F.; Delapierre, G.; Belgacem, N.; Chaussy, D. Spontaneous Capillary Flows in Piecewise Varying Cross Section Microchannels. *Sensors Actuators, B Chem.* **2016**, *223*, 868–877.

Chapter 6. SUMMARY AND FUTURE WORK

In conclusion, this dissertation covers the fundamentals of open microfluidics focusing new platforms, theory, design, fabrication, and experimental setups. The overarching goal of the projects was to further develop open channel systems, manipulation methods, and capillary pump designs to maintain capillary flow in an open system.

In chapter 2, we showed for the first time the behavior of two immiscible phases in an open channel platform. We showed that droplets can be simply created by pipetting liquids in the channel while an immiscible phase flows based on passive capillary forces. The channels were easy to fabricate in one step by milling, and the setup is minimal requiring only a pipette for fluid actuation. For larger quantities of devices, channels can be fabricated by injection molding.

In chapter 3, we showed examples of manipulation methods that can be created in an open system such as droplet transportation, incubation, and splitting. All the manipulation methods can be incorporated on one chip. We also showed an example of multiplexing by placing multiple devices in parallel with each other and showed an example of a chemical reaction in open droplet-based microfluidics.

In chapter 4, we derived an expression to calculate the velocity of the fluid in an open channel with a rounded cross section. We also investigated capillary flow in the case of bifurcations and networks.

In chapter 5, we demonstrated the ability of maintaining a constant flow rate or increasing the flow rate in the open channel by adding a capillary pump at the end of the channel. We showed designs of a bifurcation and trifurcation capillary system.

For future directions, a more efficient capillary pump could be developed by using paper as a pump in addition to the bifurcations/trifurcations presented in Chapter 5. Paper has high

wicking power compared to plastic channels and is widely used in microfluidic systems. A hybrid pump consisting of capillary tree like channels with paper pads could produce even higher velocities in an open system for a longer duration of time without the limitation of fabrication or adding a larger platform structure to the overall channel design. Further, given the promising work of an open channel capillary pump presented in this dissertation, the pump can be integrated in later channel manipulation designs to alleviate other challenges such as a longer duration of fluid flow in the channel. Another open channel design that can be incorporated is a droplet generator to create multiple droplets on a chip without using multiple pipetting steps as shown in Chapter 2 and 3. In summary, this dissertation establishes the foundation for several areas of exciting future work. We anticipate broad applications in chemical synthesis, analysis, and biological experiments using the open microfluidic tools described in this dissertation.

BIBLIOGRAPHY

3M TM Fluorinert TM Electronic Liquid FC-40 Electrical Properties; 2010.

Abate, A. R.; Hung, T.; Mary, P.; Agresti, J. J.; Weitz, D. A. High-Throughput Injection with Microfluidics Using Picoinjectors. Proc. Natl. Acad. Sci. U. S. A. 2010, 107, 19163–19166.

Adnani, N.; Vazquez-Rivera, E.; Adibhatla, S.N.; Ellis, G.A.; Braun, D.R.; Bugni, T.S. Investigation of interspecies interactions with marine micro mono sporaceae using an improved co-culture approach. Mar. Drugs, 2015, 13, 6082-6098.

Baret, J.-C.; Decré, M. M. J.; Herminghaus, S.; Seemann, R. Transport Dynamics in Open Microfluidic Grooves. Langmuir 2007, 23, 5200–5204.

Barkal, L. J.; Theberge, A. B.; Guo, C.-J.; Spraker, J.; Rappert, L.; Berthier, J.; Brakke, K. A.; Wang, C. C. C.; Beebe, D. J.; Keller, N. P.; et al. Microbial Metabolomics in Open Microscale Platforms. Nat. Commun. 2016, 7, 10610.

Berry, S. B.; Lee, J. J.; Berthier, J.; Berthier, E.; Theberge, A. B. Open Channel Droplet-Based Microfluidics. bioRxiv 2019, 436675.

Berry, S. B.; Lee, J. J.; Jean, B.; Berthier, E.; Theberge, A. B. Open Channel Droplet-Based Microfluidics. In MicroTas International Conference; MicroTas International Conference: Taiwan, 2018.

Berthier, E.; Beebe, D. J. Flow Rate Analysis of a Surface Tension Driven Passive Micropump. Lab Chip 2007, 7, 1475–1478.

Berthier, J; Brakke, K.A.; Gosselin, D.; Navarro, F.; Belgacem, N.; Chaussy, D.; Berthier, E. On the halt of spontaneous capillary flows in diverging open channels. Med. Eng. Phys. 2017, 75-80.

Berthier, J.; A. Brakke, K.; Gosselin, D.; Huet, M.; Berthier, E. Metastable Capillary Filaments in Rectangular Cross-Section Open Microchannels. AIMS Biophys. 2014, 1, 31–48.

Berthier, J.; Brakke, K. A. The Physics of Microdroplets; John Wiley & Sons, Inc.: Hoboken, NJ, USA, 2012.

Berthier, J.; Brakke, K. A.; Berthier, E. A General Condition for Spontaneous Capillary Flow in Uniform Cross-Section Microchannels. Microfluid. Nanofluidics 2014, 16, 779–785.

Berthier, J.; Brakke, K. A.; Berthier, E. Open Microfluidics; John Wiley & Sons, Inc.: Hoboken, NJ, USA, 2016.

Berthier, J.; Brakke, K. A.; Furlani, E. P.; Karampelas, I. H.; Poher, V.; Gosselin, D.; Cubizolles, M.; Pouteau, P. Whole Blood Spontaneous Capillary Flow in Narrow V-Groove Microchannels. Sensors Actuators, B Chem. 2015, 206, 258–267.

Berthier, J.; Brakke, K. A.; Gosselin, D.; Berthier, E.; Navarro, F. Thread-Based Microfluidics: Flow Patterns in Homogeneous and Heterogeneous Microfiber Bundles. Med. Eng. Phys. 2017, 48, 55–61.

Berthier, J.; Brakke, K. A.; Gosselin, D.; Bourdat, A.-G.; Nonglaton, G.; Villard, N.; Laffite, G.; Boizot, F.; Costa, G.; Delapierre, G. Suspended Microflows between Vertical Parallel Walls. Microfluid. Nanofluidics 2015, 18, 919–929.

Berthier, J.; Brakke, K. A.; Gosselin, D.; Navarro, F.; Belgacem, N.; Chaussy, D. Spontaneous Capillary Flow in Curved, Open Microchannels. Microfluid. Nanofluidics 2016, 20 (7), 1–9.

Berthier, J.; Gosselin, D.; Berthier, E. A Generalization of the Lucas–Washburn–Rideal Law to Composite Microchannels of Arbitrary Cross Section. Microfluid. Nanofluidics 2015, 19, 497–507.

Berthier, J.; Gosselin, D.; Pham, A.; Delapierre, G.; Belgacem, N.; Chaussy, D. Capillary Flow Resistors: Local and Global Resistors. Langmuir 2016, 32 (3), 915–921.

Bosanquet, C. H. On the Flow of Liquids into Capillary Tubes. Philos. Mag. Ser. 6 1923, 45, 525–531.

Boukellal, H.;Selimovic, S.; Jia, Y.; Cristobal, G.; Fraden, S. Simple, robust storage of drops and fluids in a microfluidic device. Lab Chip, 2009, 9, 331-338.

Brackbill, J.; Kothe, D.; Zemach, C. A Continuum Method for Modeling Surface Tension. J. Comput. Phys. 1992, 100 (2), 335–354.

Brakke, K. A. The Surface Evolver. Exp. Math. 1992, 1, 141–165.

Casavant, B. P.; Berthier, E.; Theberge, A. B.; Berthier, J.; Montanez-Sauri, S. I.; Bischel, L. L.; Brakke, K.; Hedman, C. J.; Bushman, W.; Keller, N. P.; et al. Suspended Microfluidics. Proc. Natl. Acad. Sci. U. S. A. 2013, 110, 10111–10116.

Chabert, M.; Dorfman, K. D.; Viovy, J.-L. Droplet Fusion by Alternating Current (AC) Field Electrocoalescence in Microchannels. Electrophoresis 2005, 26, 3706–3715.

Chen, Y.F.; Tseng, F.G.; Chein, S.Y.C.; Chen, M.H.; Yu, R.J.; Chieng, C.C. Surface tension driven flow for open microchannels with different turning angles. Microfluid Nanofluid, 2008, 5, 193-203.

Choi, K.; Ng, A.H.C.; Fobel, R.; Wheeler, A.R. Digital Microfluidics. Annu. Rev. Anal. Chem., 2012, 5, 413-440.

Concus, P.; Finn, R. Capillary Surfaces in a Wedge-Differing Contact Angles. Microgravity Sci. Technol. 1994, 7, 152–155.

Concus, P.; Finn, R. On the Behavior of a Capillary Surface in a Wedge. Proc. Natl. Acad. Sci. U. S. A. 1969, 63, 292–299.

Conrath, M.; Canfield, P. J.; Bronowicki, P. M.; Dreyer, M. E.; Weislogel, M. M.; Grah, A. Capillary Channel Flow Experiments Aboard the International Space Station. Phys. Rev. E 2013, 88, 63009.

de Groot, T.E.; Veserat, K.S.; Berthier, E.; Beebe, D.J.; Theberge, A.B. Surface-tension drive open microfluidic platform for hanging droplet culture. Lab Chip, 2016, 16, 334.

Demirci, U. Acoustic Picoliter Droplets for Emerging Applications in Semiconductor Industry and Biotechnology. Journal of Microelectromechanical Systems, 2006, 15, 4, 957-966.

Elizalde, E.; Urteaga, R.; Berli, C. L. A. Rational Design of Capillary-Driven Flows for Paper-Based Microfluidics. Lab Chip 2015, 15 (10), 2173–2180.

Fidalgo, L.M.; Abell, C.; Huck, W.T.S. Surface-induced droplet fusión in microfluidic devices. Lab Chip, 2007, 7, 984-986.

Freitas, A.; Quina, F.; Carroll, F. Estimation of Water-Organic Interfacial Tensions. A Linear Free Energy Relationship Analysis of Interfacial Adhesion. J. Phys. Chem. B 1997, 5647, 7488–7493.

Frenz, L.; Blank, K.; Brouzes, E.; Griffiths, A.D. Reliable microfluidic on-chip incubation of droplets in delay-lines. Lab Chip, 2009, 9, 10, 1344-1348.

Gervais, L.; de Rooij, N.; Delamarche, E. Microfluidic Chips for Point-of-Care Immunodiagnostics. Adv. Mater. 2011, 23, H151–H176.

Gervais, L.; Delamarche, E. Toward One-Step Point-of-Care Immunodiagnostics Using Capillary-Driven Microfluidics and PDMS Substrates. Lab Chip 2009, 9, 3330–3337.

Gervais, L.; Hitzbleck, M.; Delamarche, E. Capillary-Driven Multiparametric Microfluidic Chips for One-Step Immunoassays. Biosens. Bioelectron. 2011, 27 (1), 64–70.

Guckenberger, D.J.; de Groot, T.E.; Wan, A.M.D.; Beebe, D.J.; Young, E.W.K. Micromilling: A method for ultra-rapid prototyping of plastic microfluidic devices. Lab Chip, 2015, 15, 11, 2364-2378.

Hadimioglu, B.; Stearns, R.; Ellson, R. Moving Liquids with Sound: The Physics of Acoustic Droplet Ejection for Robust Laboratory Automation in Life Sciences. Journal of Laboratory Automation, 2016, 21, 1, 4-18.

Han, Y.; Shikazono, N. Measurement of the Liquid Film Thickness in Micro Tube Slug Flow. Int. J. Heat Fluid Flow 2009, 30, 842–853.

Huemmer, D.; Bachler, S.; Kohler, M.; Blank, L.M.; Zenobi, R.; Dittrich, P.S.; Microfluidic platform for multimodal analysis of enzyme secretion in nanoliter droplet arrays. Anal. Chem., 2018.

Jones, T.B. On the relationship of dielectrophoresis and electrowetting. Langmuir, 2002, 18, 11, 4437-4443.

Juncker, D.; Schmid, H.; Ute, D.; Heiko, W.; Marc, W.; Bruno, M.; Nico, de R.; Emmanuel, D. Autonomous Microfluidic Capillary System. Anal. Chem. 2002, 74, 6139–6144.

Kim, S.; Thiessen, P. A.; Bolton, E. E.; Chen, J.; Fu, G.; Gindulyte, A.; Han, L.; He, J.; He, S.; Shoemaker, B. A.; et al. PubChem Substance and Compound Databases. Nucleic Acids Res. 2016, 44.

Kitron-Belinkov, M.; Marmur, A.; Trabold, T.; Dadheech, G. V. Groovy Drops: Effect of Groove Curvature on Spontaneous Capillary Flow. Langmuir 2007, 23, 8406–8410.

Kolliopoulos, P.; Jochem, K. S.; Lade, R. K.; Francis, L. F.; Kumar, S. Capillary Flow with Evaporation in Open Rectangular Microchannels. Langmuir 2019, 35 (24), 8131–814

Lade Jr., R.K.; Jochem, K.S.; Macosko, C.W.; Francis, L.F. Capillary Coatings: Flow and Drying Dynamics in Open Microchannels. Langmuir, 2018, 34, 7624-7639.

Lee, J. J.; Berthier, J.; Brakke, K. A.; Dostie, A. M.; Theberge, A. B.; Berthier, E. Droplet Behavior in Open Biphasic Microfluidics. Langmuir 2018, 34 (18), 5358–5366.

Lee, U.N.; Su, X.; Guckenberger, D.J., Dostie, A.M.; Zhang, T.; Berthier, E.; et al. Fundamentals of rapid injection molding for microfluidic cell-based assays. Lab Chip, 2018, 18, 496-504.

Lee, Y.; Choi, J.W.; Yu, J.; Park, D.; Ha, J.; Son, K.; et al. Microfluidics within a well: an injection-molded plastic array 3D culture platform. Lab Chip, 2018, Advance Article.

Li, C.; Boban, M.; Tuteja, A. Open-Channel, Water-in-Oil Emulsification in Paper-Based Microfluidic Devices. Lab Chip 2017, 17, 1436–1441.

Link, D.R.; Anna, S.L.; Weitz, D.A; Stone, H.A. Geometrically mediated breakup of drops in microfluidic device. Phys. Rev. Lett., 2004, 92, 054503.

Lucas, R. Ueber Das Zeitgesetz Des Kapillaren Aufstiegs von Flüssigkeiten. Kolloid-Zeitschrift 1918, 23, 15–22.

Mann, J. A.; Romero, L.; Rye, R. R.; Yost, F. G. Flow of Simple Liquids down Narrow V Grooves. Phys. Rev. E 1995, 52, 3967–3972.

Mazutis, L.; Griffiths, A. D. Selective Droplet Coalescence Using Microfluidic Systems. Lab Chip 2012, 12, 1800–1806.

Mehrabian, H.; Gao, P.; J.J. Feng, J.J. Wicking flow through microchannels. Physics of Fluids, 2011, 23, 122108.

Mohammad, A. A.; Alkhaldi, K. H. A. E.; AlTuwaim, M. S.; Al-Jimaz, A. S. Effect of Temperature and Chain Length on the Viscosity and Surface Tension of Binary Systems of N,N-Dimethylformamide with 1-Octanol, 1-Nonanol and 1-Decanol. J. Chem. Thermodyn. 2014, 74, 7–15.

Ng, A.H.C.; Li, B.B.; Chamberlain, M.D.; Wheeler, A.R. Digital Microfluidic Cell Culture. Annu. Rev. Biomed. Eng., 2015, 17, 91-112.

Nilghaz, A.; Ballerini, D. R.; Guan, L.; Li, L.; Shen, W. Red Blood Cell Transport Mechanisms in Polyester Thread-Based Blood Typing Devices. Anal. Bioanal. Chem. 2016, 408, 1365–1371.

Nilghaz, A.; Ballerini, D. R.; Shen, W. Exploration of Microfluidic Devices Based on Multi-Filament Threads and Textiles: A Review. Biomicrofluidics 2013, 7, 51501.

Onaka, H.; Mori, Y.; Igarashi, Y.; Furumai, T. Mycolic acid-containing bacteria induce natural-product biosynthesis in Streptomyces species. Appl. Environ. Microbiol., 2011, 77, 2 400-406.

Ouali, F. F.; McHale, G.; Javed, H.; Trabi, C.; Shirtcliffe, N. J.; Newton, M. I. Wetting Considerations in Capillary Rise and Imbibition in Closed Square Tubes and Open Rectangular Cross-Section Channels. Microfluid. Nanofluidics 2013, 15, 309–326.

Quéré, D. Inertial Capillarity. Europhys. Lett. 1997, 39, 533–538.

Reches, M.; Mirica, K. A.; Dasgupta, R.; Dickey, M. D.; Butte, M. J.; Whitesides, G. M. Thread as a Matrix for Biomedical Assays. ACS Appl. Mater. Interfaces 2010, 2, 1722–1728.

Rideal, E. K. On the Flow of Liquids under Capillary Pressure. Philos. Mag. Ser. 6 1922, 44, 1152–1159.

Romero, L. A.; Yost, F. G. Flow in an Open Channel Capillary. J. Fluid Mech. 1996, 322, 109–129.

Rye, R. R.; Yost, F. G.; Mann, J. A. Wetting Kinetics in Surface Capillary Grooves. Langmuir 1996, 12, 4625–4627.

Safavieh, R.; Juncker, D. Capillarics: Pre-Programmed, Self-Powered Microfluidic Circuits Built from Capillary Elements. Lab Chip 2013, 13, 4180–4189.

Schneider, T.; Kreutz, J.; Chiu, D. T. The Potential Impact of Droplet Microfluidics in Biology. Anal. Chem. 2013, 85 (7), 3476–3482.

Shang, L.; Cheng, Y.; Zhao, Y. Emerging Droplet Microfluidics. Chem. Rev., 2017, 117, 7964-8040.

Song, H.; Chen, D.L.; Ismagilov, R.F. Reactions in droplets in microfluidic channels. Angew. Chem. Int. Ed. Engl., 2006, 45, 44, 7336-7356.

Teh, S.Y.; Lin, R.; Hung, L.H.; Lee, A.P. Droplet microfluidics. Lab Chip, 2008, 8, 198-220.

Trejo-Soto, C.; Costa-Miracle, E.; Rodriguez-Villarreal, I.; Cid, J.; Alarcón, T.; Hernández - Machado, A. Capillary Filling at the Microscale: Control of Fluid Front Using Geometry. PLoS One 2016, 11 (4), e0153559.

Tsai, Y. F.; Shieh, C. J.; Yang, H. Capillary Force Pumping Fluid for Glucose Oxidase Enzymatic Fuel Cells. Microsyst. Technol. 2017, 23 (9), 3927–3935.

Walker, G. M.; Beebe, D. J. A Passive Pumping Method for Microfluidic Devices. Lab Chip 2002, 2, 131–134.

Washburn, E. W. The Dynamics of Capillary Flow. Phys. Rev. 1921, 17 (3), 273–283.

Weislogel, M. M.; Chen, Y.; Bolleddula, D. A Better Nondimensionalization Scheme for Slender Laminar Flows: The Laplacian Operator Scaling Method. Phys. Fluids 2008, 20, 93602.

Whitesides, G. M. The Origins and the Future of Microfluidics. Nature 2006, 442 (7101), 368–373.

Yager, P.; Edwards, T.; Fu, E.; Helton, K.; Nelson, K.; Tam, M. R.; Weigl, B. H. Microfluidic Diagnostic Technologies for Global Public Health. Nature 2006, 442, 412–418.

Yang, D.; Krasowska, M.; Priest, C.; Popescu, M.N.; Ralston, J. Dynamics of capillary-driven flow in open microchannels. J. Phys. Chem. C., 2011, 115, 18761-18769.

Yang, Y.H.; Song, E.; Lee, B.R.; Kim, E.J.; Park, S.H.; Kim, Y.G.; et al. Rapid functional screening of Streptomyces coelicolor regulators by use of a pH indicator and application to the MarR-like regulator AbsC. Appl. Environ. Microbiol., 2010, 76, 11, 3645-3656.

Yost, F. G.; Rye, R. R.; Mann, J. A. Solder Wetting Kinetics in Narrow V-Grooves. Acta Mater. 1997, 45, 5337–5345.

APPENDIX A

Chapter 2. Droplet Behavior in Open Biphasic Microfluidics

Supporting Information (SI) references

Reproduced in part from Lee, J.J.; Berthier, J*.; Brakke, K.A.; Dostie, A.M.; Berthier, E.; Theberge, A.B. Droplet Behavior in Open Biphasic Microfluidics. Langmuir 2018, 34, 5358−5366.*

**denotes co-authorship. J.J.L contributed to the overall fabrication designs and experimental designs. J.B. developed the analytical model and numerical simulation of this work.*

1. Analytical analysis of the effect of an immiscible plug in a spontaneous capillary flow

Let us consider first a plug contacted by a spontaneous capillary flow (SCF) of an immiscible liquid, which we denote as the primary or carrier liquid. In the present case the carrier liquid is an organic liquid, and the plug is aqueous. This situation is sketched in Figure S1.1A. Figure S1.1B represents the SCF of the primary liquid alone.

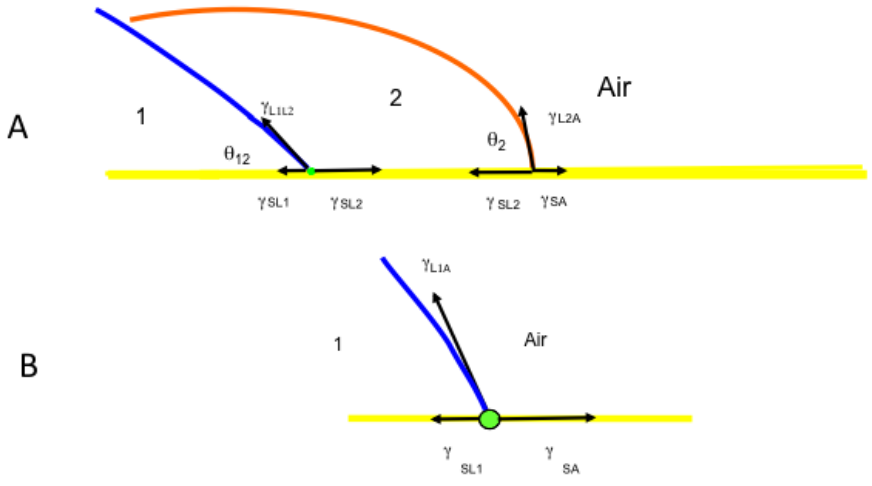

Figure S1.1. Sketch of the capillary forces. Configuration (A): the plug is delimited by the orange line and the carrier liquid is painted in blue. Configuration (B): sketch of the SCF of the primary liquid. The yellow line represents the solid wall. Note that the contact angles are not the same in (A) and (B).

We denote by indices S, A, L1 and L2 respectively the solid wall, air, carrier liquid and plug. In the following we show that the balances of the capillary forces are the same in the two configurations A and B.

Let us analyze the capillary forces on the floor of the channel. The resultant of the capillary forces is the sum of the capillary force at the first and second interfaces (Figure S1.1A)

$$R = \gamma_{L1L2}\cos\theta_{12} + \gamma_{L2A}\cos\theta_2 \quad . \tag{1.1}$$

In the case of static or quasi-static contact angles, the relation between the different contact angles is[1]

$$\gamma_{L1L2}\cos\theta_{12} = \gamma_{L1A}\cos\theta_1 - \gamma_{L2A}\cos\theta_2 \quad . \tag{1.2}$$

Substitution of (1.2) in (1.1) yields

$$R = \gamma_{L1A}\cos\theta_1 \quad , \tag{1.3}$$

which is simply the capillary force for liquid 1 alone (Figure S1.1B). Hence the two-phase configuration (A) is equivalent to the single-phase configuration (B).

This reasoning still applies for a plug embedded in the carrier fluid, as shown in Figure S1.2. In this case, and assuming that the contact angles are static ones, the resultant of the forces in configuration (A) is

$$R = \gamma_{L1L2}\cos\theta_{12} - \gamma_{L1L2}\cos\theta_{12} + \gamma_{L1A}\cos\theta_1 \quad , \tag{1.4}$$

which is the same as the resultant in configuration (B).

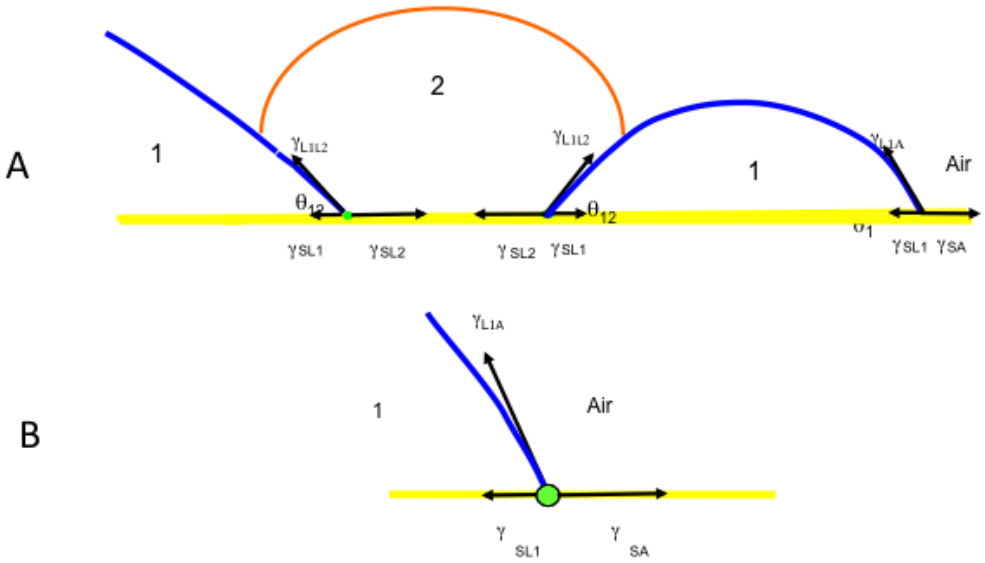

Figure S1.2. Sketch of the capillary forces. Configuration (A): the plug is delimited by the orange line and the carrier liquid is painted in blue. Configuration (B): sketch of the SCF of the primary liquid. The yellow line represents the solid wall.

In conclusion, in the case of a channel of constant cross section, the presence of the plug does not affect the occurrence of the SCF.

2. Numerical simulation of the behavior of an immiscible plug in an SCF flow

The software Surface Evolver[2] has been conventionally used with success to predict SCF conditions.[1,3–5] It is emphasized that Evolver cannot treat the dynamic of the flow, but it iteratively relocates the interface to lower the energy taking into account constraints such as contact angles and liquid weight. In the case of SCF no equilibrium location exists, but we can still use Evolver to predict if the fluid moves and the direction of motion because the onset of SCF is quasi-static. Note that when inertia and viscous forces are negligible in front of surface tension and capillary forces which is often the case in open microfluidic. Evolver results are close to the reality of the flow.[3]

The Evolver data file for this type of problem requires the specification of the different surface tensions (γ_{L1A}, γ_{L2A}, γ_{L1L2}) and the two contact angles θ_1 and θ_2. For this study of the SCF condition with Evolver, many different values of these data have been used. In all cases a two-phase SCF is observed as soon as the main liquid satisfies the SCF condition.

Let us consider the case of a rectangular open groove: Three different flow modes, i.e., three different flow morphologies, have been found: (1) a shift mode where the plug is horizontally displaced and translates in front of the flow; (2) a lift mode where the plug is lifted and the main liquid flows underneath; (3) a bridge mode where the plug sticks to the floor of the channel and the capillary flow of the main liquid flows above. In the following we detail each of these modes.

2.1 Shift mode

A shift mode occurs when the plug is translated down the channel by the action of the carrier fluid. Upon initial contact, the plug shape changes. After the contact, the shape of the plug remains unchanged. Figure S2.1. shows a typical shift mode. This mode occurs principally when the two liquids wet the walls.

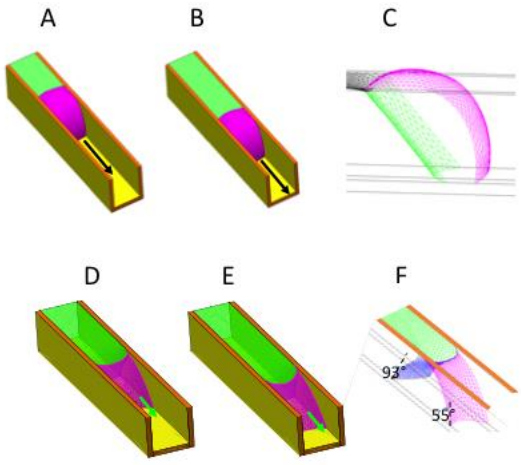

Figure S2.1. Shift mode: A and B, shift motion of the plug upon arrival of the carrier capillary flow; C, detail of the shape of the plug. (γ_{L1A} 20 mN/m, γ_{L2A}= 72 mN/m, γ_{L1L2} = 30 mN/m, θ_1= 50°, θ_2 = 90°). D and E, shift motion of the plug; F, detail of the shape of the plug (γ_{L1A} = 30 mN/m, γ_{L2A} = 42 mN/m, γ_{L1L2} = 16 mN/m, θ_1 = 40°, θ_2 = 55°).

2.2. Lift mode

In the case where the liquid-liquid contact angle θ_{12} is small, the carrier liquid (liquid 1) slips below the plug and progressively lifts the plug. The liquid 1 SCF continues with the plug of liquid 2 on top of it (Figure S2.2).

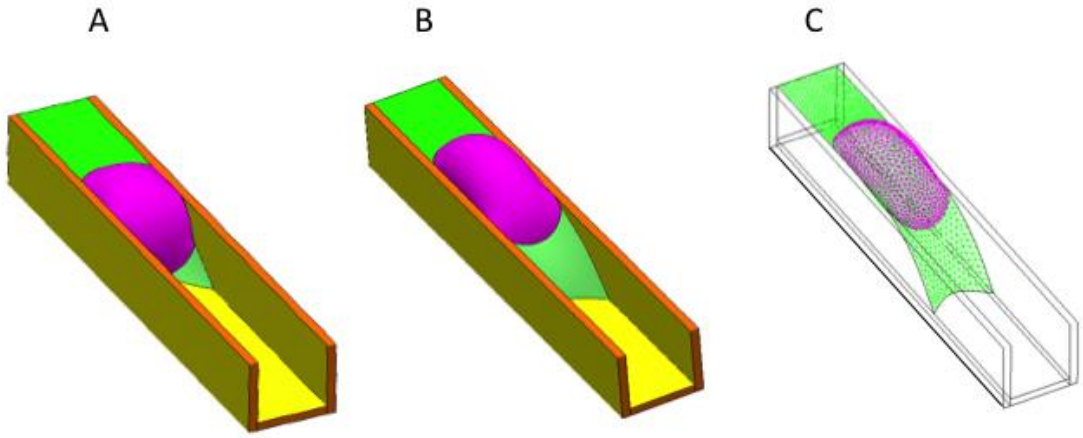

Figure S2.2. Lift mode: A and B, the main liquid uplifts the plug and continues to flow beneath (γ_{L1A} = 72 mN/m, γ_{L2A} = 36 mN/m, γ_{L1L2} = 60 mN/m, θ_1 = 50°, θ_2 = 110°).

2.3. Bridge mode

In the case where the plug has a small contact angle with the walls, and its surface tension is sufficiently high, the plug forms a bridge and the carrier fluid flows above this bridge (Figure S2.3). In the Evolver quasi-static approach, the bridge remains immobile. However, experiments show that the bridge may or may not move depending on the plug-carrier liquid surface tension.

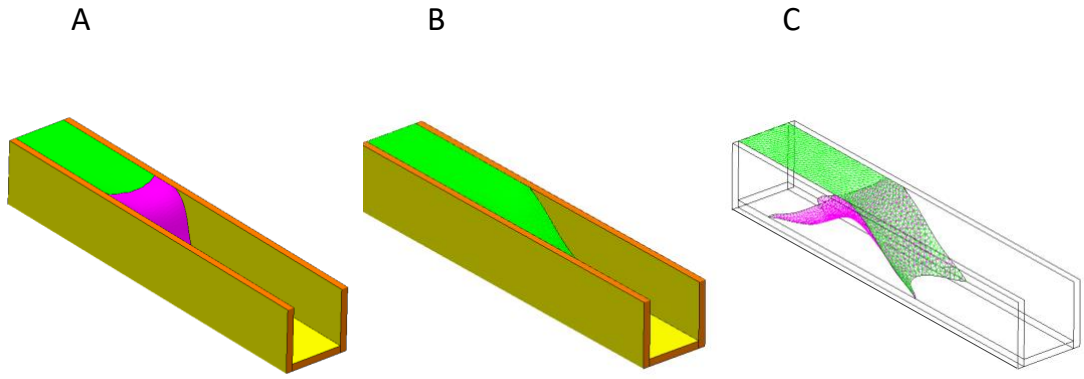

Figure S2.3. Bridge mode: A and B, the primary liquid (γ_{L1A}= 72 mN/m, γ_{L2A} = 36 mN/m, γ_{L1L2}=60 mN/m, θ_1= 50°, θ_2=110°).

Table S2.1. Parameter space tested on surface evolver and resulting mode numerically observed.

Mode	θ_1[a]	θ_2[a]	γ_1	γ_2	$\gamma_{1,2}$	cos (θ_{12})	θ_{12}[a]
Bridge	15	80	22	65	30	0.3	70.6
Bridge	15	80	22	65	30	0.3	70.6
Bridge[b]	15	60	22	65	30	-0.4	112.0
Bridge	15	30	22	65	30	-1.0	180.0
Bridge	15	40	22	65	35	-0.8	144.6
Shift	15	40	22	45	35	-0.4	112.2
Shift	15	30	22	45	35	-0.5	120.4
Shift	10	20	22	45	35	-0.6	126.1
Shift	10	90	22	45	35	0.6	51.8
Shift[c]	30	90	22	55	35	0.5	57.0
Shift	30	90	42	35	55	0.7	48.6
Shift	50	70	42	35	55	0.3	74.1
Shift	50	70	40	35	40	0.3	69.9
Shift	10	80	40	35	40	0.8	33.6
Lift	10	90	45	30	40	1.0	0.0
Lift	10	90	45	20	30	1.0	0.0
Lift[d]	10	80	45	20	30	1.0	0.0
Lift	10	60	45	20	30	1.0	0.0
Shift	10	25	35	50	30	-0.4	111.2
Shift	5	15	35	50	30	-0.4	116.6
Bridge	5	15	35	50	10	-1.0	180.0
Lift	5	15	50	35	10	1.0	0.0

[a] contact angle in units of degrees
[b]Figure 1Bii, [c]Figure 1Aii, [d]Figure 1Cii, respectively

3. Open biphasic flows in poly-methyl-methacrylate (PMMA) channels

In this section we display inserts of top and side view movies that were obtained for a number of solvents contacting an aqueous plug placed in an open microfluidic channel.

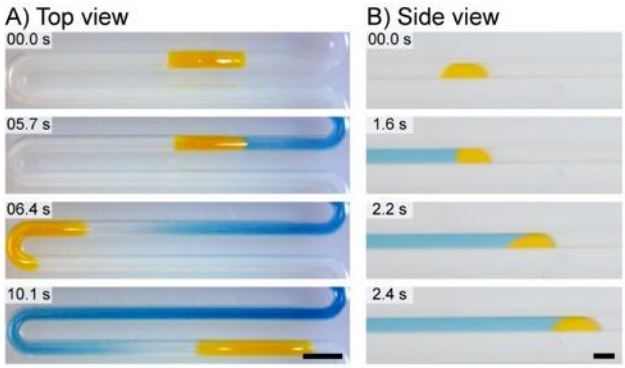

Figure S3.1. Experimental visualization of shift mode using an aqueous plug (yellow) and pentanol as the carrier phase (blue) from the top view (A) and side view (B). The plug advances and stops as it travels down the channel with the carrier fluid. Images are representative of 3 three replicate experiments. The scale bar is 2 mm.

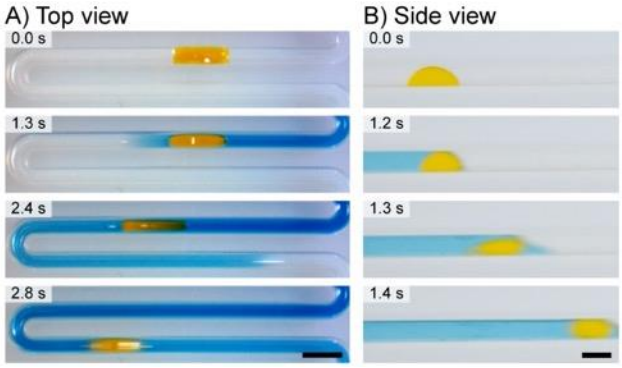

Figure S3.2. Experimental visualization of raft mode using an aqueous plug (yellow) and chloroform as the carrier phase (blue) from the top view (A) and side view (B). Images are representative of 3 three replicate experiments. The scale bar is 2 mm.

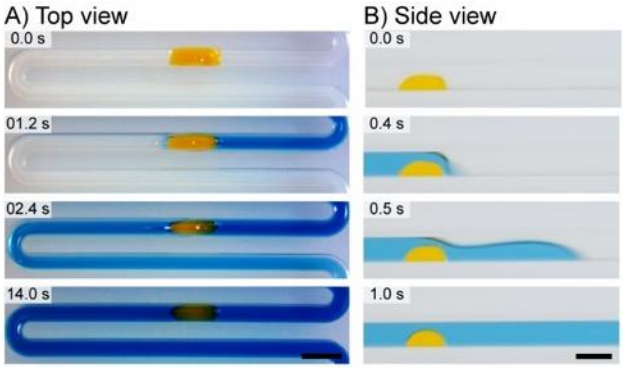

Figure S3.3. Experimental visualization of bridge mode using an aqueous plug (yellow) and toluene as the carrier phase (blue) from the top view (A) and side view (B). Images are representative of 3 three replicate experiments. The scale bar is 2 mm.

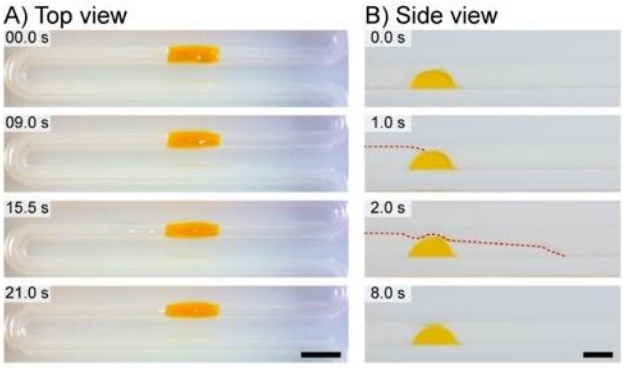

Figure S3.4. FC-40 top view k(A) and side view (B) showing bridge mode. FC-40 is not tinted because it is challenging to find dyes that are soluble in fluorinated oil. Red dotted lines in (B) have been added to visualize the FC-40 fluid front at 1.0 s and 2.0 s. At 8.0 s, the channel is full with FC-40. Images are representative of 3 replicate experiments. The scale bar is 2 mm.

4. Transition between surface-tension dominated and inertial conditions

In this section we display additional inserts of top view movies displaying transitions in behavior as inertial effects are increased.

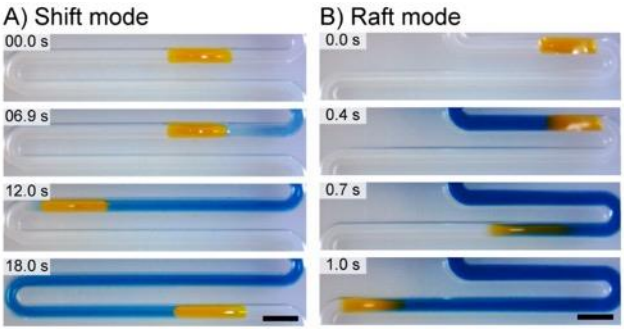

Figure S4.1. Experiment with pentanol as the carrier fluid (blue) and an aqueous plug (yellow) at 2 different locations in the channel. (A) Plug in a low velocity region showing shift mode. (B) Plug at a high velocity region showing raft mode. Images are representative of 3 three replicate experiments, and scale bar is 2 mm.

5. Development of the Weber number for open biphasic flows

Gravitational, inertial, viscous, and surface tension forces are the main forces acting on a plug/drop in a two-phase flow. These forces are associated with three dimensionless numbers: the Bond (or Eötvös) number, the capillary number, and the Weber number.[6] In this section these numbers are expressed for our two-phase capillary flows.

5.1 Bond number

For a droplet or a plug, the Bond number characterizes the ratio between gravitational and surface tension forces.[6] The expression for the Bond number is

$$Bo = \frac{\Delta\rho_{12}\ g\ h^2}{\gamma_{12}}. \qquad (5.1)$$

where $\Delta\rho_{12}$ is the difference of density between carrier liquid and water, g the gravitational constant, h the height of the channel, and γ_{12} the surface tension between carrier liquid and water. The values of the Bond number for the different carrier liquids is indicated in table S5.1.

Table S5.1. Bond numbers (*Bo*) calculated for the channel geometry used in the experiments.

Liquid	Density[a,7] [kg/m^3]	Surface tension[8] w. water [mN/m]	*Bo*	Capillary length [mm]
1-pentanol	814.0	4.4[b]	0.95	1.54
chloroform	1490.0	32.8[a]	0.34	2.59
toluene	867.0	36.1[b]	0.08	5.21
n-dodecane	750.0	52.8[b]	0.11	4.60
FC-40	1850.0[b]	52.0[c,9]	0.37	2.47
1-nonanol	827.0	8.5[b]	0.24	2.24

[a,b,c]at 20°C, 25°C, and 23°C, respectively

All Bond numbers are less than 1, but not necessarily markedly lower than 1 in some cases. Some slight gravity effects might occur, especially in the case of pentanol since its Bond number is close to 1.

Another approach to gravity effects consists in calculating the capillary length *l* defined by

$$l = \sqrt{\frac{\gamma_{12}}{\Delta\rho_{12}\ g}}\ . \qquad (5.2)$$

Gravity effects are negligible when the characteristic dimensions of the channel are small compared to the capillary length ($h \ll l$). The values of *l* are indicated in table S5.1. We observe that this statement is only approximately true. Some gravity effects may be present.

5.2 Capillary number

Let us first derive the capillary number for the carrier fluid alone. From a general standpoint, the capillary number characterizes the ratio between viscous and surface tension forces. The expression for the capillary number is

$$Ca = \frac{V\,\mu}{\gamma}\,, \tag{5.3}$$

where μ is the liquid viscosity, γ, the surface tension, and *V* the average velocity. The average velocity *V* is a function of the time or the travel distance. In the following we replace *V* by its expression using the travel distance *z*.

The travel distance for an open capillary flow as a function of the time is given by the general expression[10,11]

$$z = \sqrt{\frac{\gamma}{\mu}\,2\,\bar{\lambda}\,cos\theta^*}\,\sqrt{t}\,, \tag{5.4}$$

where *t* is the time, $\bar{\lambda}$ the average friction length, and θ* the average Cassie angle.[10]

The average Cassie angle is the average value of the contact angle alongside the contour of a cross section of the channel (Figure S5.1), i.e.

$$\cos\theta^* = \sum_i f_i\,cos\theta_i\,, \tag{5.5}$$

where f_i is the length fraction of each contour *i*: $\sum_i f_i = 1$. In the case of a single contour (closed channel with a unique wall) relation (5.5) reduces to the usual contact angle. A spontaneous capillary flow occurs when $\cos\theta^* > 0$, or $\theta^* \leq 90°$.

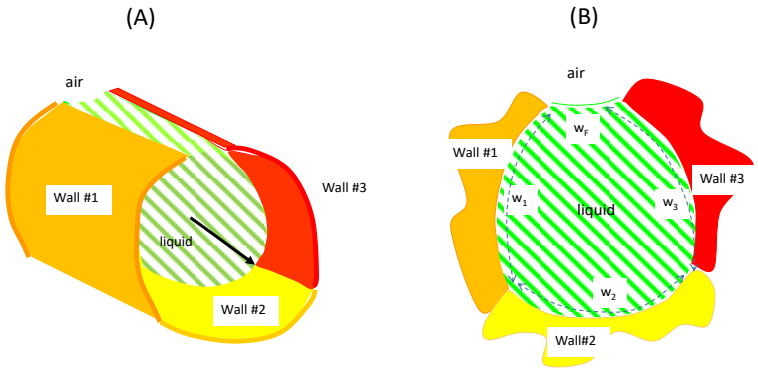

Figure S5.1. Sketch of an open channel with composite walls[11]. In the case of (B), $f_i = \frac{w_i}{w_1+w_2+w_3+w_F}$.

Organic liquids have a hydrophilic contact angle with PMMA walls. Contact angles have been measured using a Kruss device (Kruss GmBH, Germany). These angles are reported in table S5.2.

The average contact angle (Cassie generalized contact angle) can be derived from (5.5) for the rounded U-groove. If *w* denotes the channel width and *h* the vertical channel height, we find

$$\cos\theta^* = \frac{-w+2\,h\,cos\theta+\pi\frac{w}{2}cos\theta}{w+2\,h+\pi\frac{w}{2}}. \qquad (5.6)$$

The generalized Cassie angles are indicated in table S5.2.

Table S5.2. Contact angles with PMMA walls and generalized Cassie angles.

Liquid	Contact angle	cosθ*
1-pentanol	12.5°	0.60
chloroform	17.3°	0.59
toluene	7.8°	0.62
n-dodecane	26.7°	0.54
FC-40	12.7°	0.60
1-nonanol	17.0°	0.60

For a confined channel of arbitrary shape, the average friction length $\bar{\lambda}$ has been demonstrated to be[6]

$$\bar{\lambda} = \frac{8\, D_H}{f\, Re}, \tag{5.8}$$

where D_H is the hydraulic diameter, f the Fanning factor and Re the Reynolds number. In the case of a cylindrical tube, the average friction length is simply $\bar{\lambda} = R/4$, and (5.4) reduces to the Lucas-Washburn-Rideal law.[12–15]

The situation is more complex in the case of open channels. One must approximate the shear rate in a cross section. Depending on the channel geometry, different expressions have been reported in the literature depending on the geometry of the channel (rectangular U-groove, suspended channel, sharp V-groove, etc.).[3,16] Some values of $\bar{\lambda}$ are indicated in Figure S5.2. In our case of a rounded U-groove, a COMSOL calculation has produced the value $\bar{\lambda} = 151\ \mu m$. The value $\bar{\lambda} \sim 151\ \mu m$ is consistent with the values found using the approximation in Figure S5.2. First a suspended channel of width w = 0.8 mm, would have an average friction length $\bar{\lambda} \sim \frac{w}{6} = 133\ \mu m$. Second a rectangular U-groove of depth h=1.1 mm would have an average friction length $\bar{\lambda} \sim \frac{1}{6}\frac{w+2h}{\frac{w}{h}+\frac{2h}{w}} = 143\ \mu m$. Finally, a rectangular U-groove of depth h = 1.1 + 0.4 = 1.5 mm would have an average friction length $\bar{\lambda} \sim \frac{1}{6}\frac{w+2h}{\frac{w}{h}+\frac{2h}{w}} = 148\ \mu m$.

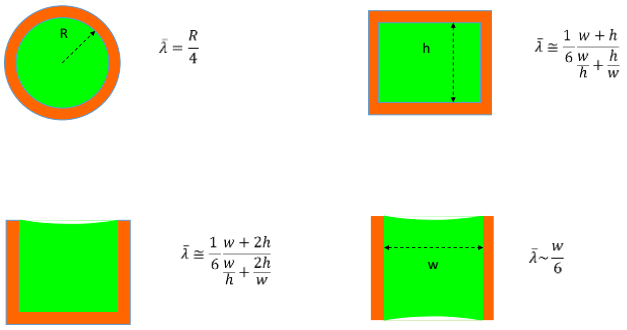

Figure S5.2. Expressions of the average friction length for four different geometries.

Time derivation of (5.4) yields the capillary velocity

$$V = \sqrt{\frac{\gamma}{\mu}\ \frac{\bar{\lambda}}{2} cos\theta^*}\ \frac{1}{\sqrt{t}}\,. \tag{5.9}$$

Eliminating the time between (5.4) and (5.9) yields the relation between the velocity and travel distance

$$V = \frac{\gamma}{\mu}\ \bar{\lambda}\, cos\theta^*\ \frac{1}{z}\ . \tag{5.10}$$

The capillary number is expressed by[17]

$$Ca = \frac{V\,\mu}{\gamma} = \frac{\bar{\lambda}}{z}\ cos\theta^*\ . \tag{5.11}$$

$\bar{\lambda}$ and $cos\theta^*$ being constant, the capillary number is merely a function of the travel distance.

Now consider a two-phase capillary flow. The plug capillary number (two-phase) is the ratio between the viscous force exerted by the carrier fluid and the surface tension of the plug liquid, hence

$$Ca_{12} = \frac{V\,\mu}{\gamma_{12}} = Ca\ \frac{\gamma}{\gamma_{12}} = \left(\frac{\bar{\lambda}}{z}\ cos\theta^*\right)\frac{\gamma}{\gamma_{12}}\,. \tag{5.12}$$

In conclusion, at a given location in the channel, for a given travel distance, the ratio γ/γ_{12} characterizes the difference between the liquids. This ratio is indicated in Table S5.3 for the six liquids.

Table S5.3. Ratio γ/γ_{12} and capillary numbers for the different liquids at distances $100\bar{\lambda}$

Liquid	Surface tension w. air[a,7] (γ) [mN/m]	Surface tension w. water[8] (γ_{12}) [mN/m]	γ/γ_{12}	Ca_{12} Distance z= $100\bar{\lambda}$	Ca_{12} Distance z= $1000\bar{\lambda}$
1-pentanol	26.00	4.4[b]	5.9	3.72×10^{-2}	3.72×10^{-3}
chloroform	26.70	32.8[a]	0.8	5.13×10^{-3}	5.13×10^{-4}
toluene	28.40	36.1[b]	0.8	4.96×10^{-3}	4.96×10^{-4}
n-dodecane	25.30	52.8[b]	0.5	3.02×10^{-3}	3.02×10^{-4}
FC-40	16.00[18]	52.0[c,9]	0.3	1.94×10^{-3}	1.94×10^{-4}
1-nonanol	28.00[b]	8.5[b]	3.3	1.94×10^{-2}	1.94×10^{-3}

[a,b,c]at 20°C, 25°C, and 23°C, respectively

The capillary numbers are small even at the channel entrance. Note that for chloroform and toluene, the plug capillary number is nearly identical to the carrier liquid capillary number. When the ratio γ/γ_{12} is small (as is the case of n-dodecane and FC-40), the plug/carrier surface tension dominates the carrier/air surface tension, and the plug wants to occupy the largest width possible. The entrainment of the plug by the carrier flow has been found impossible in the case of n-dodecane and FC-40.

5.3 Weber number

From a general standpoint, the Weber number characterizes the ratio between inertial and surface tension forces

$$We = \frac{\rho V^2}{\gamma/w} = \frac{\rho V^2 w}{\gamma} = \frac{\rho V w}{\mu}\frac{V \mu}{\gamma} = Re\, Ca\,, \tag{5.13}$$

where ρ is the density of the liquid and *Re* the Reynolds number characterizing the ratio between inertia and viscous forces. For the two-phase flow, the ratio between inertial forces of the carrier liquid and the surface tension between the two fluids (oil and water) is

$$We_{12} = \frac{\rho V^2 w}{\gamma_{12}} = \frac{\rho V w}{\mu}\frac{V \mu}{\gamma_{12}} = Re\, Ca_{12}\,. \tag{5.14}$$

Using (5.12), we derive

$$We_{12} = \left[\left(\frac{\bar{\lambda}}{z}\, cos\theta^*\right)\left(\frac{\rho w \gamma}{\mu^2}\right)\right]\left[\left(\frac{\bar{\lambda}}{z}\, cos\theta^*\right)\frac{\gamma}{\gamma_{12}}\right] = \left(\frac{\bar{\lambda}}{z}\, cos\theta^*\right)\left(\frac{\rho w \gamma}{\mu^2}\right) Ca_{12}\,. \tag{5.15}$$

Remark that a secondary dimensionless number appears

$$Br = \left(\frac{\rho w \gamma}{\mu^2}\right). \tag{5.16}$$

This number is constant during the duration of the capillary flow and depends only on the liquid properties. If we denote

$$G = \frac{\gamma}{\gamma_{12}}\,, \tag{5.17}$$

the Weber number can be expressed by

$$We_{12} = Br\ G\ \left(\frac{\bar{\lambda}}{z}\, cos\theta^*\right)^2 = Br\ \left(\frac{\bar{\lambda}}{z}\, cos\theta^*\right) Ca_{12}\,. \tag{5.18}$$

In table S5.4, the capillary and Weber numbers for each liquid are indicated for travel distance $z = 100\,\bar{\lambda}$ (approximately 1.5 cm in the channel).

Table S5.4. Capillary and Weber numbers

Liquid	Distance $\boldsymbol{z = 100\bar{\lambda}}$		Distance $\boldsymbol{z = 1000\bar{\lambda}}$	
	Ca_{12}	We_{12}	Ca_{12}	We_{12}
1-pentanol	3.72×10^{-2}	0.32	3.72×10^{-3}	3.2×10^{-3}
chloroform	5.13×10^{-3}	3.28	5.13×10^{-4}	3.3×10^{-2}
toluene	4.96×10^{-3}	1.77	4.96×10^{-4}	1.8×10^{-2}
n-dodecane	3.02×10^{-3}	0.17	3.02×10^{-4}	1.7×10^{-3}
FC40	1.94×10^{-3}	0.06	1.94×10^{-4}	6.0×10^{-4}
1-nonanol	1.94×10^{-2}	0.02	1.94×10^{-3}	2.2×10^{-4}

n-Dodecane and FC-40 have small capillary and Weber numbers everywhere in the channel. The behavior of the plug is governed by the two-phase surface tension γ_{12}which is relatively high (of the order of 50 mN/m, as indicated in table S5.1). Hence the water plug remains immobile in bridge mode.

At the channel entrance, chloroform and toluene have Weber numbers larger than 1 and moderate capillary numbers. The water plug may be removed from entrance by inertial forces. This is the case of chloroform and sometimes toluene.

Pentanol has a relatively large capillary number at the entrance and the plug is entrained by viscous forces in raft mode.

6. Device schematics

Table S6. Device schematics and their associated figures

Device	Schematic in SI
Figure 2Ai, 2C, 3A, 4A, 7Ai, 7B, 7Di, 7E	Figure S6.1
Figure 2Aii, 3B, 4B	Figure S6.2
Figure 5	Figure S6.3
Figure 7Aii, 7C, 7Dii, 7F	Figure S6.4

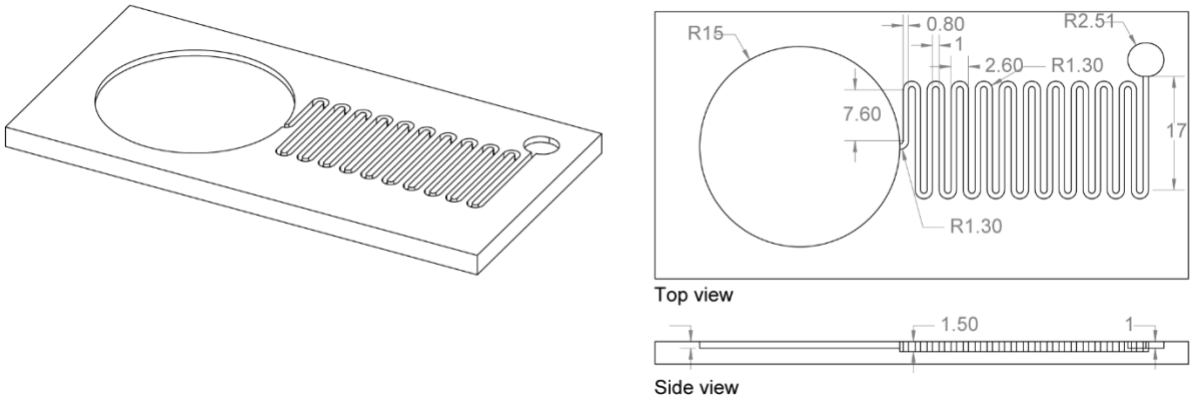

Figure S6.1. Schematic of top view imaging device. Units in mm.

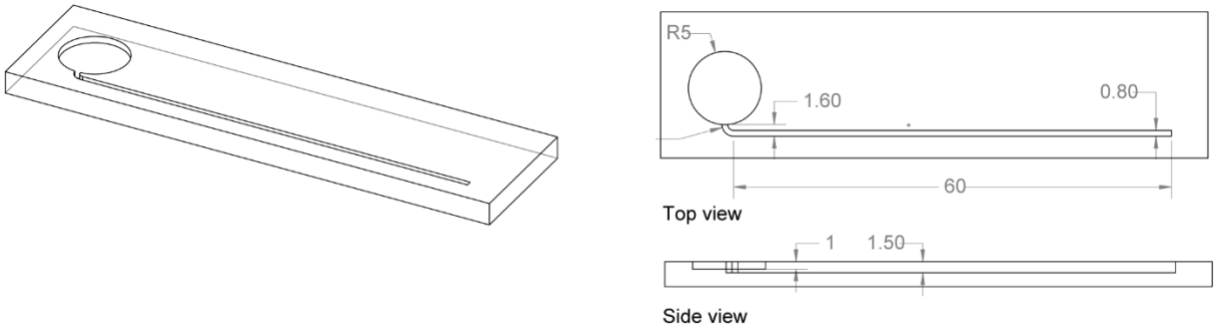

Figure S6.2. Schematic of side view imaging device. Units in mm.

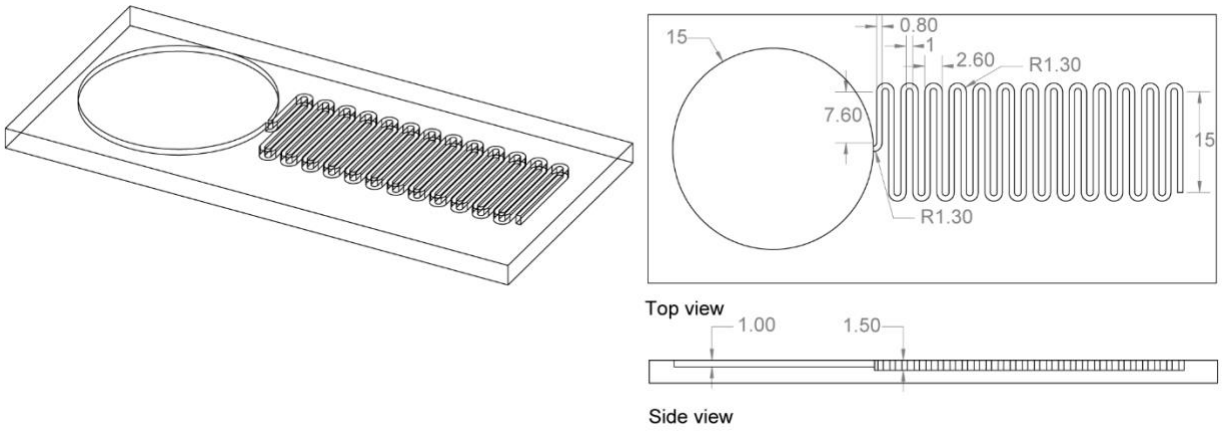

Figure S6.3. Schematic of device used in Figure 5. Units in mm.

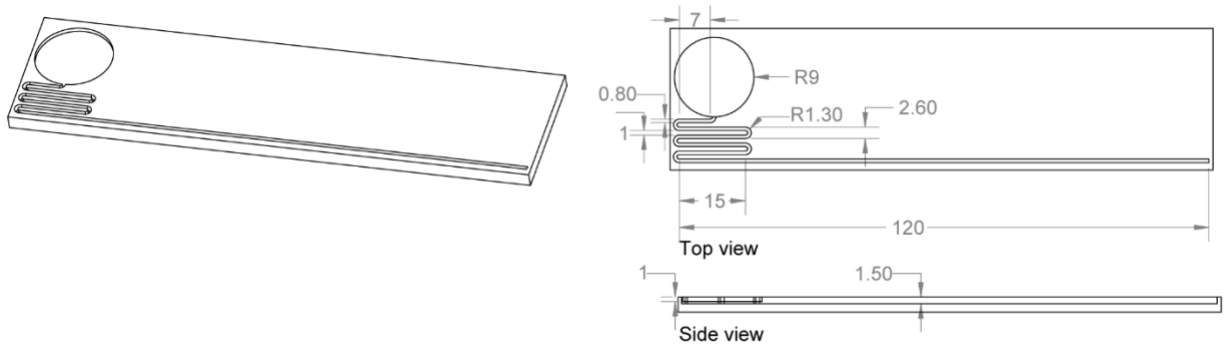

Figure S6.4. Schematic of side view imaging device used in Figure 7. Units in mm

7. References

1. Berthier, J.; Brakke, K. A. The Physics of Microdroplets; John Wiley & Sons, Inc.: Hoboken, NJ, USA, 2012.
2. Brakke, K. A. Exp. Math. 1992, 1, 141.
3. Berthier, J.; Brakke, K. A.; Berthier, E. Open Microfluidics; John Wiley & Sons, Inc.: Hoboken, NJ, USA, 2016.
4. Casavant, B. P.; Berthier, E.; Theberge, A. B.; Berthier, J.; Montanez-Sauri, S. I.; Bischel, L. L.; Brakke, K.; Hedman, C. J.; Bushman, W.; Keller, N. P.; Beebe, D. J. Proc. Natl. Acad. Sci. U. S. A. 2013, 110, 10111.
5. Taher, A.; Jones, B.; Fiorini, P.; Lagae, L. In Microfluidics, BioMEMS, and Medical Microsystems XV; Gray, B. L., Becker, H., Eds.; International Society for Optics and Photonics: San Francisco, 2017; Vol. 10061, p 1006108.
6. Clift, R. (Roland); Grace, J. R.; Weber, M. E. Bubbles, drops, and particles; Academic Press: New York, NY, USA, 1978.
7. Kim, S.; Thiessen, P. A.; Bolton, E. E.; Chen, J.; Fu, G.; Gindulyte, A.; Han, L.; He, J.; He, S.; Shoemaker, B. A.; Wang, J.; Yu, B.; Zhang, J.; Bryant, S. H. Nucleic Acids Res. 2016, 44.

8. Freitas, A.; Quina, F.; Carroll, F. J. Phys. Chem. B 1997, 5647, 7488.
9. Mazutis, L.; Griffiths, A. D. Lab Chip 2012, 12 (10), 1800.
10. Berthier, J.; Gosselin, D.; Berthier, E. Microfluid. Nanofluidics 2015, 19, 497.
11. Berthier, J.; Brakke, K. A.; Berthier, E. Microfluid. Nanofluidics 2014, 16, 779.
12. Lucas, R. Kolloid-Zeitschrift 1918, 23, 15.
13. Washburn, E. W. Phys. Rev. 1921, 17, 273.
14. Rideal, E. K. Philos. Mag. Ser. 6 1922, 44, 1152.
15. Bosanquet, C. H. Philos. Mag. Ser. 6 1923, 45, 525.
16. Berthier, J.; Brakke, K. A.; Furlani, E. P.; Karampelas, I. H.; Poher, V.; Gosselin, D.; Cubizolles, M.; Pouteau, P. Sensors Actuators, B Chem. 2015, 206, 258.
17. Berthier, J.; Gosselin, D.; Delapierre, G. Sens. Transducers J 2015, 191, 40.

APPENDIX B

Chapter 3. Droplet Incubation and Splitting in Open Microfluidic Channels

SI references

Reproduced in part from Berry, S. B.; Lee, J. J.*; Berthier, J.; Berthier, E.; Theberge, A. B. Open Channel Droplet-Based Microfluidics. Anal. Methods 2019, 11, 4528-4536.*

**denotes co-authorship.*

The supporting information for "Droplet Incubation and Splitting in Open Microfluidic Channels" includes additional information that readers might find useful for adapting the open channel systems presented here for their own work; this includes detailed schematics and dimensions of each platform described in this work and corresponding computer aided design (CAD) files, a derivation of the analytical model used to describe flow in the bypass system, an illustrated workflow of the droplet length measuring protocol used for Figure 3D, results demonstrating the reproducibility of droplet splitting in one device, and videos showing the use and function of each platform in this work.

S1. Droplet Behavior Modes in Open Channel Platform

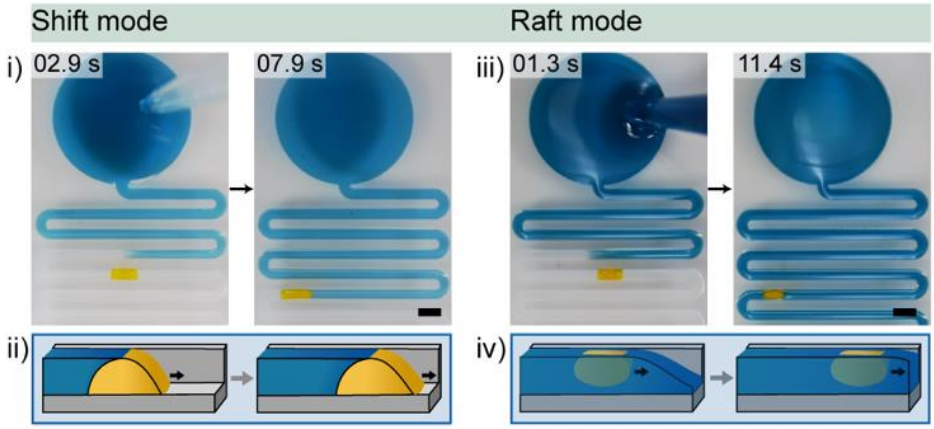

Figure S1. A single static aqueous droplet (yellow) is pipetted into the channel and can display either shift mode ((i) and (ii)) or raft mode ((iii) and (iv)) as carrier fluid (blue) moves the aqueous droplet down channel.[1] For shift mode, the carrier phase is 1-pentanol; for raft mode, the carrier phase is toluene. Scale bar: 2 mm. Schematics in (ii) and (iv) are reproduced from Lee et al.[1]

S2. Detailed Device Schematics and Dimensions

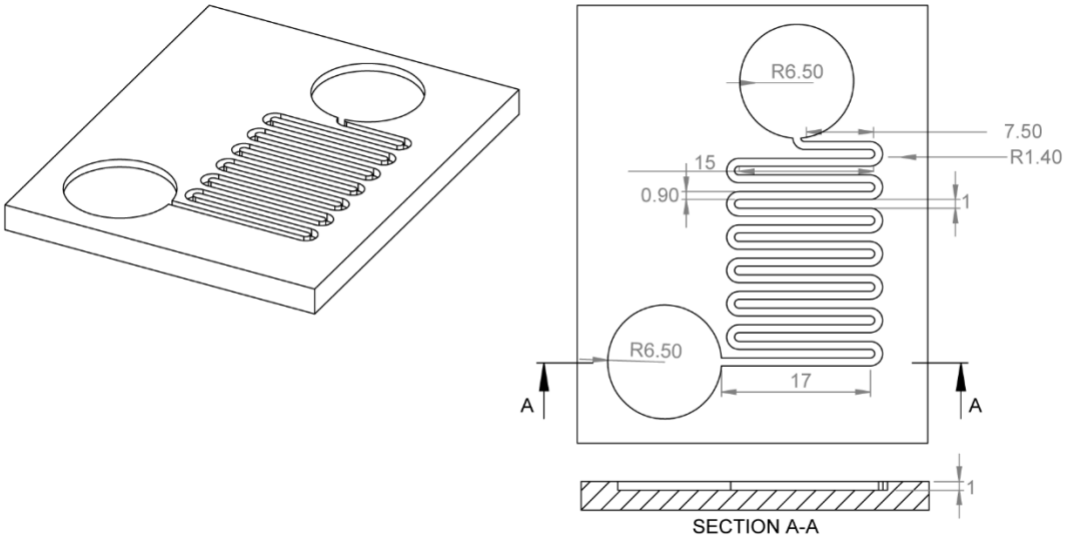

Figure S2i. Detailed device schematics illustrating device dimensions for the Coalescence Device (Figure 2A). Units in mm.

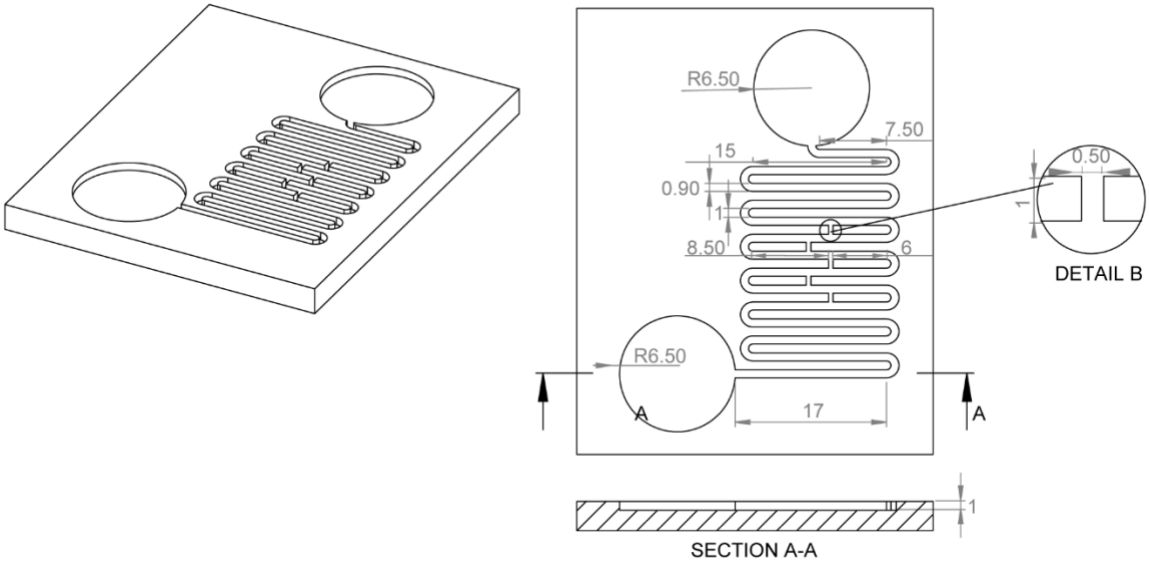

Figure S2ii. Detailed device schematics illustrating device dimensions for the Bypass Device without a step (Figure 2B). Units in mm.

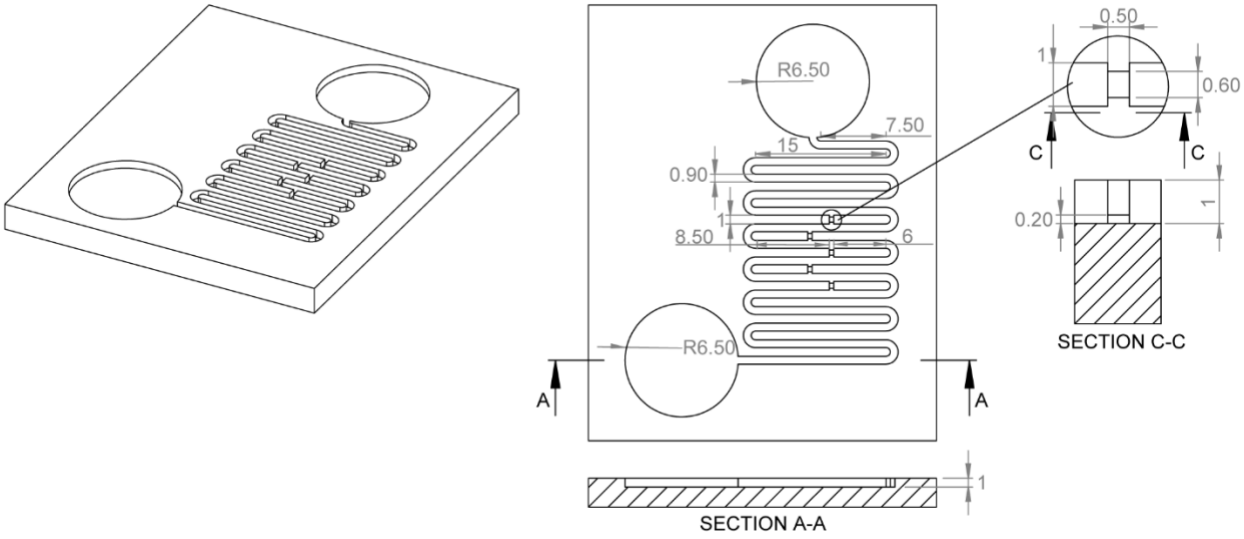

Figure S2iii. Detailed device schematics illustrating device dimensions for the Bypass Device with a step (Figure 2C). Units in mm.

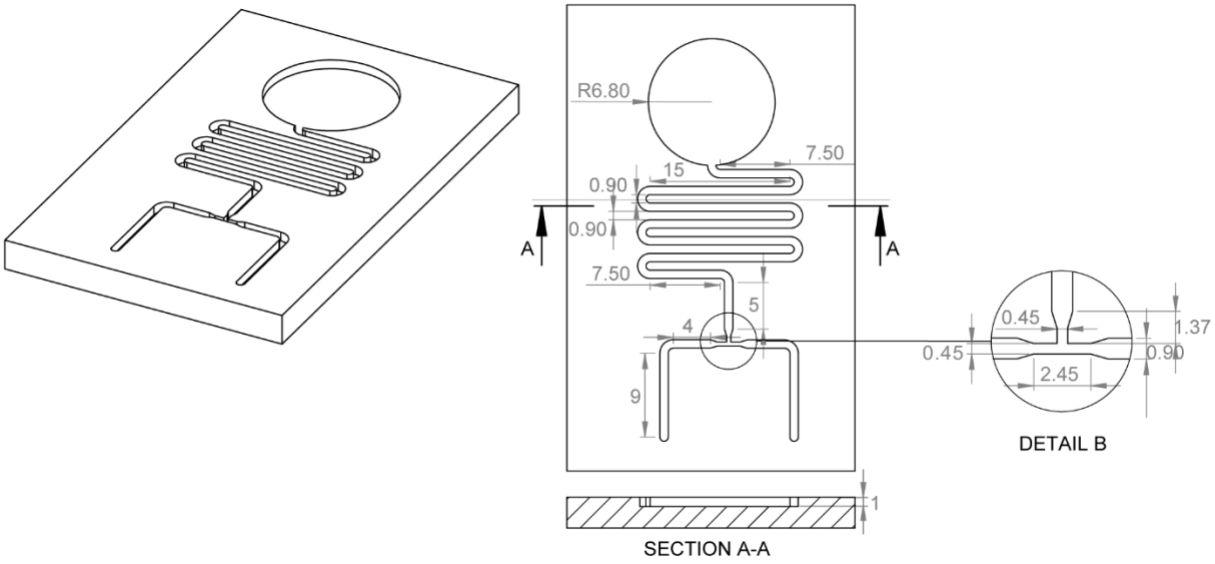

Figure S2iv. Detailed device schematics illustrating device dimensions for the symmetric splitting T junction device (Figure 4B). Units in mm.

S3. Derivation of Analytical Model for Resistance and Flux

In this model, we considered an open channel system with a bifurcation and two nodes, where the flows partition at the first node (green dot) and join at the second (red dot). Between the

two nodes are two different branches (blue and yellow outlines); Branch 1 is an extension of the main channel, and Branch 2 is the bypass channel with a step in the middle (Figure S3i).

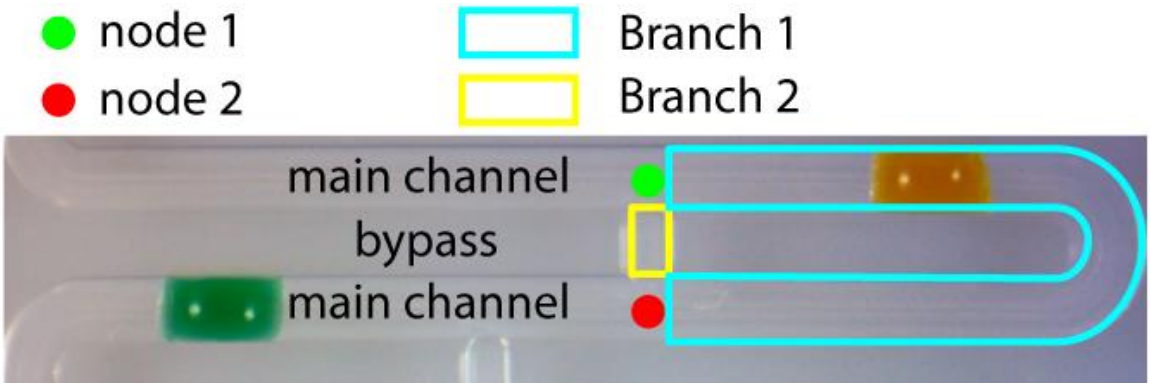

Figure S3i. Labeled top view image of open channel system.

Based on previous work[1] on the creation of a generalized Lucas-Washburn law for varying shapes driven by capillary flow and application of the analogy of an electric circuit, we can write:

$$\Delta P = P_1 - P_2 \approx \tilde{R}_1 Q_1 \approx \tilde{R}_2 Q_2 \quad (1)$$

$$\mu \frac{p}{\lambda S^2} L = R \quad (2)$$

Where P_1 and P_2 are the pressures at node 1 and node 2, respectively, R is the resistance, L is the length, Q is the flux, S is the channel cross sectional area, μ is the liquid viscosity, p is the total perimeter, and λ is the friction length.[2]

Solving equation 1 for Q:

$$\left(\frac{\tilde{R}_1}{\tilde{R}_2}\right) = \left(\frac{Q_2}{Q_1}\right) \quad (3)$$

From Equation 3, we have a relation that describes the flow rate in terms of the resistance and can be used to calculate the specific resistance for each channel with physical parameters from the system. However, Branch 2 has a heterogenous cross section due to the step; therefore, the resistances of each section of the bypass channel must be considered to find the total resistance through Branch 2:

$$\left(\frac{\tilde{R}_1}{\tilde{R}_2}\right) = \left(\frac{\widetilde{R_1}}{\widetilde{R_i}+\widetilde{R_{ii}}+\widetilde{R_{iii}}}\right) = \left(\frac{Q_2}{Q_1}\right) \tag{4a}$$

And plugging in Equation 2:

$$\left(\frac{\mu\frac{p_1}{\lambda_1 s_1^2}L_1}{\mu\frac{p_i}{\lambda_i s_i^2}L_i+\mu\frac{p_{ii}}{\lambda_{ii} s_{ii}^2}L_{ii}+\mu\frac{p_{iii}}{\lambda_{iii} s_{iii}^2}L_{iii}}\right) = \left(\frac{Q_2}{Q_1}\right) \tag{4b}$$

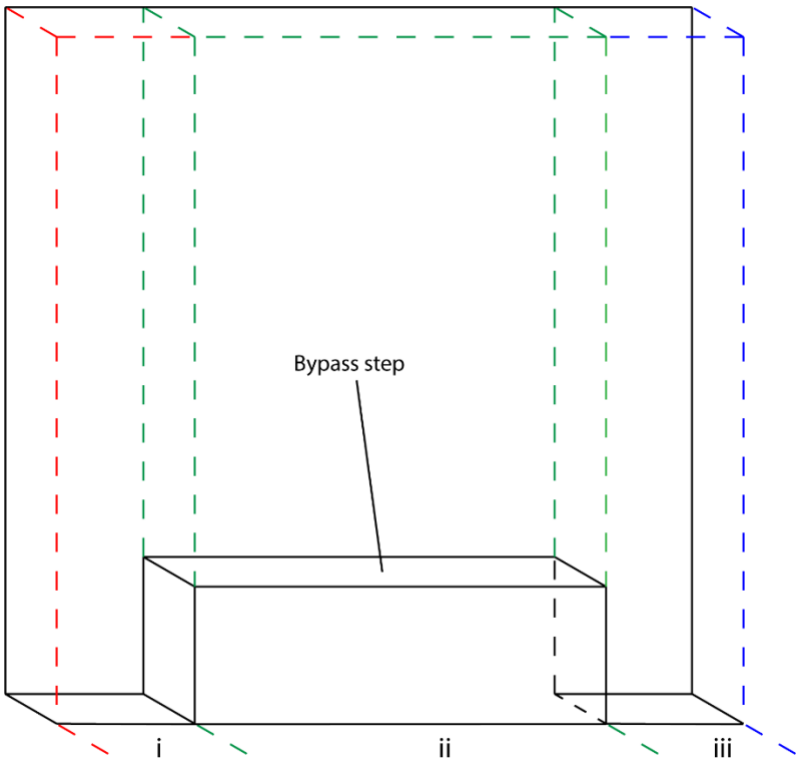

Figure S3ii. Isometric view of cross section of Branch 2 (Bypass)

Where i, ii, and iii represent the separate sections within the bypass channel (Figure S3ii). Plugging in the physical parameters into Equation 4b provides the ratio of the fluxes between the bypass channel and the main channel. For our specific stepped bypass platform:

$$\frac{Q_2}{Q_1} = 2.68 \quad (5a)$$

And without a step in the bypass channel:

$$\frac{Q_2}{Q_1} = 3.18 \quad (5b)$$

These calculations demonstrate that incorporation of the step into the bypass decreases the flux through the bypass by increasing the resistance through the bypass channel. The decreased flux through the bypass (Branch 2) corresponds to an increased flux through the main channel (Branch 1), which drives the droplets completely through the curves in the channels and allows them to flow to the outlet.

S4. Workflow for Droplet Length Measurements

To measure the length of the aqueous droplets in our channels, we designed and fabricated T junction platforms without outlet reservoirs. As with the devices with the outlet reservoir, we pipetted a 3 μL droplet upstream of the T junction and the added carrier fluid to the inlet reservoir. After initiation of spontaneous capillary flow (SCF) and splitting of the droplet, daughter droplets flowed to the end of the channel, where they stopped and were compressed as the device filled with carrier fluid. Once the device was completely filled and flow had completely ceased, the daughter droplets at the end of the channel were imaged. Images of droplets were then analyzed

with ImageJ. Specifically, A-B) images were opened (symmetric droplet image) and scaled (Analyze, set scale); C) the "Segmented Line" tool was then selected and a vertical line was drawn from the top of each droplet to the bottom. D) The segmented line was measured (Analyze, measure) and droplet lengths were recorded.

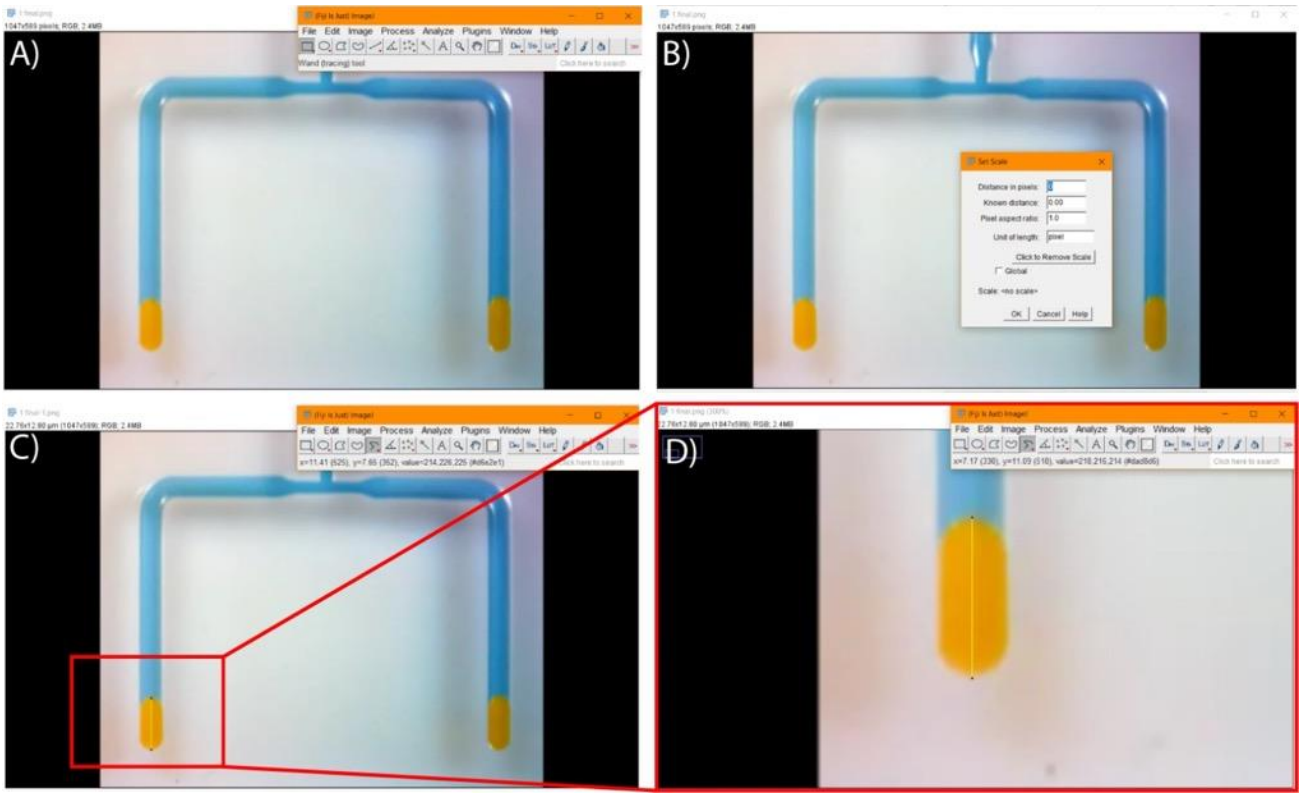

Figure S4. Workflow for droplet length measurement. A) The image to be measured is opened using ImageJ; B) to set the scale, we selected "Analyze, set scale" and changed the scale from pixels to μm; C) the Segmented Line tool is selected, and a line is draw from one end of the droplet to the other (interface of droplet and carrier phase and boundary of droplet and end of channel); D) zoomed-in image illustrating the line drawn on the droplet.

S5. Droplet splitting reproducibility within a single device

To demonstrate the reproducibility of droplet splitting within a single device, we measured the droplet area and perimeter after splitting in one device. After flowing the droplet through the 1:1 T-junction (Fig. 4B) and measuring droplet area and perimeter once it reached the outlet

reservoir, the device was washed with 70% ethanol, rinsed with water, dried with compressed air, and then reused. Images were analyzed using ImageJ and the "circle" drawing tool to encapsulate the droplet prior to measurement and recording.

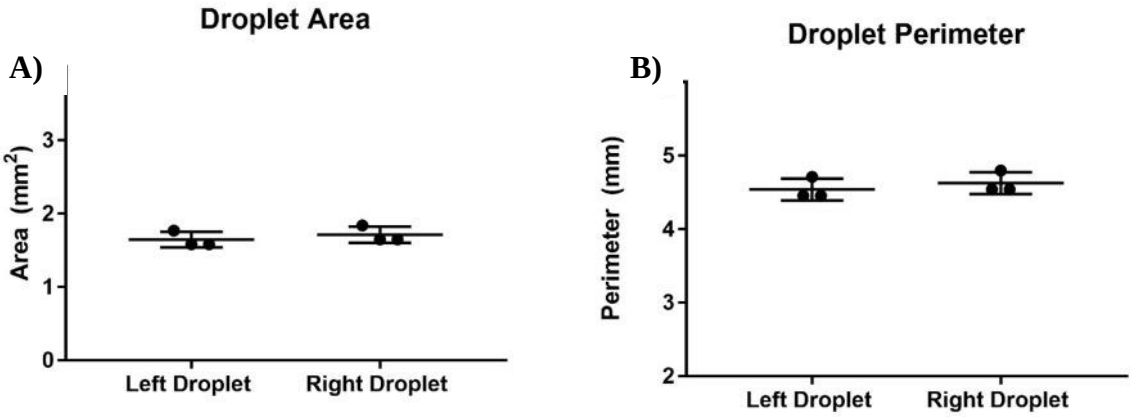

Figure S5. Reproducibility of droplet splitting within one device. Daughter droplet area (A) and perimeter (B) were measured using ImageJ for one droplet split using the 1:1 T-junction device in n=3 independent experiments. After splitting and droplet quantification, the same device was cleaned, dried, and used for the subsequent independent experiment. Mean and standard deviation are indicated for n=3 droplets across n=3 independent experiments.

6. References

1. Lee, J.J.; Berthier, J.; Brakke, K.A.; Dostie, A.M.; Theberge, A.B.; Berthier, E. Droplet behavior in Open Biphasic Microfluidics. *Langmuir*, **2018**, 34, 18, 5358-5366.
2. Berthier, J.; Gosselin, D.; Berthier, E. A generalization of the Lucas-Washburn Rideal law to composite microchannels of arbitrary cross section. Microfluid. Nanofluid., 2015, 19, 3, 497-507.
3. Lee, J.J.; Karampelas, I.H.; Brakke, K.A.; Theberge, A.B.; Berthier, E.; Berthier, J. Capillary flow of solvents and aqueous liquids in rounded open microgrooves. Langmuir. Accepted.

APPENDIX C

Chapter 4. Capillary Flow in Open microgrooves: bifurcations and networks

Supporting Information (SI) references

Reproduced in part from Lee, J. J.; Berthier, J.*; Theberge, A. B.; Berthier, E. Capillary Flow in Open Microgrooves: Bifurcations and Networks. Langmuir 2019, 35 (32), 10667–10675.*

**denotes co-authorship. J.J.L contributed to the overall fabrication designs and experimental designs. J.B. developed the analytical model and numerical simulation of this work.*

1. Design schematics

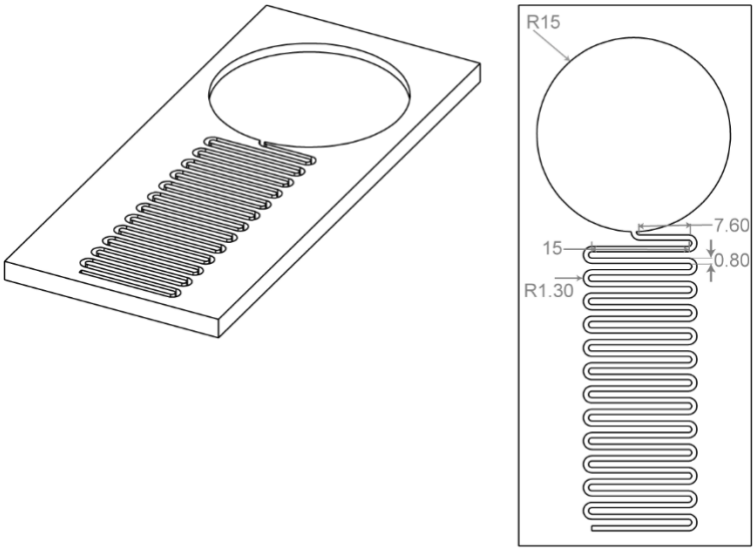

Figure S1.1. Schematic of a simple open-channel. Units in mm.

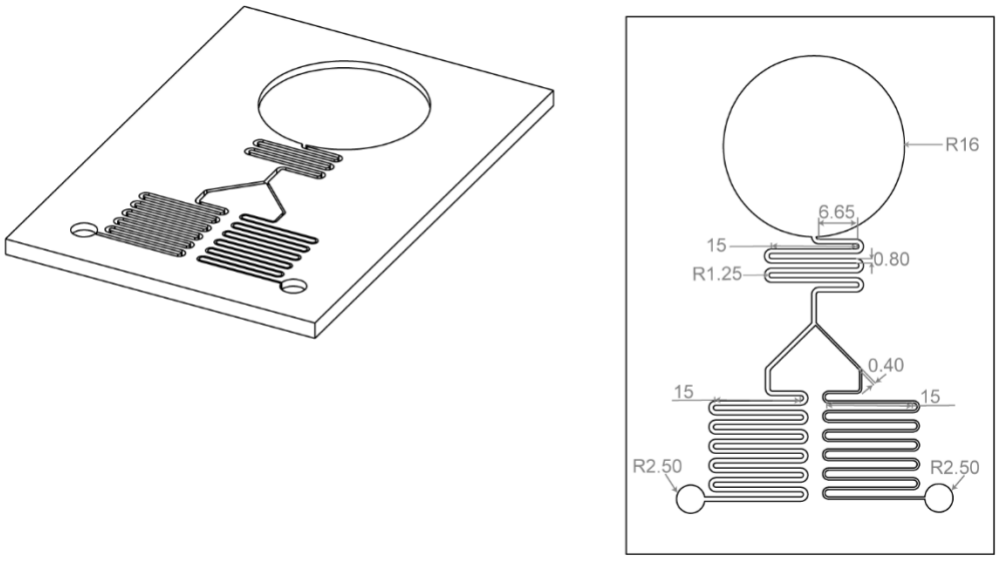

Figure S1.2. Schematic of a bifurcation channel. Units in mm.

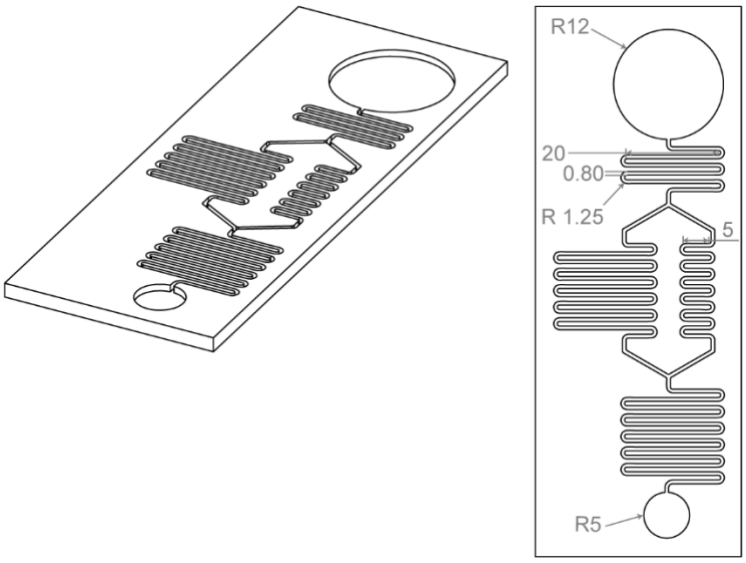

Figure S1.3. Schematic of a simple network channel. Units in mm.

2. Numerical models

2.1: COMSOL model for the friction length

A closed form expression for the average friction length does not exist for complicated geometries. A numerical approach can be utilized to find this parameter. Here we use the finite element software COMSOL (www.COMSOL.com).

First a geometry similar to that of the channel is set up. Note that we perform a closed channel calculation with COMSOL. The open surface is then simulated by a solid surface without friction (symmetry condition). This condition introduces an approximation since the real open surface is not flat but slightly bent inwards. The symmetry condition is however justified by the zero shear rate at the free surface, as shown by Brackbill and coworkers.[1] This no-shear condition at the free surface is also used by Koliopoulos and coworkers[2] for the determination of the flow in open rectangular microchannels. An arbitrary average velocity is imposed in the inlet cross section while a zero-pressure condition is set up in the outlet cross section. We emphasize that the inlet velocity can be arbitrary since the friction length does not depend on the average velocity. The shear rate at the wall is deduced from the derivative of the calculated velocities in a cross section, at the nodes of the geometrical meshes close to the solid wall. The shear rate $\dot{\gamma}$ is then averaged along the perimeter of the cross section in order to obtain the averaged shear rate $\frac{V}{\bar{\lambda}}$.

Figure S2.1 shows the approach for the rounded open channel. The input average velocity is 1 mm/s, and the shear rate averaged from point a to b is $\overline{(\dot{\gamma})}_{a,b} = 6.8\ s^{-1}$. The whole perimeter averaged shear rate is then

$$\overline{(\dot{\gamma})} = \overline{(\dot{\gamma})}_{a,b}\ \frac{p_w}{p_w + p_F} \qquad \text{(SI.2.1)}$$

In the present case, the form factor $\frac{p_w}{p_w+p_F}$ is equal to 0.77. Then, using the relation

$$\bar{\lambda} = \frac{V}{\overline{(\dot{\gamma})}}, \qquad \text{(SI.2.2)}$$

where V=1 mm/s, we find a friction length of 192 µm.

Figure S2.2 shows the same approach for a double cylindrical open channel. In such a case, we find $\overline{(\dot{\gamma})}$~0.6 $\overline{(\dot{\gamma})}_{a,b}$=26.4 s^{-1}. The friction length is then 38.8 µm. Of course, the approach can also be used for closed channels, as shown in Figure S2.3.

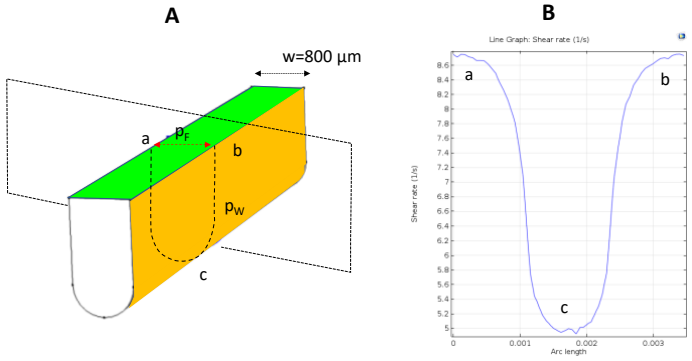

Figure S2.1. COMSOL model for the calculation of the shear rate in a cross section of a rounded open channel. A) The cover plate (green parallelogram in the figure), the cross section where the velocity profile is considered for the shear rate calculation is defined by the plane perpendicular to the channel. B) Shear rate profile at the wall in curvilinear coordinates system. The points denoted a,b,c are reported from A to B.

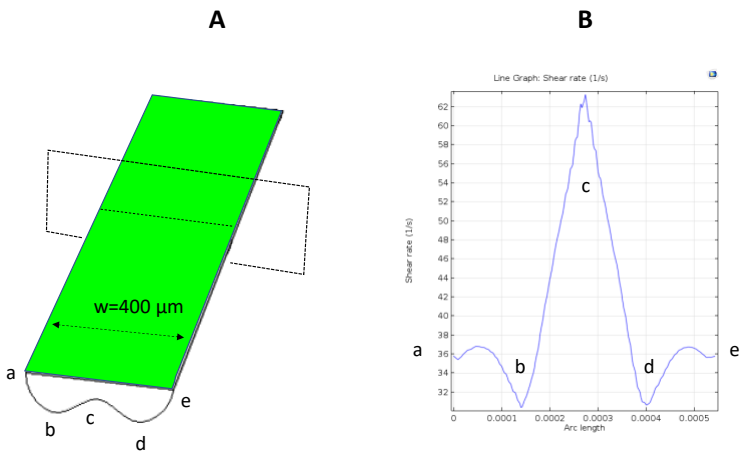

Figure S2.2. COMSOL model for the calculation of the shear rate in a cross section of a double half cylindrical open channel. A) The cover plate (green parallelogram in the figure), the cross section where the velocity profile is considered for the shear rate calculation is defined by the plane perpendicular to the channel. B) Shear rate profile at the wall in curvilinear coordinates system. The points denoted a,b,c,d,e are reported from A to B.

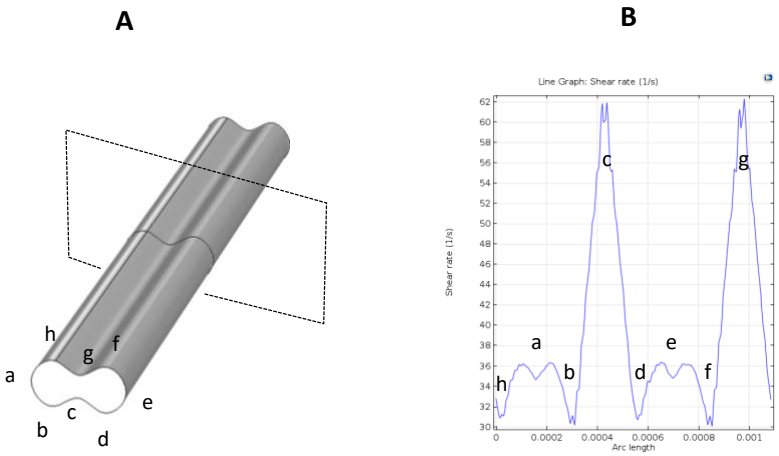

Figure S2.3. COMSOL model for the calculation of the shear rate in a cross section of a double cylindrical closed channel. A) The cross section where the velocity profile is considered for the shear rate calculation is defined by the plane perpendicular to the channel. B) Shear rate profile at the wall in curvilinear coordinates system. The points denoted a,b,c,d,e,f,g,h are reported from A to B.

2.2 Iterative solution of system (23)

The system (23), corresponding to the travel distances after an asymmetrical bifurcation, is a system of two fully coupled quadratic equations. We recall that this system is

$$z_{1,i+1} = -K_1 + \sqrt{K_1^2 + K_{12} z_{2,i} - \frac{2B_1}{A_1}\tau}$$

$$z_{2,i+1} = -K_2 + \sqrt{K_2^2 + K_{12} z_{1,i+1} - \frac{2B_2}{A_2}\tau}\,, \qquad \text{(SI.2.3)}$$

where i is the iteration index. Using an initial value $z_{1,0} = 0$, $z_{2,1}$ is obtained by solving the second quadratic equation. Inserting $z_{2,1}$ in the first quadratic equation one obtains $z_{1,1}$. The process is repeated until convergence.

In Table S2.1, (obtained with Excel) we give an example of an asymmetrical bifurcation, starting at time 27 s, at a distance of 90 mm from inlet. At each time (τ in our text), we indicate the different values of the iterations (successive columns z_{1j} and z_{2j}). It was observed that convergence is fast (columns pasted in green). Here we show only 5 iterations. After 6 iterations approximately stabilization is reached within 5 μm. The "real" travel distances are obtained by adding 90 mm to the converged values (columns pasted in blue): Upon convergence of the coupled numerical equations, one obtains the total travel distances at time τ.

Table S2.1. Example of iterations to obtain the solution of the system (SI.2.3).

Time	z_{1j}	z_{2j}	z_{1j}	z_{2j}	z_{1j}	z_{2j}	z_{1j}	z_{2j}	z_{1j}	z_{2j}	z_1 real	z_2 real
28,00	0,00	56,02	15,36	50,04	17,60	49,11	17,94	48,97	**17,99**	**48,95**	**107,99**	**138,95**
38,00	0,00	77,61	32,99	67,78	36,14	66,78	36,46	66,68	**36,49**	**66,67**	**126,49**	**156,67**
48,00	0,00	94,89	49,65	82,47	53,16	81,53	53,42	81,46	**53,44**	**81,45**	**143,44**	**171,45**
58,00	0,00	109,72	65,17	95,41	68,81	94,55	69,03	94,50	**69,04**	**94,50**	**159,04**	**184,50**
68,00	0,00	122,92	79,66	107,16	83,34	106,38	83,52	106,34	**83,53**	**106,34**	**173,53**	**196,34**
78,00	0,00	134,93	93,28	118,01	96,94	117,30	97,09	117,27	**97,10**	**117,27**	**187,10**	**207,27**
88,00	0,00	146,02	106,15	128,15	109,76	127,50	109,89	127,47	**109,90**	**127,47**	**199,90**	**217,47**
98,00	0,00	156,38	118,36	137,70	121,92	137,11	122,04	137,09	**122,04**	**137,09**	**212,04**	**227,09**
108,00	0,00	166,13	130,01	146,77	133,51	146,22	133,61	146,20	**133,61**	**146,20**	**223,61**	**236,20**
118,00	0,00	175,38	141,17	155,42	144,60	154,91	144,69	154,89	**144,69**	**154,89**	**234,69**	**244,89**

128,00	0,00	184,18	151,89	163,71	155,26	163,23	155,34	163,21	**155,34**	**163,21**	**245,34**	**253,21**
138,00	0,00	192,61	162,21	171,67	165,52	171,22	165,59	171,21	**165,59**	**171,21**	**255,59**	**261,21**
148,00	0,00	200,70	172,18	179,34	175,43	178,92	175,49	178,91	**175,49**	**178,91**	**265,49**	**268,91**
158,00	0,00	208,49	181,83	186,76	185,02	186,36	185,08	186,35	**185,08**	**186,35**	**275,08**	**276,35**
168,00	0,00	216,02	191,19	193,95	194,32	193,57	194,37	193,56	**194,38**	**193,56**	**284,38**	**283,56**
178,00	0,00	223,30	200,28	200,92	203,36	200,56	203,41	200,55	**203,41**	**200,55**	**293,41**	**290,55**
188,00	0,00	230,37	209,13	207,70	212,15	207,36	212,20	207,35	**212,20**	**207,35**	**302,20**	**297,35**

We have remarked that, when the seed ($z_{1,0}$ or $z_{2,0}$) corresponds to the "slowest" channel, the convergence is fast. In the opposite case, we have sometimes observed oscillations of the solution. In general, it is best to use the "slowest" channel at the beginning, i.e. the largest channel, for the seed of the iterations. We don't have an explanation for this behavior yet. Figure S2.4 shows the travel distances vs. time indicated in Table S2.1.

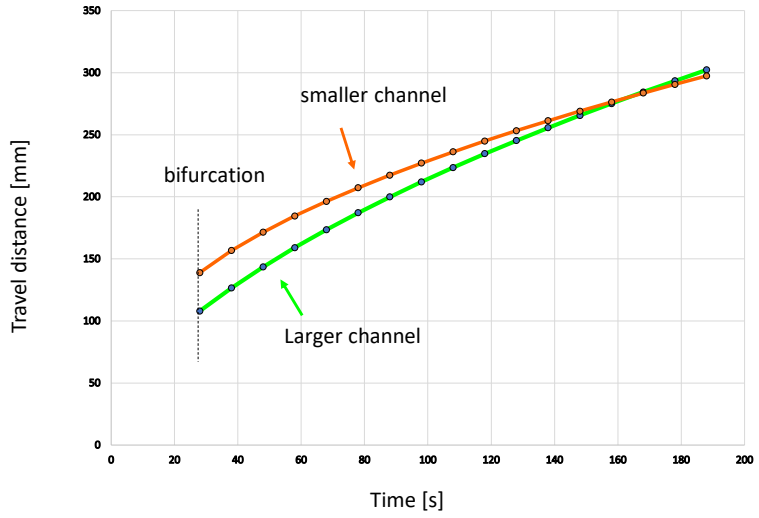

Figure S2.4. Travel distances in the two channels after an asymmetrical bifurcation, obtained by iteration of system SI.2.3.

3. Calculation of the different flows past the second junction

In general, one of the flows in the two daughter branches arrives first at the second fork (confluence). It may be because one of the forks has a shorter length than the other (Figure S3.1 showing a bypass), or it can be due to the uneven velocity in the branches (Figure S3.2 showing different cross-sectional branches).

Figure S3.1. Capillary flow in a bypass preceding the flow in the root channel, after the bypass confluence. Scale bat at 1 mm.

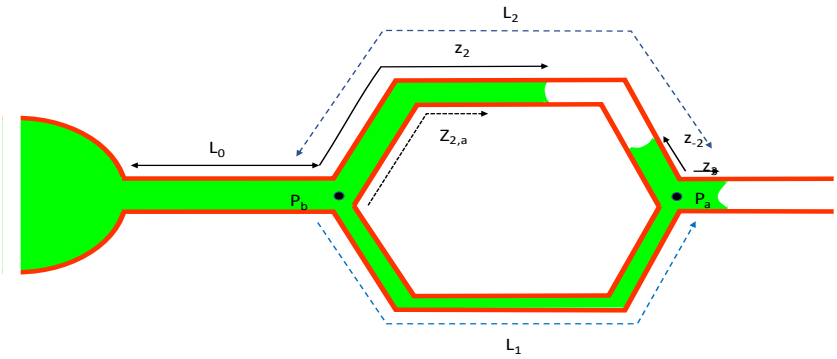

Figure S3.2. Sketch of the capillary flow after the arrival at the second fork (case of different cross sections of the two daughter branches). The indices *a* and *b* stand for "before the network" and "after the network".

We derive the system of equations governing the motion of the three capillary flows: (1) z_1 the capillary flow in the "slower" daughter channel, (2) z_{-1} the reverse capillary flow in the same daughter channel, and (3) z_3 the capillary flow in the reunited root channel.

The pressure P_b can be expressed as a pressure drop from the entrance, and as a balance between friction and capillary pressure

$$-P_b = L_0\, p_0\, \mu\, \frac{V_0}{\bar{\lambda}_0}\frac{1}{S_0} = -z_2\, p_2\, \mu\, \frac{V_2}{\bar{\lambda}_2}\frac{1}{S_2} + \frac{\gamma\, p_2\, cos\theta_2^*}{S_2}. \quad \text{(SI.3.1)}$$

Similarly, the pressure P_a can be expressed as a pressure drop

$$-P_a = L_0\, p_0\, \mu\, \frac{V_0}{\bar{\lambda}_0}\frac{1}{S_0} + L_1\, p_1\, \mu\, \frac{V_1}{\bar{\lambda}_1}\frac{1}{S_1}, \quad \text{(SI.3.2)}$$

or as the balance between capillary pressure and pressure drop

$$-P_a = -z_3\, p_3\, \mu\, \frac{V_3}{\bar{\lambda}_3}\frac{1}{S_3} + \frac{\gamma\, p_3\, cos\theta_3^*}{S_3} = -z_{-2}\, p_2\, \mu\, \frac{V_{-2}}{\bar{\lambda}_2}\frac{1}{S_2} + \frac{\gamma\, p_2\, cos\theta_2^*}{S_2}, \quad \text{(SI.3.3)}$$

where z_{-2} and V_{-2} are respectively the reverse travel distance and velocity in the incomplete daughter branch 2.

Mass conservation equations —at nodes *a* and *b*—can be added to the system (SI.3.1), (SI.3.2) and (SI.3.3)

$$S_0 V_0 = S_1 V_1 + S_2 V_2, \quad \text{(SI.3.4)}$$

and

$$S_1 V_1 = S_2 V_{-2} + S_3 V_3. \quad \text{(SI.3.55)}$$

The system comprises 7 equations (7 equal signs), and 7 unknowns P_a, P_b, V_0, V_1, V_2, V_{-2} and V_3 (because $V_i = dz_i/dt$). In order to make it tractable, we first simplify the notations, using $A_i =$

$\mu\ p_i/\bar{\lambda}_i$ for i=1,2,3,-2, $B_i = \gamma\ p_i \cos\theta_i^*$ and $K_i = 2\ B_i/A_i$. First consider P_a and equation (SI.3.3). We can write

$$z_3\ V_3 \frac{A_3}{S_3} - z_{-2}\ V_{-2} \frac{A_2}{S_2} = \frac{B_3}{S_3} - \frac{B_2}{S_2}, \qquad \text{(SI.3.6)}$$

which can be integrated in function of the time τ_a counted after the second fork as

$$z_3^2\ \frac{A_3}{S_3} - z_{-2}^2\ \frac{A_2}{S_2} = \left(\frac{2\ B_3}{S_3} - \frac{2\ B_2}{S_2}\right)\ \tau_a. \qquad \text{(SI.3.7)}$$

Note that z_3 and z_{-2} are counted from point a. Second, consider P_a-P_b. We can express this difference in two ways

$$P_b - P_a = -z_{-2}\ V_{-2} \frac{A_2}{S_2} + z_2\ V_2 \frac{A_2}{S_2} = L_1\ V_1 \frac{A_1}{S_1} = L_1 \frac{A_1}{S_1^2}(S_2 V_{-2} + S_3 V_3), \qquad \text{(SI.3.8)}$$

and we can integrate

$$\left(z_2 - z_{2,a}\right)^2 - z_{-2}^2\ =\ 2\ L_1\ \frac{A_1}{A_2}\frac{S_2}{S_1^2}(S_2 z_{-2} + S_3 z_3), \qquad \text{(SI.3.9)}$$

remarking that $z_{2,a}$ is the travel distance z_2 when the flow in branch 1 reaches the second fork. Finally, we make use of the whole chain of capillary segments and derive from (SI.3.2) and (SI.3.3)

$$-2\ P_a = -z_3\ V_3 \frac{A_3}{S_3} + \frac{B_3}{S_3} - z_{-2}\ V_{-2} \frac{A_2}{S_2} + \frac{B_2}{S_2} = 2\ L_0\ V_0 \frac{A_0}{S_0} + 2\ L_1 V_1 \frac{A_1}{S_1}. \qquad \text{(SI.3.10)}$$

Using (SI.3.4) and (SI.3.5), we can rewrite (SI.3.10) under the form

$$-z_3\,V_3\frac{A_3}{S_3}+\frac{B_3}{S_3}-z_{-2}\,V_{-2}\frac{A_2}{S_2}+\frac{B_2}{S_2}=2\,L_0(S_2V_2+S_2V_{-2}+S_3V_3)\frac{A_0}{S_0^2}+2\,L_1(S_2V_{-2}+S_3V_3)\frac{A_1}{S_1^2},$$

(SI.3.11)

which can be integrated as

$$z_3^2\frac{A_3}{S_3}+z_{-2}^2\,\frac{A_2}{S_2}=\left(\frac{2B_3}{S_3}+\frac{2B_2}{S_2}\right)\tau_a-4\,L_0S_2\left(z_2-z_{2,a}\right)\frac{A_0}{S_0^2}-4(S_2z_{-2}+S_3z_3)\left(L_0\frac{A_0}{S_0^2}+L_1\frac{A_1}{S_1^2}\right).$$

(SI.3.12)

The system (SI.3.7), (SI.3.9) and (SI.3.12) is a system of three quadratic equations with three unknowns (z_2, z_{-2}, z_3). We can slightly simplify it by adding (SI.3.7) and (SI.3.12), to obtain a replacement for (SI.3.12)

$$z_3^2+2\,L_0S_2\left(z_2-z_{2,a}\right)\frac{A_0\,S_3}{A_3S_0^2}+2(S_2z_{-2}+S_3z_3)\left(L_0\frac{A_0S_3}{A_3S_0^2}+L_1\frac{A_1\,S_3}{A_3S_1^2}\right)-K_3\tau_a=0\,,\qquad\text{(SI.3.13)}$$

or

$$z_3^2+2\left(L_0\frac{A_0}{S_0^2}+L_1\frac{A_1}{S_1^2}\right)\frac{S_3^2}{A_3}z_3+2\,L_0\frac{A_0\,S_2S_3}{A_3S_0^2}\left(z_2-z_{2,a}\right)+2\left(L_0\frac{A_0S_2S_3}{A_3S_0^2}+L_1\frac{A_1\,S_2S_3}{A_3S_1^2}\right)z_{-2}-K_3\tau_a=0\,.$$

(SI.3.14)

4. Top view images of sequences of fluidic flow in a network

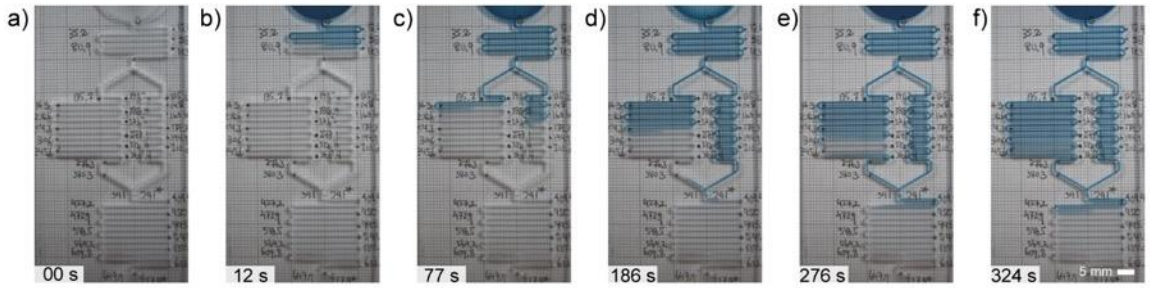

Figure S4.1. Top view images showing sequence of flow of carrier fluid (blue) in the network channel. a) Before filling the channel with carrier fluid. b) Carrier fluid flow in the main channel. c) Carrier fluid reaching the first bifurcation fork then reaching the daughter channel. d) Carrier fluid reaching the second bifurcation fork. e) Backflow of the carrier fluid in the daughter channel. f) Fluid merges in the channel.

5. References

1. Brackbill, J.; Kothe, D. .; Zemach, C. A Continuum Method for Modeling Surface Tension. J. Comput. Phys. 1992, 100 (2), 335–354.
2. Kolliopoulos, P.; Jochem, K. S.; Lade, R. K.; Francis, L. F.; Kumar, S. Capillary Flow with Evaporation in Open Rectangular Microchannels. Langmuir 2019, 35 (24), 8131–8143.

APPENDIX D

Chapter 5. Open-Channel Capillary Trees and Capillary Pumping

References to SI

Reproduced in part from Lee, J. J.; Berthier, J.*; Kearney, K. E.; Berthier, E.; Theberge, A. B. Open-channel Capillary Trees and Capillary Pumping. Langmuir 2020, 36, 12795–12803.*

**denotes co-authorship. J.J.L contributed to the overall fabrication designs and experimental designs. J.B. developed the analytical model and numerical simulation of this work.*

1. Definition of the generalized Cassie angle

The generalized Cassie angle, θ^{*1} is defined by

$$\cos\theta^* = \frac{-p_F + \sum_{i=1,n} p_{w,i} \cos\theta_i}{p} \quad \text{(S1)}$$

where p_F and $p_{w,i}$ are, respectively, the free perimeter (in contact with air) and wetted perimeters (in contact with the liquid walls) in a cross section of the open channel.

Influence of the parameters

The theoretical developments have shown that there are 3 main groups of parameters: the sub-channel lengths, the cross section decreasing ratio, and the number of daughter channels at each division. A mathematical approach can be done assuming that all sub-channels have the same length.

2. Flow rate as a function of the sub-channel length

The dependency of the flow rate as a function of the lengths of the sub-channels of the capillary tree can be done relatively easily if one considers segments (sub-channel length) of same length, i.e. $L_0=L_1=\ldots=L_n=L$.

In such a case, for bifurcating trees, the time derivative of relation (25) yields the total flow rate

$$Q_n = \frac{2^{n-1}\,\alpha^n\,C}{\left\{\left[2^n\alpha^{4n}L_0 + 2^{n-1}\,\alpha^{4(n-1)}\,L_1+\cdots+2\alpha^4L_{n-1}\right]^2+\alpha^nC\,(t-t_{n-1})\right\}^{\frac{1}{2}}}, \tag{S2}$$

and, considering that the all segments have the same length L, we can write

$$2^n\alpha^{4n}L_0 \;+\; 2^{n-1}\,\alpha^{4(n-1)}\,L_1+\cdots+2\alpha^4L_{n-1} = 2\alpha^4L\left(1+2\alpha^4+\cdots+2^{n-1}\,\alpha^{4(n-1)}\right)$$

$$= \;2\alpha^4L(1-2^n\alpha^{4n})/(1-2\alpha^4). \tag{S3}$$

Then

$$Q_n = \frac{2^{n-1}\,\alpha^n\,C}{\{\,L^2[g(\alpha)]^2+\alpha^nC\,(t-t_{n-1})\}^{\frac{1}{2}}}, \tag{S4}$$

where

$$g(\alpha) = \frac{2\,\alpha^4\left[1-(2\alpha^4)^n\right]}{1-2\,\alpha^4}. \tag{S5}$$

Hence, because L is on the denominator of (S4), reducing L results in an increase of the total flow rate Q_n. In Figure S1, we have plotted the flow rate as a function of the segment length, for a tree comprising 5 levels (n = 5), a coefficient C = 800 mm^2/s, a time interval Δt = 5 s, and two values of α: α = 1 and α = 0.9.

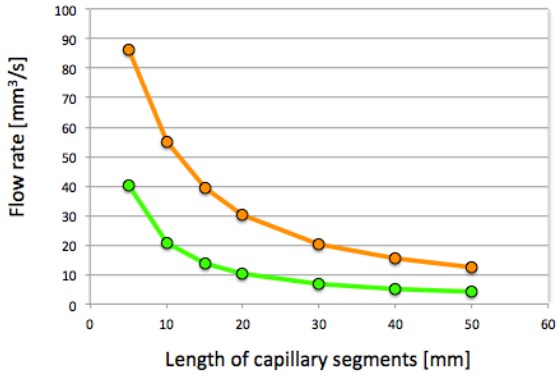

Figure S1. Flow rate as a function of the length of the segments (sub-channels); the green line corresponds to α = 1, and the orange line to α = 0.9.

3. Flow rate as a function of the division numbers

Again, for tractability, we assume that all the tree branches have the same length. Let us note m the number of sub-channels at every channel node. For bifurcation m = 2, for trifurcation m = 3. Then it is shown from (25) and (27) that

$$Q_n = \frac{m^n \alpha^n C}{2\left\{L^2\left[\frac{m\alpha^4\left[1-(m\alpha^4)^n\right]}{1-m\alpha^4}\right]^2 + \alpha^n C\,(t-t_{n-1})\right\}^{\frac{1}{2}}}. \qquad \text{(S6)}$$

For a number of divisions (nodes) n sufficiently high, the numerator of (S6) varies as m^n. On the other hand, the first term of the denominator varies as m^{n-1}. Hence Q_n increases with m. Figure S2 represents the flow rate (S6) for n = 5, L = 20 mm, C = 800 mm^2/s, Δt = 5s and α = 1 and 0.9.

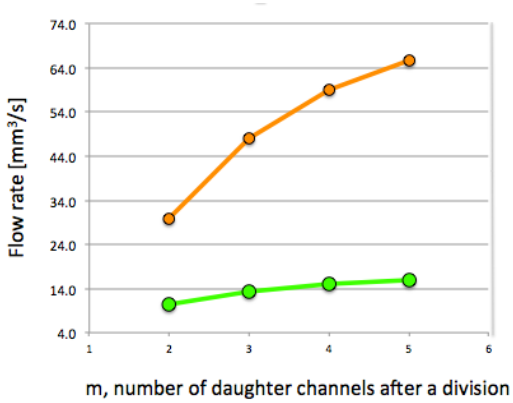

Figure S2. Flow rate as a function of the number of daughter channels at a division m (green line corresponds to $\alpha = 1$, and orange line to $\alpha = 0.9$), $m = 2$ for a bifurcation and $m = 3$ for a trifurcation).

4. Flow rate as a function of the homothetic coefficient α

The influence of α (in equation S4) is difficult to apprehend. The values of the flow rate as a function of α have been numerically calculated and plotted in Figure S3, for $L = 20$ mm, $\Delta t = 5$ s, 10 s, and 20 s, $m = 2$, $n = 5$ and 10. The flow rate increases first with a decrease of the coefficient α, then reaches a maximum.

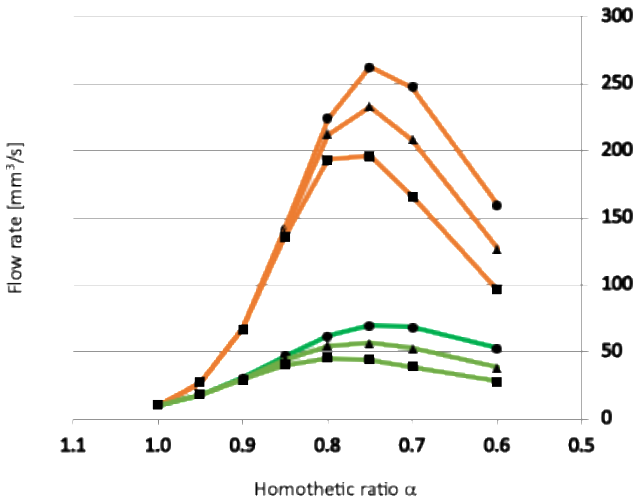

Figure S3. Flow rate as a function of the homothetic coefficient α where $\Delta t = 5$ s (circle), 10s (triangle), and 20 s (square) for the orange lines ($n = 10$) and green lines ($n = 5$).

5. Schematic of devices

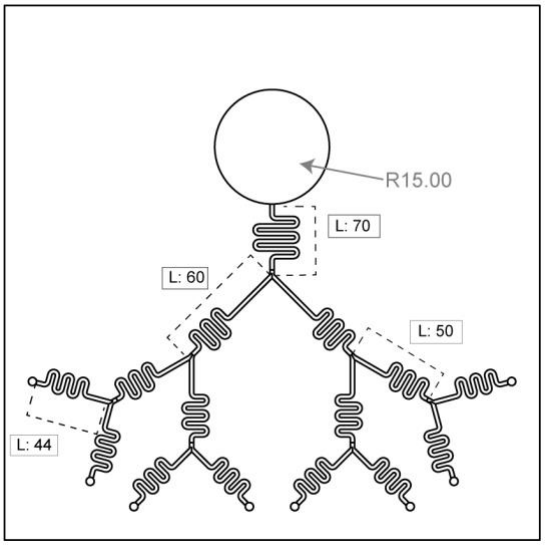

Figure S4. Schematic of bifurcation device with identical cross sections, where L = length, and R = radius. Width of channels are 1.06 mm and depth are 1.76 mm. Units in mm.

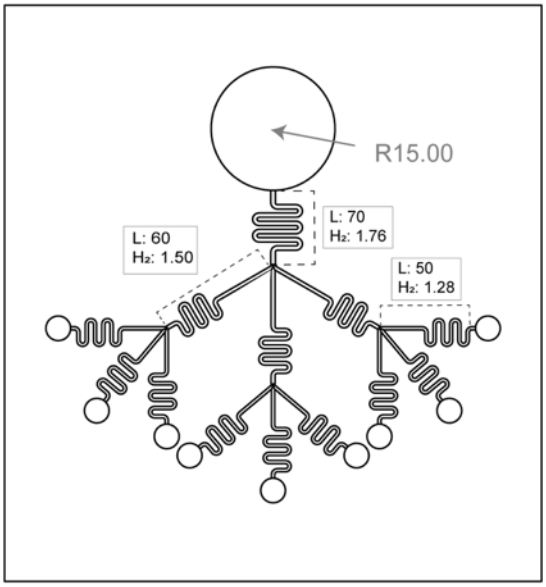

Figure S5. Schematic of trifurcation device with decreasing cross sections where L = length, H = height, and R = radius. Units in mm.

6. Calculation of the friction length using COMSOL

Part of this has been reproduced from the SI from an earlier publication by Lee et al.[2]

A closed form expression for the average friction length does not exist for complicated geometries. A numerical approach can be utilized to find this parameter. Here we use the finite element software COMSOL (www.COMSOL.com).

First a geometry similar to that of the channel is set up. Note that we perform a closed channel calculation with COMSOL. The open surface is then simulated by a solid surface without friction (symmetry condition). This condition introduces an approximation since the real open surface is not flat but slightly bent inwards. The symmetry condition is however justified by the zero shear rate at the free surface, as shown by Brackbill and coworkers.[3] This no-shear condition at the free surface is also used by Koliopoulos and coworkers[4] for the determination of the flow in open rectangular microchannels. An arbitrary average velocity is imposed in the inlet cross section while a zero-pressure condition is set up in the outlet cross section. We emphasize that the inlet velocity can be arbitrary since the friction length does not depend on the average velocity. The shear rate at the wall is deduced from the derivative of the calculated velocities in a cross section, at the nodes of the geometrical meshes close to the solid wall. The shear rate $\dot{\gamma}$ is then averaged along the perimeter of the cross section in order to obtain the averaged shear rate $\frac{V}{\bar{\lambda}}$.

Figure S6 shows the approach for the rounded open channel (where width (w) = 0.80 mm and height (h) = 1.1 mm). The input average velocity is 1 mm/s, and the shear rate averaged from point a to b is $\overline{(\dot{\gamma})}_{a,b} = 6.8\ s^{-1}$. The whole perimeter averaged shear rate is then

$$\overline{(\dot{\gamma})} = \overline{(\dot{\gamma})}_{a,b}\ \frac{p_w}{p_w + p_F} \qquad \text{(S7)}$$

In the present case, the form factor $\frac{p_w}{p_w+p_F}$ is equal to 0.77. Then, using the relation

$$\bar{\lambda} = \frac{V}{\overline{(\dot{\gamma})}}, \tag{S8}$$

where V = 1 mm/s, we find a friction length of 192 µm.

Figure S7 shows the same approach for a double cylindrical open channel. In such a case, we find $\overline{(\dot{\gamma})} \sim 0.6\ \overline{(\dot{\gamma})}_{a,b}$ = 26.4 s^{-1}. The friction length is then 38.8 µm. Of course, the approach can also be used for closed channels, as shown in Figure S8.

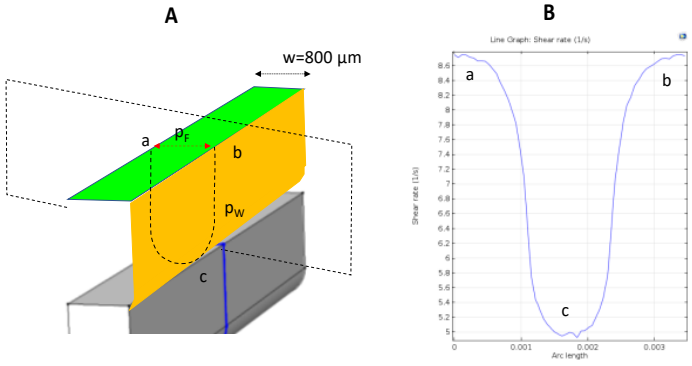

Figure S6. COMSOL model for the calculation of the shear rate in a cross section of a rounded open channel. A) The cover plate (green parallelogram in the figure), the cross section where the velocity profile is considered for the shear rate calculation is defined by the plane perpendicular to the channel. B) Shear rate profile at the wall in curvilinear coordinates system. The points denoted a, b, c are reported from A to B.

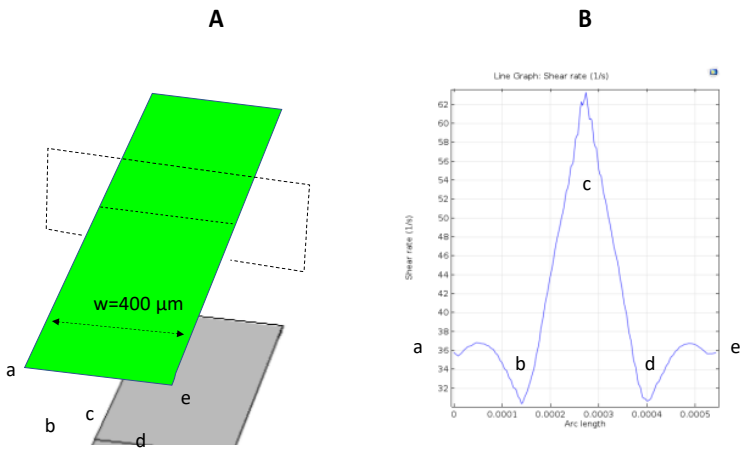

Figure S7. COMSOL model for the calculation of the shear rate in a cross section of a double half cylindrical open channel. A) The cover plate (green parallelogram in the figure), the cross section where the velocity profile is considered for the shear rate calculation is defined by the plane perpendicular to the channel. B) Shear rate profile at the wall in curvilinear coordinates system. The points denoted a, b, c, d, e are reported from A to B.

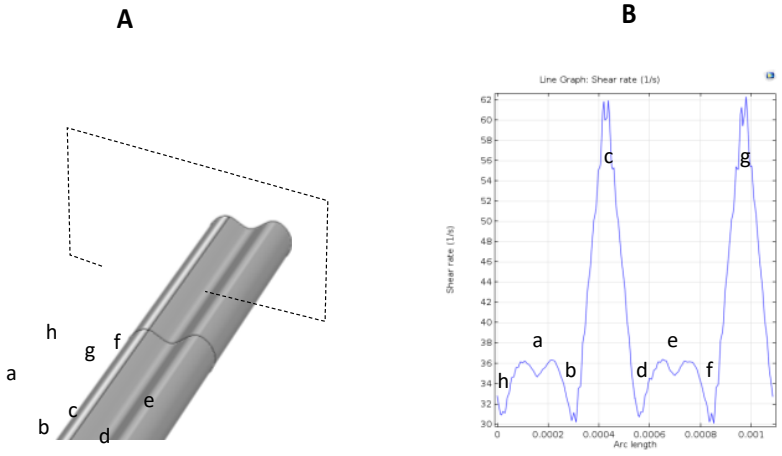

Figure S8. COMSOL model for the calculation of the shear rate in a cross section of a double cylindrical closed channel. A) The cross section where the velocity profile is considered for the shear rate calculation is defined by the plane perpendicular to the channel. B) Shear rate profile at the wall in curvilinear coordinates system. The points denoted a, b, c, d, e, f, g, h are reported from A to B.

7. References

1. Berthier, J.; Brakke, K. A.; Berthier, E. Open Microfluidics; Wiley, 2016.
2. Lee, J. J.; Berthier, J.; Theberge, A. B.; Berthier, E. Capillary Flow in Open Microgrooves: Bifurcations and Networks. Langmuir 2019, 35 (32), 10667–10675.
3. Brackbill, J.; Kothe, D. .; Zemach, C. A Continuum Method for Modeling Surface Tension. J. Comput. Phys. 1992, 100 (2), 335–354.
4. Kolliopoulos, P.; Jochem, K. S.; Lade, R. K.; Francis, L. F.; Kumar, S. Capillary Flow with Evaporation in Open Rectangular Microchannels. Langmuir 2019, 35 (24), 8131–8143. https://doi.org/10.1021/acs.langmuir.9b00226.

VITA

Jing Lee grew up in Curacao. After high school, she attended the California State University of Stanislaus in California to pursue her chemistry degree. During here time in college, she grew found of chemistry, and decided to take her curiosity in the research direction. She moved to Seattle to pursue a doctoral degree at the University of Washington. She joined the Theberge research lab and during her time she studied capillary flow in open system channels while fabricating these channels alongside her journey.